



**LIQUID SPRAY CHARACTERIZATION IN FLOW FIELDS WITH  
CENTRIPETAL ACCELERATION**

THESIS

Andrew J. Brinker, Captain, USAF

AFIT-ENY-14-M-09

**DEPARTMENT OF THE AIR FORCE  
AIR UNIVERSITY**

**AIR FORCE INSTITUTE OF TECHNOLOGY**

---

---

**Wright-Patterson Air Force Base, Ohio**

**DISTRIBUTION STATEMENT A.**  
APPROVED FOR PUBLIC RELEASE; DISTRIBUTION UNLIMITED.

The views expressed in this thesis are those of the author and do not reflect the official policy or position of the United States Air Force, Department of Defense, or the United States Government. This material is declared a work of the U.S. Government and is not subject to copyright protection in the United States.

AFIT-ENY-14-M-09

**LIQUID SPRAY CHARACTERIZATION IN FLOW FIELDS WITH  
CENTRIPETAL ACCELERATION**

THESIS

Presented to the Faculty

Department of Aeronautics and Astronautics

Graduate School of Engineering and Management

Air Force Institute of Technology

Air University

Air Education and Training Command

In Partial Fulfillment of the Requirements for the  
Degree of Master of Science in Aeronautical Engineering

Andrew J. Brinker, BS

Captain, USAF

March 2014

**DISTRIBUTION STATEMENT A.**  
APPROVED FOR PUBLIC RELEASE; DISTRIBUTION UNLIMITED.

**LIQUID SPRAY CHARACTERIZATION IN FLOW FIELDS WITH  
CENTRIPETAL ACCELERATION**

Andrew J. Brinker, BS

Captain, USAF

Approved:

//signed//  
\_\_\_\_\_  
Marc D. Polanka, PhD (Chairman)

13 March 2014  
\_\_\_\_\_  
Date

//signed//  
\_\_\_\_\_  
Mark F. Reeder, PhD (Member)

13 March 2014  
\_\_\_\_\_  
Date

//signed//  
\_\_\_\_\_  
Kevin C. Gross, PhD (Member)

14 March 2014  
\_\_\_\_\_  
Date

### **Abstract**

Performing combustion in the circumferential direction has a significant potential payoff in terms of saving engine length and subsequently weight. Key to this process is the high gravitational load placed on the fuel and air. The additional stretching of the flame should increase the flame speed. The induced buoyancy causes unburnt fuel to remain in the cavity while lighter products migrate out. What is not understood is the flame dynamics for a liquid fuel when sprayed into a combustor with centripetal acceleration. This investigation used Phase Doppler Particle Anemometry (PDPA) to characterize water exiting from a nozzle into a circular cavity with centripetal acceleration. The two-component velocity and size of the droplets in the cavity are measured as a function of centripetal acceleration of the air in the cavity. It was found that the droplets are accelerated by the swirling air flow and that droplet velocity increases with distance from the nozzle up to the tangential velocity in the cavity. It was also seen that increasing the centripetal acceleration causes the larger droplets to migrate to the outer diameter of the cavity, and that the distribution of droplets is sensitive to changes in the centripetal acceleration. These measurements will aid in the development of compact combustors for gas turbine engines that use a circumferential cavity with swirling flow to reduce the length of the combustor. Knowing the spray distribution and residence time for the particles allows optimization of the temperature distribution in the cavity and should enable a minimization of the number of fuel injection sites.

## **Acknowledgments**

First, I would like to express my sincere appreciation to my faculty advisor, Dr Marc Polanka, for his guidance and support throughout the course of this thesis effort. He continually guided me throughout this journey and held high expectations for the benefit of my work. His guidance, support, and insight have helped shape me into the engineer I am today.

I would like to Dr. Daniel Richardson for his unparalleled help and patience while teaching me how to conduct experiments using Phase Doppler Particle Anemometry. He spent countless hours in the lab thoroughly explaining the process of PDPA. He also spent many more hours helping with the test setup, data collection, and data analysis. I am greatly indebted to him for his continued and exceptional support. I would also like to thank the AFIT model shop for their role in the fabrication of many integral parts needed for the successful completion of my thesis work.

Finally I would like to thank my family for their unwavering support and encouragement. Their love and support is the foundation of my success, not only as a student, but also as a human being.

Andrew J. Brinker

## Table of Contents

	Page
Abstract .....	iv
Table of Contents .....	vi
List of Figures .....	viii
List of Tables .....	xi
Nomenclature .....	xii
1. Introduction.....	1
1.1 Background.....	1
1.2 The Ultra Compact Combustor .....	3
1.3 Research Objectives .....	5
2. Literature Review.....	6
2.1 Overview .....	6
2.2 Combustion in a G-loaded environment.....	6
2.3 UCC.....	9
2.4 Fuel Spray Basics .....	25
2.4.1 Atomization of Liquid Jets.....	26
2.4.2 Fuel Spray Analysis in the UCC.....	30
2.5 Phase Doppler Particle Anemometry (PDPA) .....	31
2.5.1 Laser Doppler Anemometry Theory .....	32
2.5.2 Doppler Effect.....	33
2.5.3 Phase Doppler Particle Anemometry.....	36
2.6 Summary.....	37
3. Methodology .....	39
3.1 Full Annular UCC Design .....	39
3.2 Laboratory Air Supply.....	48
3.3 Pressure and Temperature Measurements .....	51
3.4 PDPA Setup.....	54
3.4.1 General .....	54

3.4.2	Initial beam calibration and data collection .....	55
3.4.3	PDPA alignment with the UCC .....	57
3.4.4	Traversing system and data collection grid .....	58
3.4.5	BSA Flow Software Settings .....	62
4.	Analysis and Results .....	69
4.1	Test Conditions.....	69
4.2	Droplet Break-up .....	72
4.3	Stokes Number Determination .....	74
4.4	Concentration Measurements .....	86
4.5	Droplet Velocity and Diameter Analysis .....	89
V.	Conclusions and Recommendations .....	98
5.1	Overview .....	98
5.2	Test Conclusions .....	98
5.2.1	Droplet Break-up .....	98
5.2.2	Stokes Number Determination.....	99
5.2.3	Concentration Measurements.....	99
5.2.4	Droplet Diameter Analysis .....	100
5.3	Recommendations for Future Work .....	101
	Appendix A.....	102
	Appendix B .....	103
	Appendix C .....	105
	Appendix D.....	107
	Bibliography .....	110



## List of Figures

	Page
Figure 1: Standard axial flow combustor [1] .....	2
Figure 2: Flow paths for a UCC [3] .....	4
Figure 3: Observed flame speed plotted against Centrifugal Acceleration [2].....	8
Figure 4: Flame traveling at bubble velocity (left) and flame traveling at turbulent flame speed (right) [2].....	9
Figure 5: T-s diagram of an engine with and afterburner and ITB (solid) and an engine with an afterburner only (dotted) [5].....	10
Figure 6: Specific Thrust vs. Compression Ratio (a) and TSFC vs. Compression Ratio (b) [5] .....	11
Figure 7: Anthenien et al. UCC rig (a) radial vane cavity (b) [6].....	13
Figure 8: Anthenien et al. rig front view (a) side view (b) paired hole injection ring (c) [6] .....	14
Figure 9: UNICORN model of the spreading of a flame under g-loads of (a) 10 g's and (b) 500 g's [7] .....	15
Figure 10: UCC cavity equivalence ratio at LBO as a function of cavity g-loading [7] .	16
Figure 11: Efficiency plots showing efficiency drop-off at low g-loadings [8]. .....	18
Figure 12: Anderson et al. test setup [9] .....	18
Figure 13: CFD velocity vectors in circumferential cavity colored by temperature (F) for CCW flow (a) and CW flow (b) [9] .....	20
Figure 14: Average intensity in the cavity for CCW (left) flow and CW (right) flow[9]	21
Figure 15: Creation of the hybrid guide vane [10] .....	22
Figure 16: G-loading data for 3.24 kg/min core and $\Phi=1.76$ [3].....	24
Figure 17: Migration flow path for CW (left) and CCW (right) [3].....	25
Figure 18: Classification of modes of disintegration [12] .....	29
Figure 19: Fuel spray testing at varying g-loading [14] .....	31
Figure 20: Laser beam with Gaussian intensity distribution [15].....	32
Figure 21: Fringe pattern created by two coherent, vertically polarized laser beams [15] .....	35
Figure 22: Off-axis scattering [15] .....	36
Figure 23: Change in phase difference due to particle size [15].....	37
Figure 24: Full annulus UCC (a) design and (b) main flow paths.....	40
Figure 25: UCC centerbody [3] .....	41
Figure 26: Diagram of circumferential cavity [3] .....	42
Figure 27: Air injection rings [3] .....	43
Figure 28: Fuel plug with atomizing nozzle .....	43
Figure 29: ISCO Model 1000D syringe pumps .....	44
Figure 30: UCC Optical access unobstructed (a) and with a background (b) .....	46
Figure 31: Front face of the UCC with a window, instrumentation panel, and blank panel [3] .....	47
Figure 32: Ethylene-air ignition torch.....	47

Figure 33: Plumbing and splitting of incoming air [3].	49
Figure 34: Set up of the three air supply lines [3].	49
Figure 35: Inlet of the core flow to the UCC	50
Figure 36: Routing of the cavity air.	51
Figure 37: Temperature and pressure instrumentation.	52
Figure 38: Initium Pressure acquisition system (a) 32 port pressure scanner (b)	52
Figure 39: Thermocouple plug board.	53
Figure 40: DANTEC FiberPDA Probe [15]	55
Figure 41: PDPA transmitting optics and calibration screws.	56
Figure 42: Initial PDPA calibration using water in open air	57
Figure 43: Experimental setup configuration.	58
Figure 44: Newport electronic traverse (a) and Newport traverse controller (b)	59
Figure 45: Recording the vertical height of the measurement probe	60
Figure 46: Data collection grid	61
Figure 47: Representative phase plot used to ensure alignment and fringe directions are set correctly [15]	65
Figure 48: Mean diameter of droplets as a function of droplets collected.	68
Figure 49: Temperature and Pressure measurement locations within the cavity.	70
Figure 50: Initial measurements recorded at 1400 g 0.7 MPa	71
Figure 51: Measured velocity for water droplets in the UCC cavity with gravitational loadings of 300, 1400 and 5000 g. The pressure drop across the nozzle is 0.7 or 1.4 MPa. The circles in the plots represent the average droplet size.	72
Figure 52: Vector plots for droplets with Stokes numbers less than 1 for rig operating conditions of 0.7 MPa and g-loadings of 300, 1400, and 5000 g	78
Figure 53: Vector plots for droplets with Stokes numbers less than 1 for rig operating conditions of 1.4 MPa and g-loadings of 300, 1400, and 5000 g	79
Figure 54: Vector plots for droplets with Stokes numbers greater than 2 for rig operating conditions of 0.7 MPa and g-loadings of 300, 1400, and 5000 g	80
Figure 55: Vector plot of the difference of the horizontal components of velocity for particles $[(Stk > 2) - (Stk < 1)]$ at the operation condition of 5000g and injection pressure of 0.7 MPa.	83
Figure 56: Vector plots for droplets with Stokes numbers greater than 2 for rig operating conditions of 1.4 MPa and g-loadings of 300, 1400, and 5000 g	84
Figure 57: Vector plots for droplets with Stokes numbers between 0.5 and 2 for rig operating conditions of 0.7 MPa and g-loadings of 300, 1400, and 5000 g	85
Figure 58: Vector plots for droplets with Stokes numbers between 0.5 and 2 for rig operating conditions of 1.4 MPa and g-loadings of 300, 1400, and 5000 g	85
Figure 59: Vector plots 1400 g 0.7 MPa rig condition for droplet Stokes: $St < 1$ , $0.5 < St < 2$ , and $St > 2$	86
Figure 60: Plots of the location of the highest concentrations of drops for all six cases. The legend indicates the x and y position in the data collection grid at which the concentration of drops was measured	89
Figure 61: Nozzle pressure effect on droplet diameter.	91
Figure 62: Histogram of droplet diameters for 1400 g & 0.7 MPa at horizontal locations of (a) $y=0$ , (b) $y=5$ , (c) $y=10$ , (d) $y=20$ , and (e) $y=30$ .	92

Figure 63: Plot of $D^2$ law for a rig operating condition of 1400 g and 0.7 MPa .....	94
Figure 64: Evaporation constant versus g-load.....	96
Figure 65: Pressure Calibration .....	102
Figure 66: PDA measurements performed on the same nozzle to be used in the UCC	103
Figure 67: Preliminary PDPA fuel nozzle characterization measurements for water flowing through the fuel nozzle .....	104
Figure 68: Plot of $D^2$ law for a rig operating condition of 300 g and 0.7 MPa .....	107
Figure 69: Plot of $D^2$ law for a rig operating condition of 300 g and 1.4 MPa .....	107
Figure 70: Plot of $D^2$ law for a rig operating condition of 1400 g and 1.4 MPa .....	108
Figure 71: Plot of $D^2$ law for a rig operating condition of 5000 g and 0.7 MPa .....	108
Figure 72: Plot of $D^2$ law for a rig operating condition of 5000 g and 1.4 MPa .....	109

## List of Tables

	Page
Table 1: Combustor Design Configurations [8].....	17
Table 2: Matrix of text scenarios. ....	55
Table 3: BSA Flow software specifications.....	62
Table 4: Influence of sample size on accuracy of drop size measurements [20].....	67
Table 5: Maximum and Minimum liquid Reynolds number, Ohnesorge Number, and Weber number.....	73
Table 6: Flow Properties.....	77
Table 7: Difference in velocity of particles ( $Stk > 2$ ) – ( $Stk < 1$ ) at 5000 g and 0.7 MPa	82
Table 8: Location of highest droplet concentrations for each measurement plane.....	87
Table 9: Average vertical and horizontal components of droplet velocity at rig operating conditions of 1400g and nozzle injection pressure of 0.7 MPa. ....	90
Table 10: Values used to calculate evaporation constant .....	94
Table 11: Experimentally calculated K values and associated error .....	95
Table 12: Time in seconds and Distance in mm for complete evaporation of the droplets .....	97
Table 13: Average vertical and horizontal components of droplet velocity at rig operating conditions of 300g and nozzle injection pressure of 0.7 MPa. ....	105
Table 14: Average vertical and horizontal components of droplet velocity at rig operating conditions of 300g and nozzle injection pressure of 1.4 MPa. ....	105
Table 15: Average vertical and horizontal components of droplet velocity at rig operating conditions of 1400g and nozzle injection pressure of 1.4 MPa. ....	105
Table 16: Average vertical and horizontal components of droplet velocity at rig operating conditions of 5000g and nozzle injection pressure of 0.7 MPa. ....	106
Table 17: Average vertical and horizontal components of droplet velocity at rig operating conditions of 5000g and nozzle injection pressure of 1.4 MPa. ....	106

## Nomenclature

A	=	Area
a	=	Local speed of sound
AFRL	=	Air Force Research Lab
AFIT	=	Air Force Institute of Technology
CCW	=	Counter-clockwise cavity direction
CFD	=	Computational Fluid Dynamics
COAL	=	Combustion Optimization and Analysis Laser
$C_p$	=	Specific heat capacity at constant pressure
CW	=	Clockwise cavity direction
DAQ	=	Data Acquisition Unit
EGV	=	Exit guide vanes (compressor)
FS	=	Full scale value
FT	=	Fischer-Tropsch (fuel)
g	=	Gravitational constant for earth / g-load
GCF	=	Gas correction factor
HPT	=	Higher pressure turbine
HSV	=	High speed video
IB	=	Instrumentation block
ID	=	Inner diameter
IGV	=	Inlet guide vanes (turbine)
IR	=	Infrared
ISSI	=	Innovative Scientific Solutions, Inc.
ITB	=	Inter-turbine burner
LBO	=	Lean Blow Out
LE	=	Leading edge
LLCB	=	Low Loss center body
LPT	=	Low pressure turbine
M	=	Mach number

$\dot{m}$	=	Mass flow rate
MFC	=	Mass flow controller
NI	=	National Instruments
OD	=	Outer diameter
OFAR	=	Overall fuel to air ratio
P	=	Pressure
PDPA	=	Phase Doppler Particle Analyzer
PSI	=	Pounds per square inch
r	=	Radius
Re	=	Reynolds Number
R	=	Gas constant
RVC	=	Radial vane cavity
SFC	=	Specific fuel consumption
T	=	Temperature
TCB	=	Tapered center body
TE	=	Trailing edge
UCC	=	Ultra Compact Combustor
V	=	Velocity
$\Phi$	=	Equivalence ratio
$\gamma$	=	Ratio of specific heats
$\rho$	=	Density ( $\text{kg/m}^3$ )

### *Subscripts*

c	=	Referring to gravitational constant of Earth
cav	=	Referring to cavity
COLD	=	Non-reacting conditions
f	=	Final condition
HOT	=	Reacting conditions
i	=	Initial condition

S	=	Stoichiometric
t	=	Total (stagnation) condition
tan	=	Tangential direction
3	=	At the inlet of the combustor
4	=	At the exit of the combustor

# **LIQUID SPRAY CHARACTERIZATION IN FLOW FIELDS WITH CENTRIPETAL ACCELERATION**

## **1. Introduction**

### **1.1 Background**

The gas turbine jet engine was conceptualized and developed during the late 1920's and early 1930's. The concept of the jet engine was relatively simple; it consisted of a compressor, combustor, turbine, and nozzle. The idea was that air would enter the compressor, be pressurized and then move through a combustor section where fuel was added and ignited. The hot exhaust products produced by the combustion reaction would then expand and travel through the turbine blades causing them to rotate. The turbine blades were attached to the compressor via spools such that when the turbine blades rotated, the compressor blades rotated as well, compressing the air. After passing through the turbine the exhaust gases were then channeled through a nozzle providing a propulsive force.

This day and age, the gas turbine engine is commonplace. Gas turbine engines are used for applications such as power generation for the electrical industry to applications including the primary means of propulsion for aircraft. A gas turbine engine when used for aircraft propulsion is more commonly referred to as a jet engine. Jet engines create unique and complex challenges when compared to a gas turbine engines used for power generation. For power generation a gas turbine engine has the primary purpose of producing power and in most cases is not limited by size and weight requirements. On the contrary, when using a jet engine on an aircraft, the primary



purpose of the engine is to generate enough thrust to allow flight. To achieve successful flight, the thrust-to-weight ratio of an aircraft is a significant factor. A jet engine must balance a fine line of minimizing overall weight while increasing the output of thrust.

Conventional combustors, since the advent of the jet engine up to now, have burned fuel in the axial direction of the engine. Figure 1 illustrates the operation of a standard combustor in a jet engine. Air exits the compressor where it is diffused to a Mach number of approximately 0.1 and directed into the combustor [1]. Inside the combustor, fuel is added and burned at fuel lean conditions. The amount of time required for complete combustion of the fuel dictates the length of the combustor [1]. It is imperative that the combustion reaction is complete prior to the first stage of the turbine due to temperature limitations of jet engine materials; however, a greater temperature at the exit of the combustor increases the efficiency of a jet engine. A delicate balance of combustor exit temperatures, material properties, and engine cooling schemes must be achieved for the highest possible efficiency.

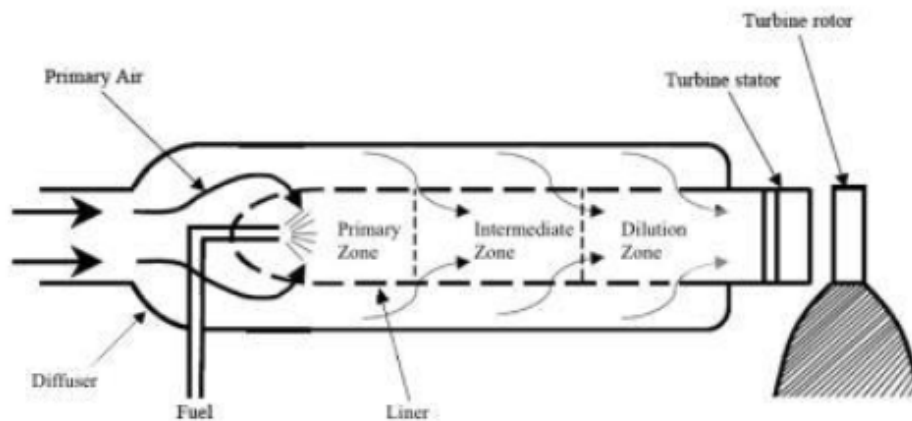


**Figure 1: Standard axial flow combustor [1]**

Long axial combustor lengths required for complete combustion means more material and greater engine weights. The axial length of the combustor negatively affects the thrust-to-weight ratio of a jet engine. The lean burning conditions within the combustor are intended to not only ensure complete combustion but to also aid in reducing the overall engine size while still generating the required power. Improving thrust-to-weight ratios up to this point has primarily focused on using film cooling techniques and materials with a higher temperature resistance in order to increase the air temperature at the entrance of the turbine and therefore increasing efficiency, power, and thrust. Rather than increasing the thrust, recent research and experimentation has been conducted to find ways to shorten the combustor of a jet engine, reducing engine weight and increasing the thrust-to-weight ratio. One method utilizes a circumferential combustion cavity to reduce the axial combustion length. This is known as the Ultra Compact Combustor (UCC).

## **1.2 The Ultra Compact Combustor**

Over the past decade, the Air Force Research Laboratory (AFRL) and the Air Force Institute of Technology (AFIT) have worked in conjunction to develop a unique solution to decrease the length of combustors and in turn increase the thrust-to-weight ratio of jet engines. Rather than burning fuel in the axial direction of the engine, the flow would be turned to swirl circumferentially in a cavity around the engine creating a centrifugal force known as gravitational loading (g-load). The benefits of burning under a g-load were first realized by Lewis [2] in the early 1970's. Lewis found that flame fronts of a combustion reaction subjected to a g-load would propagate at velocities

greater than that of the turbulent flame speed of the mixture. The increased reaction rates mean shorter residence times, therefore less space is required for the combustion process.

Circumferential swirl in the combustion cavity is achieved either through angled air driver jets located around the outside diameter (OD) of the UCC or through angled holes in the front plate of the UCC. A representation of the flow paths for splitting air into a core and cavity flow is shown in Figure 2, where the cavity air is injected into the primary combustion zone through holes along the OD.

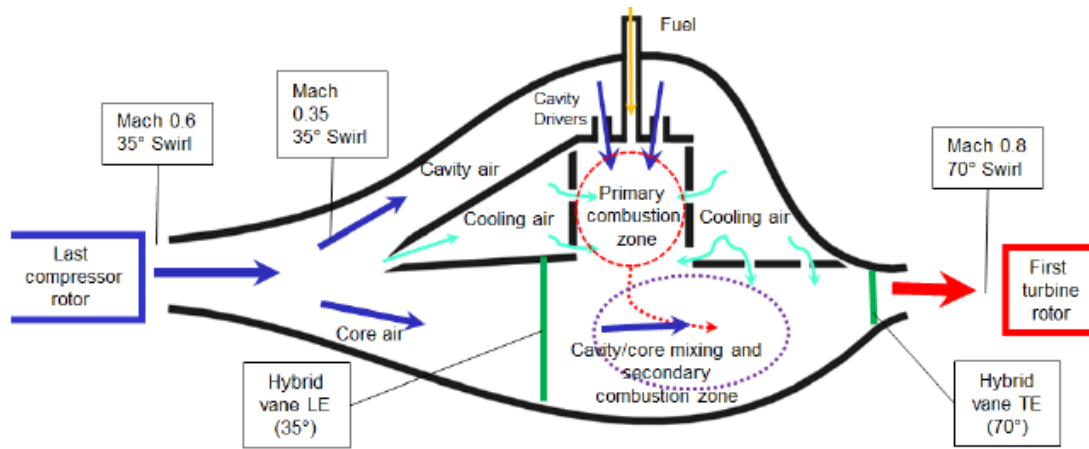


**Figure 2: Flow paths for a UCC [3]**

The g-load inside the cavity creates a density gradient in which the heavier, unburned reactants are forced toward the OD of the cavity due to the centrifugal force while the lighter, buoyant combustion products migrate toward the center of the UCC and merge with the core and then travel to the turbine. The density gradient in theory creates an infinite residence time for fuel, ensuring all the fuel is consumed and allowing for efficiencies upwards of 99% based on emissions measurements.

### **1.3 Research Objectives**

There are many challenges associated with designing the UCC. One of the primary challenges is the integration of liquid fuels to the UCC. Aircraft engines use liquid fuels, therefore it is important to understand how the liquid fuel will act when injected into the circumferential cavity under high g-load conditions. Currently very little analysis has been conducted for sprays in general subjected to high g-loads such as those present in the circumferential cavity of the UCC.

The primary objective of this research is centered on characterizing how a liquid spray is distributed in the circumferential cavity under a g-load. Characterizing how the liquid is distributed will provide valuable information regarding the UCC combustion process. This information will include how long the spray remains in the cavity and the distribution of fuel nozzles within the circumferential cavity required to achieve a consistent spray pattern for uniform combustion. The spray data will ultimately provide insight as to the number of fuel injectors needed to create a continual burning pattern while minimizing the number of nozzles for manufacturing and cost reasons.

## **2. Literature Review**

### **2.1 Overview**

Jet engine developers are always looking for ways to increase the thrust-to-weight ratio of an engine and improve combustion efficiency. As mentioned in Chapter 1, a proposed solution to increase the thrust-to-weight ratio and combustion efficiency of an engine is the Ultra Compact Combustor (UCC). The UCC is still in the infancy stages of the design process; continuous research and testing is needed to make the UCC feasible as an option for the main combustor of a jet engine. Over the past decade, AFRL and AFIT have studied the UCC in detail, conducting research on the combustion process while the fuel is ignited under g-loading. The results from previous UCC experimentation provide the basis for the current research being conducted at AFIT. In order to understand the research presented in this thesis, it is important to include a discussion detailing previous research and development of the UCC. The information in this chapter will present the necessary background needed to complete the research objective of characterizing and analyzing fuel spray patterns in the presence of centripetal acceleration.

### **2.2 Combustion in a G-loaded environment**

The effects of high g-loading on combustion were realized due to the results of experiments performed by Lewis [2] in the early 1970s. Lewis [2] investigated the role of centrifugal forces on flame speed using a combustion centrifuge constructed from a stainless steel pipe with an inside diameter of 6.7 cm and measuring 1.83 m in length. A spark plug was mounted to one end of the pipe while an electric motor was attached to

the midpoint, allowing for variable rotation rates and g-loading. The experiments proved that for a propane-air mixture at a g-loading greater than 200 g's bubbles or eddies moved ahead of the flame front due to the centripetal acceleration [2]. When the loading was less than 200 g's, the propagation of the flame was unaffected, and the flame speed was equal to that of the turbulent flame speed [2]. At g-loadings between 200 and 500 g's, a transition region was observed where flame speeds began to increase to values greater than that of the turbulent flame speed. When g-loadings reached a range between 500 and 3500 g's, Lewis found that the flame speed increased in proportion to the square root of the centrifugal force [2]. As g-loads reached values greater than 3500 g's, the flame speed began to decrease with increasing centrifugal force to a point at which combustion would not occur. Experiments for propane-air mixtures at various equivalence ratios were performed and all exhibited the same behavior. In addition to propane-air mixtures, experiments were also conducted with hydrogen-air mixtures. Test conducted using a stoichiometric mixture of hydrogen and air resulted in a constant flame propagation rate over the range of g-loads. However, when the equivalence ratio of the hydrogen-air mixture was reduced to 0.6, the resulting flame speeds corresponded closely to propane-air mixtures. Results for the flame speeds of various propane-air mixtures under a g-load are represented in Figure 3.

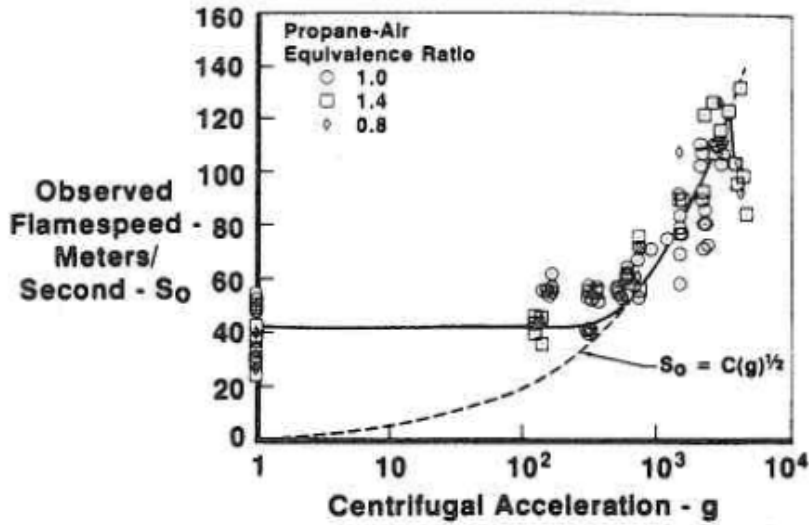


**Figure 3: Observed flame speed plotted against Centrifugal Acceleration [2]**

Based off of the experimental results, Lewis [2] concluded that two different phenomenon exist which control the flame spreading. At g-loads less than 200 g's, the propagation rate of the flame is equal to that of the turbulent flame speed ( $S_T$ ). As the g-loading is increased from 200 to 3500 g's, the centrifugal force pushes a bubble of more buoyant product gases forward of the flame causing an increase in the propagation rate of the flame. Lewis [2] defined the increased propagation rate as the bubble velocity ( $S_B$ ). Figure 4 illustrates and compares the two types of reactions, one where the flame speed is equal to the turbulent flame speed and one where the bubble velocity drives the flame propagation rate. In Figure 4, the crosshatched circles represent bubbles of combusted gas products and the dashed line represents the flame front. After a short time period  $\Delta t$ , the left image shows the bubble of combusted gases driving the propagation of the flame. The image on the right illustrates that the flame will spread at the turbulent flame rate if the bubble velocity of combusted gases is less than that of the turbulent flame speed.

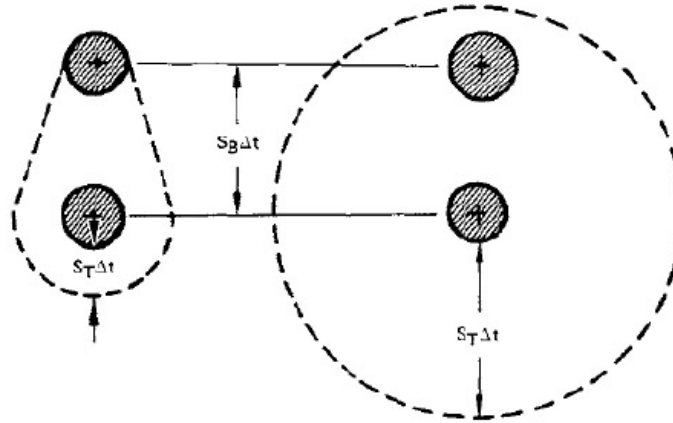


**Figure 4: Flame traveling at bubble velocity (left) and flame traveling at turbulent flame speed (right) [2]**

Lewis used the knowledge gained from his experiment and applied swirl to a full size augmenter of a turbofan engine. The flame holders of the conventional augmenter were removed, fuel spray bars were rearranged, and swirl vanes were added in order to swirl stabilize the flame. Results from the test showed that by removing the flameholders and using swirl to stabilize the flame, a 2% improvement in specific fuel consumption was achieved [2]. The results of the experiment also showed an increase in flame stability over the conventional flameholder design by a factor of 20 [2]. Yonezawa et al. [4] applied Lewis' [2] concepts and designed a jet-swirled main combustor. For a given loading factor, Yonezawa et al. showed that the jet-swirled main combustor was more efficient than a conventional combustor and that the rate of combustion increased dramatically allowing for the combustor to be 33% shorter than conventional combustors [4].

### 2.3 UCC

The idea of using a reheat cycle to obtain more specific power and thermal efficiency is not a new idea, it has been used in the power generation industry for years



with great success. However, using the idea of a reheat cycle for applications in the aeronautical industry is a relatively new idea due to size and weight limitations. Increasing the thrust-to-weight ratio of an aircraft engine is a chief concern of engine manufacturers; therefore, the benefits of introducing a reheat cycle to an aircraft engine need to outweigh the additional weight due to more hardware. Knowing the thermodynamic benefits of the reheat cycle, W.A. Sirignano, J. P. Delplanque, and F. Liu [5], performed a thermodynamic analysis of an engine utilizing a reheat cycle. For the analysis, the reheating took place between the high pressure turbine (HPT) and low pressure turbine (LPT) of the engine in a device known as an interstage turbine burner (ITB). The cycle analysis performed by Sirignano et al. [5] compared various configurations of a turbine engine with ITBs and afterburners. In theory, an ITB is more efficient than an afterburner due to the fact that heat is added between the turbines where the pressure is greater than that of the afterburner. For a given temperature range, the Carnot cycle is the most efficient cycle with heating occurring at a constant temperature. Figure 5 uses a solid line to depict the T-s diagram of an engine with an ITB and an afterburner while the dotted line represents an engine with an afterburner only.

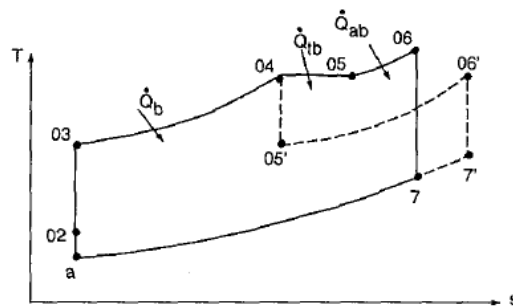


**Figure 5: T-s diagram of an engine with and afterburner and ITB (solid) and an engine with an afterburner only (dotted) [5]**

Sirignano et al. [5] conducted the thermodynamic analysis on four types of gas turbine engines: (1) without afterburner or ITB, (2) with afterburner, (3) with ITB only, and (4) with ITB and reduced afterburner. Using the data gained from the cycle analysis, plots of specific thrust (ST) and thrust specific fuel consumption (TSFC) were generated for all the engines and are shown in Figure 6. The plots show that adding an ITB to an engine with an afterburner increases the ST of the engine while decreasing the TSFC.

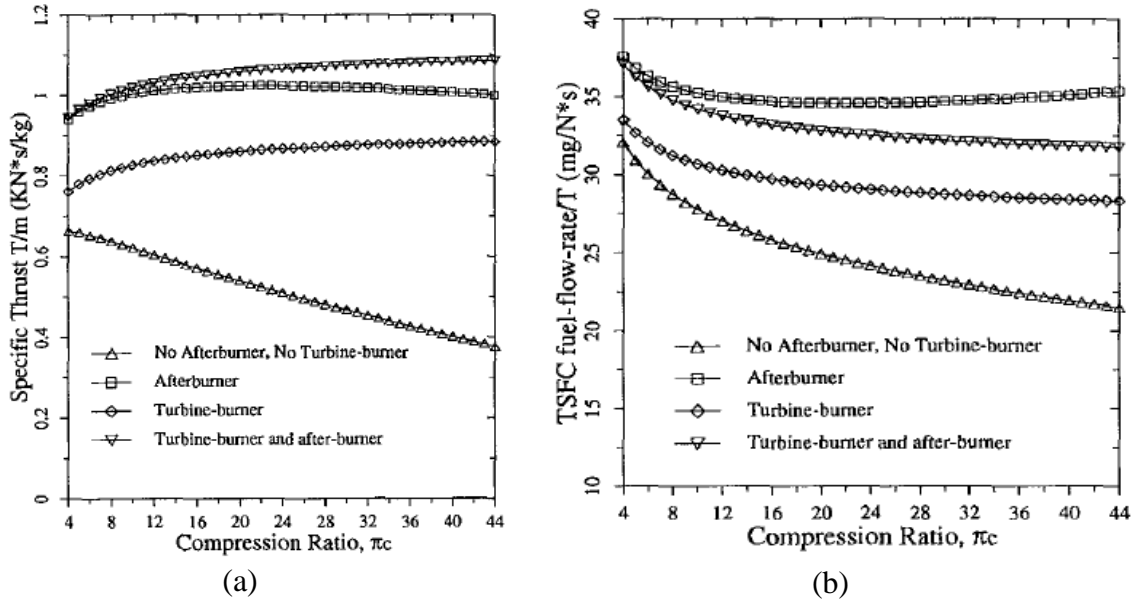


**Figure 6: Specific Thrust vs. Compression Ratio (a) and TSFC vs. Compression Ratio (b) [5]**

Ideally, the concept of a constant temperature reheat cycle requires burning in the turbine rotor. Due to cooling issues and material limits, burning in the turbine rotor is not desirable. A more feasible option as mentioned earlier is to place an ITB between the HPT and LPT that would burn fuel in the turning vanes prior to the rotor. Sirignano et al. [5] showed that theoretically adding an ITB to a gas turbine engine proved to be beneficial; however, current conventional combustors are too large to place between the turbine stages.

R. A. Anthenien, R. A. Mantz, W. M. Roquemore, and G. J. Sturgess [6], researchers at the Air Force Research Laboratory (AFRL), introduced the concept of using an Ultra Compact Combustor (UCC) as a feasible option for an ITB. Anthenien et al. [6] constructed a UCC applying the knowledge of high g-load burning learned from Lewis [2] and Yonezawa et al [4]. The test rig was axi-symmetric and included a circumferential cavity that wrapped around the turning vanes to the turbine rotor as is shown in Figure 7a. Swirling air flow inside the circumferential cavity was supplied by injecting air along the outside diameter of the cavity at a  $45^\circ$  angle to the radial direction. Fuel was injected at six equally spaced locations around the OD of the circumferential cavity. Fuel was burned rich in the swirling flow of the circumferential cavity which allowed for the combustion process to take place circumferentially rather than axially as in a conventional combustor. The swirl induced in the circumferential cavity created a high g-load, increased reaction rate, and a shorter chemical residence time [6]. The g-loading caused the heavier reactants to remain in the cavity for complete combustion while buoyancy effects caused the lighter combustion products to migrate toward the center of the rig and into the core flow. The UCC design of Anthenien et al. [6] incorporated radial vane cavities (Figure 7b) in the turning vanes around which the circumferential cavity was located. The purpose of the radial vane cavity (RVC) was to transport combustion products from the circumferential cavity into the core flow while allowing for complete combustion.

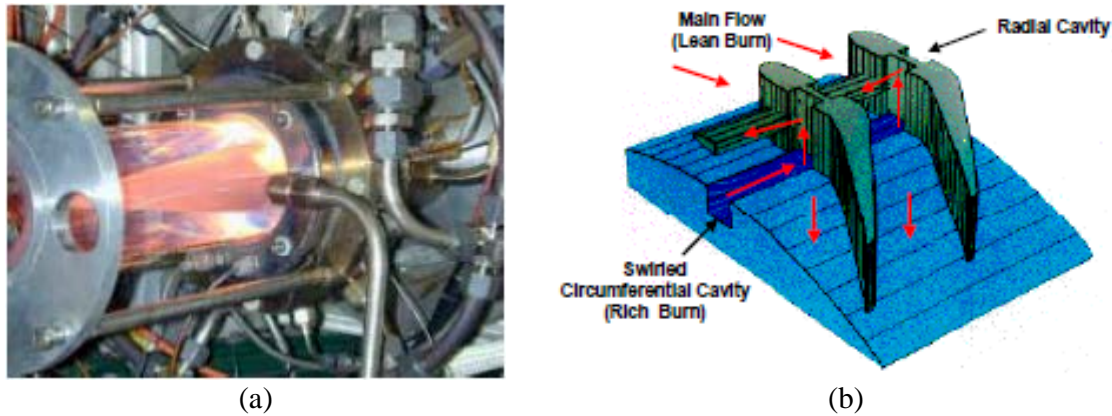


**Figure 7: Anthenien et al. UCC rig (a) radial vane cavity (b) [6]**

Anthenien et al. [6] initially conducted tests in which air was injected into the circumferential cavity through 12 slots around the OD. When air was injected through the slots, it was difficult to ignite the rig and very low efficiencies were observed by analyzing the emissions of CO, CO<sub>2</sub>, O<sub>2</sub>, NO<sub>x</sub>, and unburned hydrocarbons (THCs). Anthenien et al. [6] hypothesized that the curtain of air from the air slot collapsed the fuel spray and reduced mixing. To test this hypothesis, an outer ring was fashioned to inject air using paired round holes rather than slots. The paired holes allowed for air to be injected on either side of the fuel spray, preventing the fuel spray from collapsing. Combustion efficiencies of 99+% for both JP-8 and ethanol were observed when using the air injection method of paired holes. Figure 8 illustrates how air was injected into the circumferential cavity using paired holes along the OD.

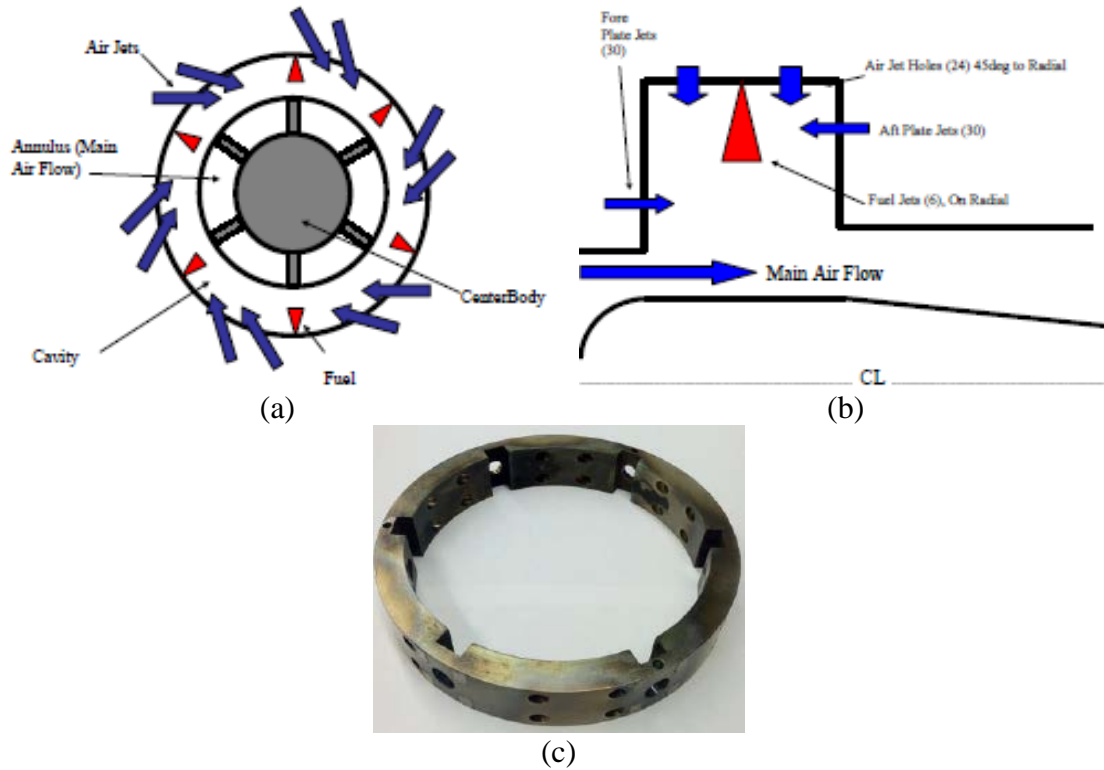


**Figure 8: Anthenien et al. rig front view (a) side view (b) paired hole injection ring (c) [6]**

J. Zelina, G. J. Sturgess, and D. T. Shouse [7] employed the UCC designed by Anthenien et al. [6] and performed experiments in an effort to characterize how centrifugal loading enhanced turbulent burning rates in the UCC. Zelina et al. [7] attempted to confirm the bubble velocity hypothesis proposed by Lewis [2]. To confirm the hypothesis, first-order numerical experiments were conducted using the Unsteady Ignition and Combustion with Reactions (UNICORN) code [7]. A tube measuring 50 mm wide by 100 mm long was filled with a hydrogen-air mixture at a stoichiometric value of 0.8. The tube was subjected to g-loads of 10 g's and 500 g's and a flame was initiated at the bottom of the tube by three separate ignition sources [7]. The g-loadings of 10 g's and 500 g's were chosen to confirm the centrifugal loading regions where Lewis [2] proposed that the bubble velocity was or was not a factor. Figure 9 shows the

propagation of the flame front at three points in time for the two loading conditions.

Figure 9b confirms the bubble-transport hypothesis proposed by Lewis [2], showing that the flame subjected to 500 g's propagates at a much faster rate than the flame subjected to only 10 g's. Through experimentation, Lewis [2] found that flame speed increased with increasing g-loading up to an inflection point around 3500 g's where the flame speed would then rapidly decrease until blowout occurred around 8000 g's. The results found by Zelina et al. [7] coincide with results obtained by Lewis.

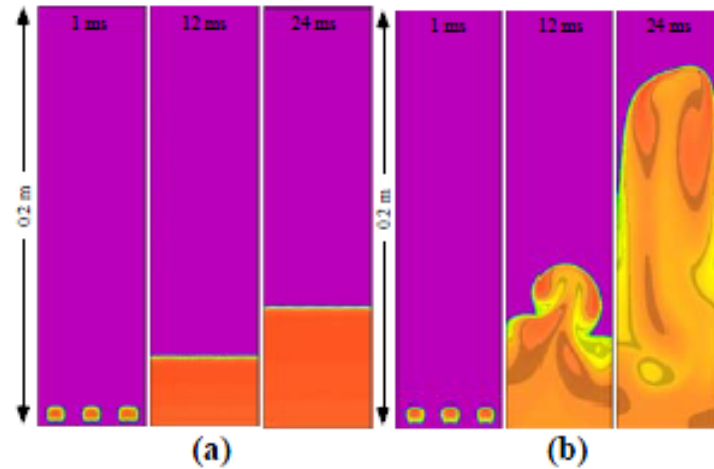


**Figure 9: UNICORN model of the spreading of a flame under g-loads of (a) 10 g's and (b) 500 g's [7]**

Zelina et al. [7] applied the lessons learned from Lewis and conducted a series of lean blowout (LBO) tests on the UCC. The tests revealed the UCC had superior LBO characteristics compared to conventional systems [7]. Figure 10 shows the stability region of the flame by plotting the combustor LBO equivalence ratios ( $\Phi_{cav}$ ) against g-loading. With an equivalence ratio of one, the flame remained stable all the way up to g-loadings between 7000 to 8000 g's. In addition to the stability results, Zelina et al. also

noted that the flame lengths within the UCC were up to 50% shorter than those of a conventional combustor [7].

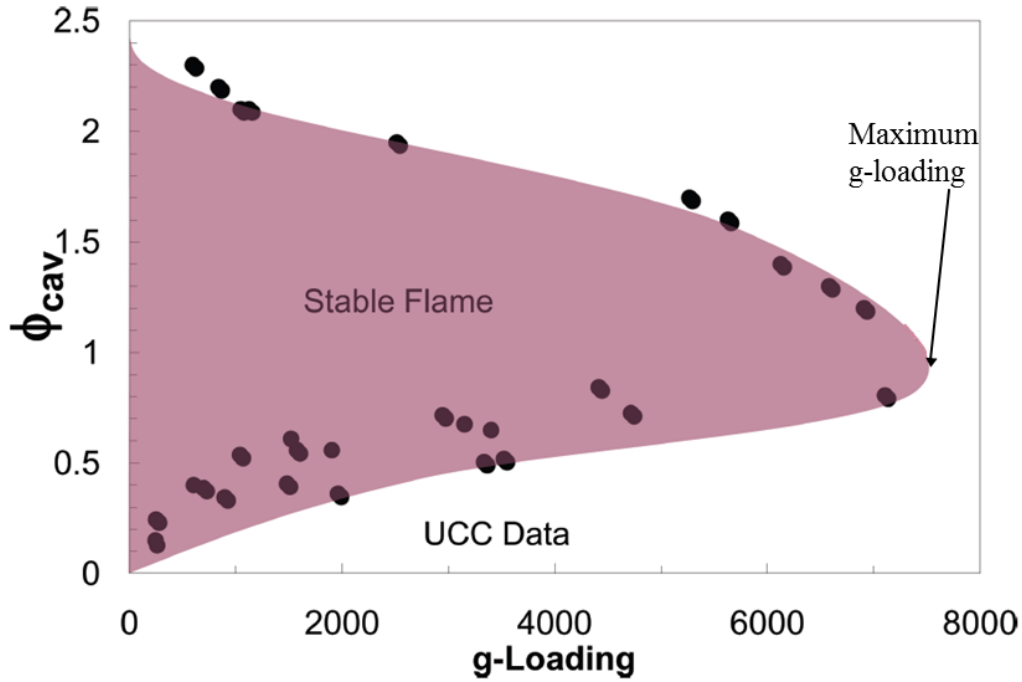


**Figure 10: UCC cavity equivalence ratio at LBO as a function of cavity g-loading [7]**

J. Zelina, D. T. Shouse, and R. D. Hancock [8] performed additional tests on the rig developed by Anthenien et al. [6] in an effort to better measure combustion stability, combustion efficiency, and pollutant emissions. As was the case before, fuel was injected at six discrete locations spaced equally around the circumferential cavity. Air was injected into the cavity at a 45° angle to the radial direction through twelve sets of paired rounded holes [8]. For all tests, the same fuel injectors were used; however, the fuel injectors were recessed either 0.041 inches or 0.125 inches from the outside diameter of the circumferential cavity. The different fuel injector recess depths were selected to

investigate the effect of air emitted to the system around the injector [8]. Straight vanes were used on the center-body for all cases, but in two of the configurations a radial cavity was machined into the vane. The RVC was located such that it faced the circumferential flow; its purpose was to aid in transporting the combustion products radially out of the circumferential cavity and into the core flow [8]. The four experiment configurations are shown in Table 1. The experiments conducted by Zelina et al. [8] resulted in combustion efficiencies ranging from 95% to 99% based on emission measurements of CO, CO<sub>2</sub>, O<sub>2</sub>, NO<sub>x</sub>, and unburned hydrocarbons. The results showed that at lower g-loadings there was a large drop off in efficiency which appeared to correlate with the amount of air entering the cavity around the fuel injector. The drop in efficiency is attributed to primarily lean  $\Phi_{cav}$ 's with slow reaction rates and quenching occurring in the main flow [8]. The reduced efficiency also correlated to premature mass extraction from the circumferential cavity due to a strong pressure gradient caused by the RVC [8]. The trends of efficiencies can be seen in Figure 11.

**Table 1: Combustor Design Configurations [8]**

<b>Configuration</b>	<b>Injector Recess (in.)</b>	<b>% Total Airflow Due to Injector Air</b>	<b>Vane Design</b>
1	0.041	0.4	Flat
2	0.041	0.4	Radial Cavity
3	0.125	1.2	Flat
4	0.125	1.2	Radial Cavity



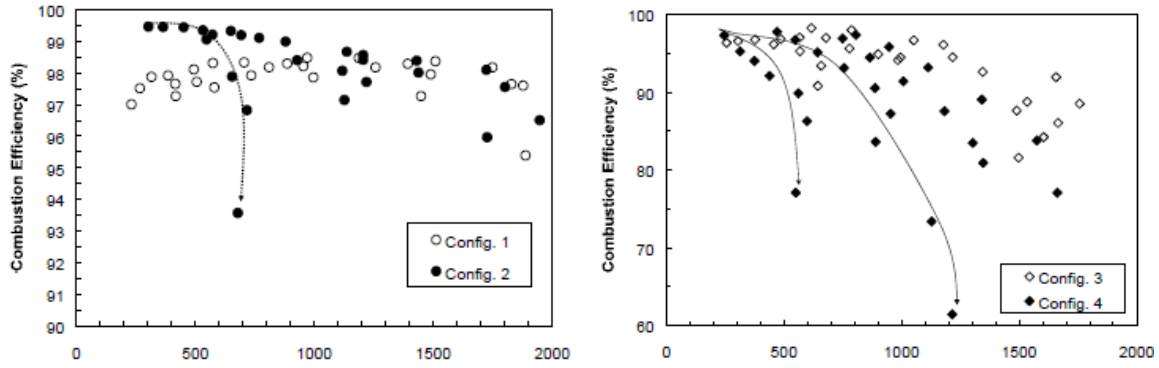


**Figure 11: Efficiency plots showing efficiency drop-off at low g-loadings [8].**

W. Anderson, J. Radtke, P. King, H. Thornburg, J. Zelina, and B. Sekar [9], used the UCC developed by Anthenien et al. [6] and conducted experiments in an effort to determine the effects of main swirl direction in the circumferential cavity on high-g combustion. The rig was modified with four simulated turbine inlet guide vanes with radial vane cavities. The guide vanes were equally spaced around the center body creating four equal sized flow passages. The set up was designed to simulate flow coming directly off a compressor rotor [9]. Representations of the modified center body and UCC are depicted in Figure 12 [9].

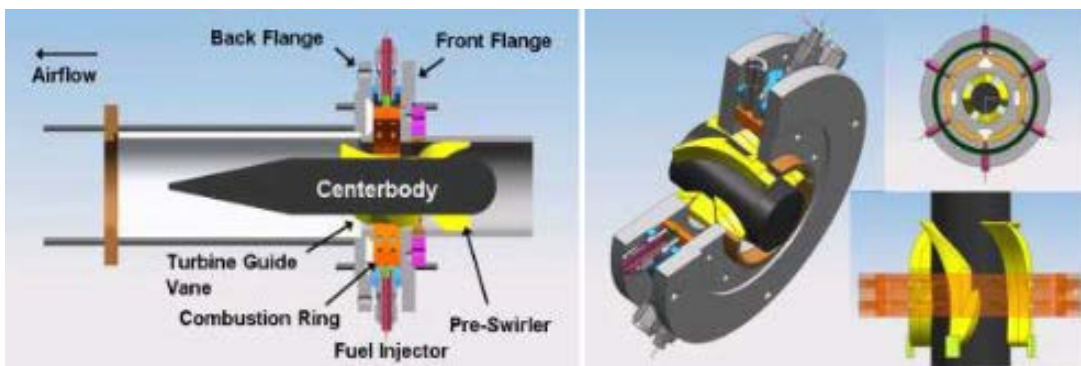


**Figure 12: Anderson et al. test setup [9]**

The experiments were conducted using JP-8 and Fischer-Tropsch (FT) jet fuels. In addition to pressure, temperature, and emissions measurements, CFD analysis was utilized to depict the aerodynamics inside the cavity. The experimental results indicated that depending on whether the flow was swirling clock-wise (CW) or counter clock-wise (CCW), flow behavior inside the circumferential cavity varied significantly. CFD analysis illustrated when the cavity flow was swirled in the CCW direction, the RVC significantly impacted the amount of hot flow drawn into the core of the UCC. The effect of the RVC is seen in the circle in Figure 13. When flow is swirled in the CW direction, the same area in the flow field experiences a very different behavior. Cold air is entrained by the RVC and aids in the development of flow recirculation regions between vane locations. UCC stability was reduced at high flow rates with swirl in the CW direction. The CFD results for the CW flow direction showed that high temperature regions were further away from the cavity-in-cavity (CIC) fuel injection locations. This meant that hot products from upstream injectors were not effectively entrained into downstream CIC locations, reducing the ability to ignite the fuel in the downstream CIC. It was hypothesized that this decrease in flame holding ability was due to the entrainment of cool core airflow and the formation of recirculation zones [9]. Figure 14 was taken using high speed digital photography and compares the flame holding ability for cavity flow in the CCW and CW directions.

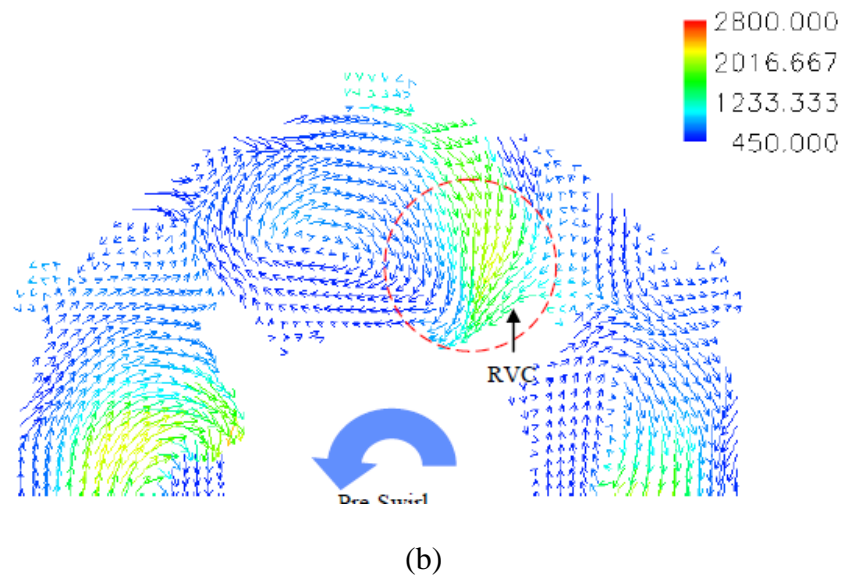
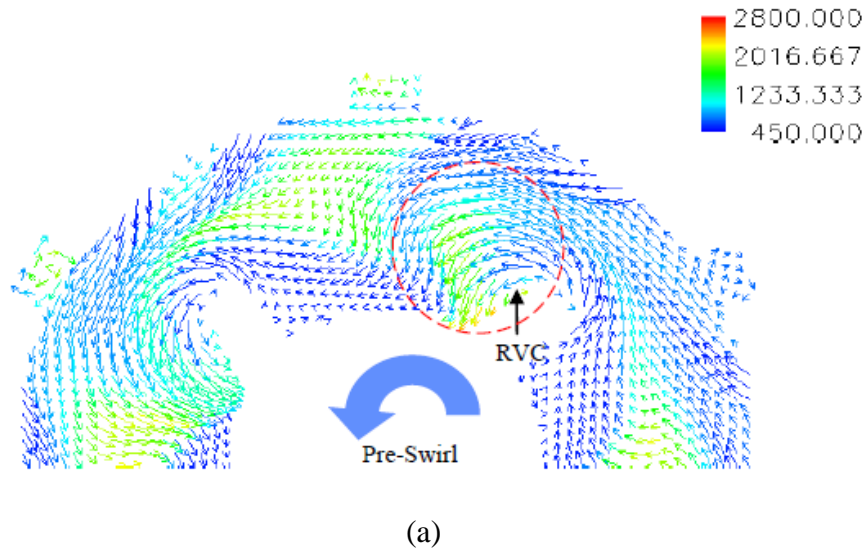


**Figure 13: CFD velocity vectors in circumferential cavity colored by temperature (F) for CCW flow (a) and CW flow (b) [9]**

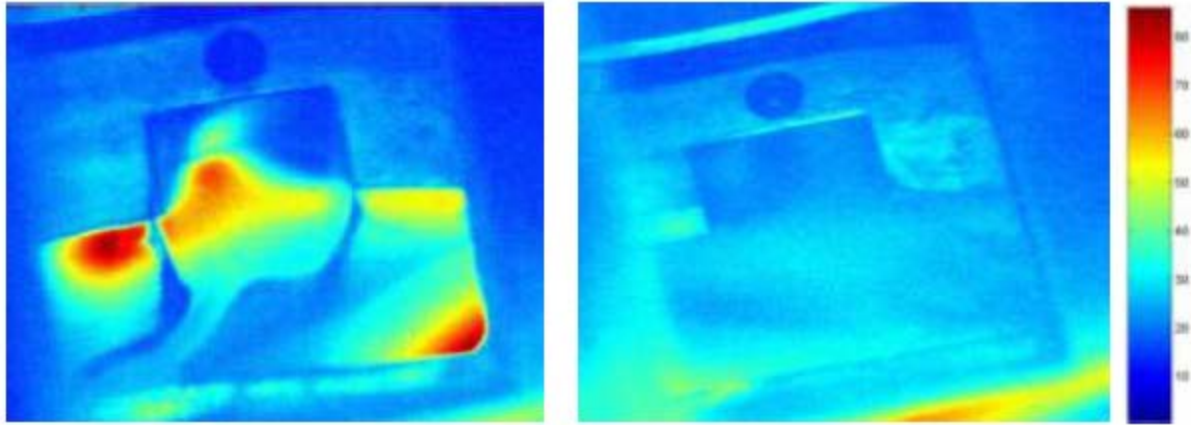


**Figure 14: Average intensity in the cavity for CCW (left) flow and CW (right) flow[9]**

When comparing the two different types of fuels, combustion efficiencies above 99% were experienced for cavity equivalence ratios higher than  $\Phi=1.2$  for both the CW and CCW flows. The experimental results showed that the lean blow-out characteristics and emissions data for both fuels were similar.

CFD work was also conducted at the Air Force Institute of Technology (AFIT) by B. T. Bohan and M. D. Polanka [10] to analyze the flow patterns in a full scale UCC designed for fighter engines. For their research Bohan and Polanka developed a hybrid UCC guide vane. The hybrid guide vane allowed for the conventional compressor exit guide vane and turbine IGV to be combined with the circumferential cavity of the UCC wrapped around the hybrid vanes. With the compressor exit guide vane removed, the hybrid vane was designed to accept the swirl from the last rotor of the compressor and turn the flow to the correct angle for the first HPT rotor. Figure 15 shows the process by which the compressor exit guide vanes and the turbine IGVs are combined into one hybrid vane.

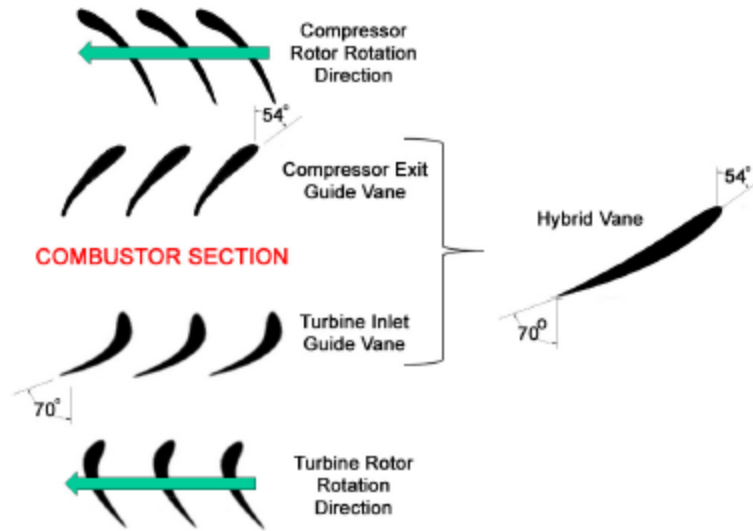


**Figure 15: Creation of the hybrid guide vane [10]**

The CFD work by Bohan and Polanka [10] focused on how the diameter of the air injection holes along the OD of the UCC affected the tangential velocity and g-loading within the circumferential cavity when overall mass flow was kept constant. The results of the experiments indicated that as the diameter of the air injection holes decreased, the velocity through the holes increased to maintain the same mass flow [10]. The increase in velocity in turn directly affected the g-loading in the cavity since the cavity g-loading is a function of the tangential velocity squared.

J. D. Wilson [3] developed a small scale full annulus UCC for research at AFIT. The AFIT rig was developed based off the same general layout of the AFRL rig developed by Anthenien et al [6]. The AFIT rig incorporated six of the hybrid vanes designed by Bohan and Polanka [10] in order to match the number of vanes to the number of fuel injectors. Multiple air injection rings with varying hole diameters were also created to experimentally test the CFD results of Bohan and Polanka [10]. The rig

also included increased optical access into the circumferential cavity allowing for flame structures and fuel sprays to be analyzed.

The experimental results found by Wilson for varying air injection hole diameters was consistent with the CFD work previously accomplished by Bohan and Polanka [3]. Three different air injection rings with hole diameters of 0.35, 0.45, and 0.65 cm were tested at a constant core mass flow of 3.24 kg/min [3]. The cavity mass flow was varied from 1.08 to 1.44 kg/min at an equivalence ratio of  $\Phi=1.76$ . The 0.35 cm diameter holes imparted the greatest g-load followed by the 0.45 and 0.65 diameter holes [3]. The g-loading for the various hole diameters is represented in Figure 16. Wilson noted that for the 0.35 and 0.65 diameter holes, the rig experienced greater instability and rapid blowout for mass flows greater than 1.44 kg/min while the 0.45 cm ring was able to maintain stability up to cavity mass flows of 2.16 kg/s [3]. Additional pressure measurements were recorded along the quarterline of the circumferential cavity in an effort to explain the reduced stability seen in the 0.35 and 0.65 cm rings. The measurements indicated that there was a minimal g-load/velocity gradient present for the 0.45 cm ring; however, for the 0.35 cm ring, a larger g-load/velocity gradient was present. Wilson hypothesized that the g-load/velocity gradient was responsible for flame blowout [3]. The cause for instability for the 0.65 cm ring was attributed to the fact that because the circumferential cavity was only 2.54 cm wide, the paired 0.65 cm air jets take up over half the cavity width and therefore create instability problems consistent to those discovered by Anthenien et al. [6] while using slots to impart the cavity swirl.

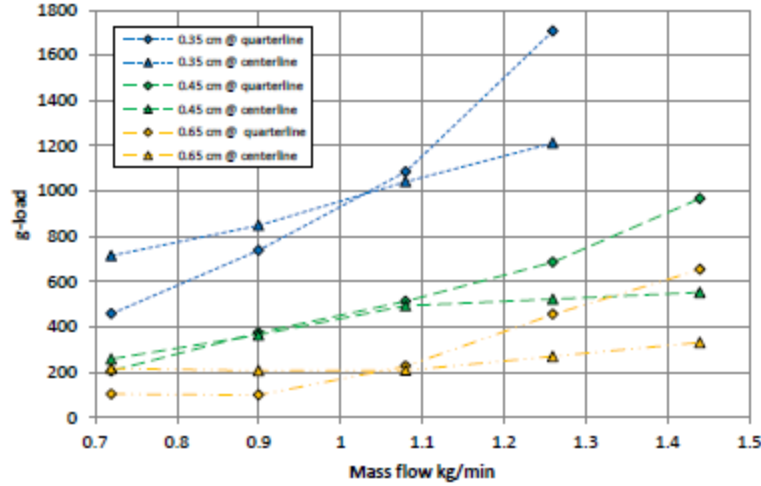


**Figure 16: G-loading data for 3.24 kg/min core and  $\Phi=1.76$  [3]**

In an effort to continue the work of Anderson et al. [9], Wilson [3] tested the impact of swirl direction on the AFIT rig. The air injection rings were designed such that they could be installed to provide swirl both CW, interacting with the suction side of the hybrid vane, and CCW, interacting with the pressure side of the hybrid vane. Using the 0.45 cm jet diameter ring and a core-to-cavity airflow split of 3.24/1.08 kg/min and an equivalence ratio of 1.76, the effects of swirling CW and CCW were analyzed. Figure 17 explains the direction of swirl and how the combustion products interact with the centerbody and core flow. A consistent flame profile was seen when the flow was swirled CW with the combustion products migrating inwards toward the core flow and along the suction side of the hybrid vane. As was the case in the work conducted by Andersen et al. [9], when the flow was swirled CCW a substantial increase in unsteadiness was observed. It was hypothesized that the unsteadiness arose as a result of the flow in the cavity having to turn approximately  $135^\circ$  to enter the core flow along the

pressure side of the hybrid vane [3]. A greater pressure loss at the exit was also observed when the flow was swirled CCW.

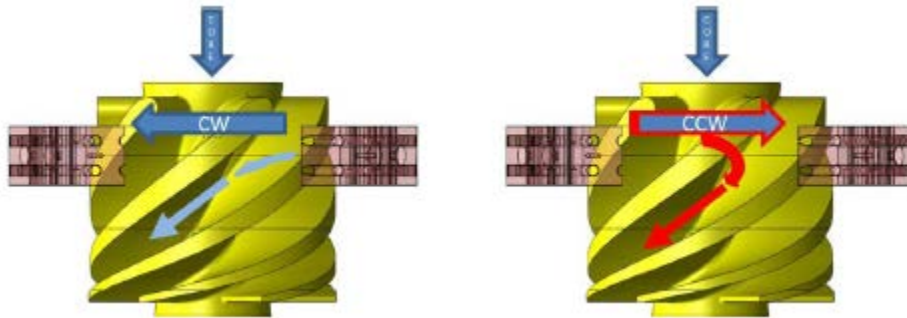


**Figure 17: Migration flow path for CW (left) and CCW (right) [3]**

## 2.4 Fuel Spray Basics

In the field of combustion, the process of transforming a liquid into a finely atomized spray is of utmost importance. As gas turbine engine technology continues to advance, researchers are constantly looking for innovations which increase engine capabilities and efficiencies. When talking about combustion in a gas turbine engine, the properties of a fuel spray are an important factor greatly affecting engine efficiency. The process that transforms liquid fuel into a spray consisting of a multitude of droplets is known as atomization [11]. Combustion is dependent on the effective atomization of fuel due to the increase in specific surface area and the achievement of high rates of mixing and evaporation [11]. A gas turbine engine benefits from a reduction in the mean fuel drop size due the higher volumetric heat release rates, easier light-up, wider burning range, and lower exhaust pollutant emissions [11].



### 2.4.1 Atomization of Liquid Jets

Atomization involves the interaction of consolidating and disruptive forces acting on a jet of liquid. The process of atomization can be further characterized as a disruption of surface tension – a consolidating force – by both internal and external forces. The viscosity ( $\mu$ ) and surface tension ( $\sigma$ ) of a liquid provide a stabilizing influence. If no disruptive forces are present, surface tension will pull the liquid into the form of a perfect sphere since this shape has the minimum surface energy [11]. The viscosity and surface tension of the liquid act as a stabilizing influence and help maintain the spherical shape of a droplet. External forces, such as aerodynamic forces, oppose the consolidating forces and act in a disruptive fashion. Breakup of the liquid occurs when the magnitude of the disruptive forces exceeds the consolidation surface tension force [11]. The process of liquid droplet breakup continues until a stable droplet size is attained. For any liquid, the initial breakup condition is achieved when the aerodynamic drag equals the surface tension force. Lefebvre provides the initial condition for breakup in Equation (2.1) [11].

$$C_D \frac{\pi D^2}{4} 0.5 \rho_A U_R^2 = \pi D \sigma \quad (2.1)$$

Where:

$C_D$  = the coefficient of drag

$D$  = the diameter of a drop

$\rho_A$  = the density of air

$U_R$  = the relative velocity

Equation (2.1) can be rearranged as a ratio of the disruptive aerodynamic forces to the consolidating surface tension forces, defined as the Weber number ( $We$ ), shown in

Equation (2.2). The higher the Weber number, the greater the disruptive forces compared to the consolidating forces [11].

$$\left(\frac{\rho_A U_R^2 D}{\sigma}\right)_{crit} = \frac{8}{C_D} \quad (2.2)$$

$$We_{crit} = \frac{8}{C_D}$$

$We_{crit}$  is the Weber number at the critical condition for breakup in which the largest diameter droplet will form. Rearranging Equation (2.1) once more, it is possible to calculate the maximum stable droplet size for a relative velocity, as well as the critical relative velocity at which a drop will begin breakup, shown in Equation (2.3) and Equation (2.4) respectively.

$$D_{max} = \frac{8\sigma}{C_D \rho_A U_R^2} \quad (2.3)$$

$$U_{Rcrit} = \sqrt{\frac{8\sigma}{C_D \rho_A D}} \quad (2.4)$$

Atomization consists of two processes known as *primary* and *secondary* atomization. When considering a liquid jet that exits a nozzle in continuous, cylindrical form, primary atomization begins when oscillations and perturbations are caused by the interaction of the consolidating and disruptive forces [11]. As the oscillations and perturbations increase in intensity, the continuous, cylindrical body of water exiting the jet will break apart into drops [11]. During the process of primary atomization, some of the drops surpass the critical size and will further break apart into drops of a smaller size until stability is reached. The additional break up of unstable drops is known as secondary atomization.

The way a liquid jet disintegrates into particles can be divided into different regimes of break-up. Lefebvre asserts that the most commonly quoted criteria for classifying jet disintegration are the criteria proposed by Ohnesorge [12]. Using photographic records, Ohnesorge was able to classify jet disintegration according to the relative importance of inertial, gravitational, surface tension, and viscous forces [12]. The process of classifying liquid jet disintegration involves comparing the liquid Reynolds number ( $Re_{liquid}$ ), a ratio of inertial to viscous forces, and another dimensionless number now known as the Ohnesorge number ( $Oh$ ). The Reynolds number and Ohnesorge number are shown in Equation (2.5) and Equation (2.6), respectively.

$$Re_{liquid} = \frac{\rho_{liquid} V_{liquid} D}{\mu_{liquid}} \quad (2.5)$$

$$Oh = \frac{\mu_{liquid}}{\sqrt{\rho_{liquid} \sigma_{liquid} d_0}} \quad (2.6)$$

Where:

$\mu_{liquid}$  = liquid kinematic viscosity ( $m^2/s$ )

$d_0$  = injector orifice diameter (m)

Ohnesorge [12] was able to show that the break-up of a liquid jet could be separated into the three regions which are shown in Figure 18. The first region deals with relatively low Reynolds numbers. In the first region, the jet breaks-up into large drops of consistent size [11]. The second region of jet disintegration occurs at intermediate Reynolds numbers and produces drops with a large variance in size. The third region of jet disintegration occurs at high Reynolds numbers where atomization occurs quickly and is complete within a short distance from the exit of the nozzle [11].

For practical purposes of atomization, most nozzles do not produce a jet of liquid, rather they form a flat or conical sheet of liquid. Fuel nozzles used in jet turbine engines primarily produce conical atomization patterns. The conical pattern of atomization can be produced if a liquid flowing through a pipe is deflected by some angle through an annular orifice [11]. Another way to create a conical atomization pattern is to impart a tangential velocity component to the liquid as it exits a nozzle by flowing the liquid through tangential or helical slots [11]. The theory to describe atomization due to hollow-cone, pressure-swirl nozzles is still under development.

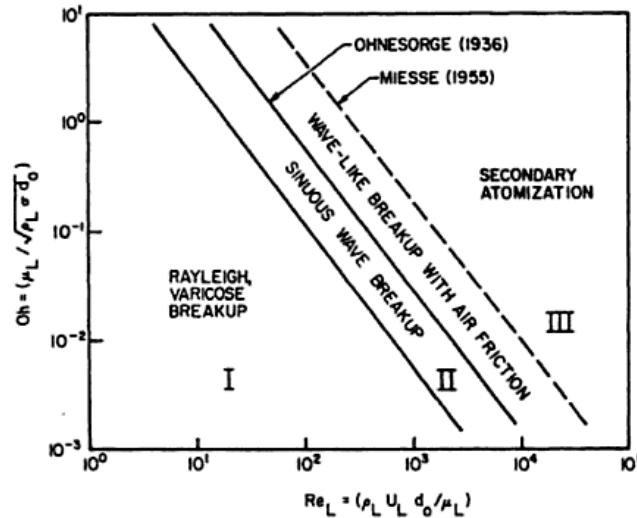


**Figure 18: Classification of modes of disintegration [12]**

Three modes of sheet disintegration proposed by Fraser and Eisenklam [13] are rim, wave, and perforated-sheet disintegration. Sheet disintegration in rim mode is caused by surface tension forces which cause the free edge of a liquid sheet to form a thick rim. The thick rim of liquid then breaks up into drops according to the same theory associated with the disintegration of a free jet described above. The process of rim disintegration tends to produce large drops and is most prevalent when the liquid being

atomized possesses a high viscosity and surface tension [13]. The wave form of disintegration occurs when an oscillation is present in a sheet of liquid and the liquid breaks apart in conjunction with the wavelength of the oscillation. Once the wave of liquid breaks apart from the main sheet, surface tension forces cause the liquid to contract and disintegrate into drops. The third form of liquid sheet disintegration is perforated-sheet disintegration. During perforated-sheet disintegration, multiple holes, or perforations, form in the liquid sheet. Each hole grows in size and creates its own rim until the rims of adjacent holes combine and ultimately break up into drops.

#### **2.4.2 Fuel Spray Analysis in the UCC**

Conrad [14] conducted an initial qualitative investigation into fuel spray patterns under g-loading. JP-8 was injected into the circumferential cavity through a pressure swirl nozzle with a flow number of 0.3 at a constant flow rate of 20 mL/min while the core air flow was fixed at 2.0 kg/min[14]. The spray from the fuel nozzle was then observed at g-loads of 0, 822, 1789, and 3249. At a g-load of zero, the fuel was atomized and ejected into the cavity in conical fashion, however it was noted that the cone was not at the maximum spray angle due to a low fuel flow rate [14]. Increasing the g-load in the cavity caused the fuel spray to be swept further downstream while also decreasing the width of the spray. At a g-load of 3249, there was no noticeable broadening of the fuel spray and the spray was rapidly swept towards the OD of the combustor ring [14]. High speed video images of the four test cases are compared in Figure 19.

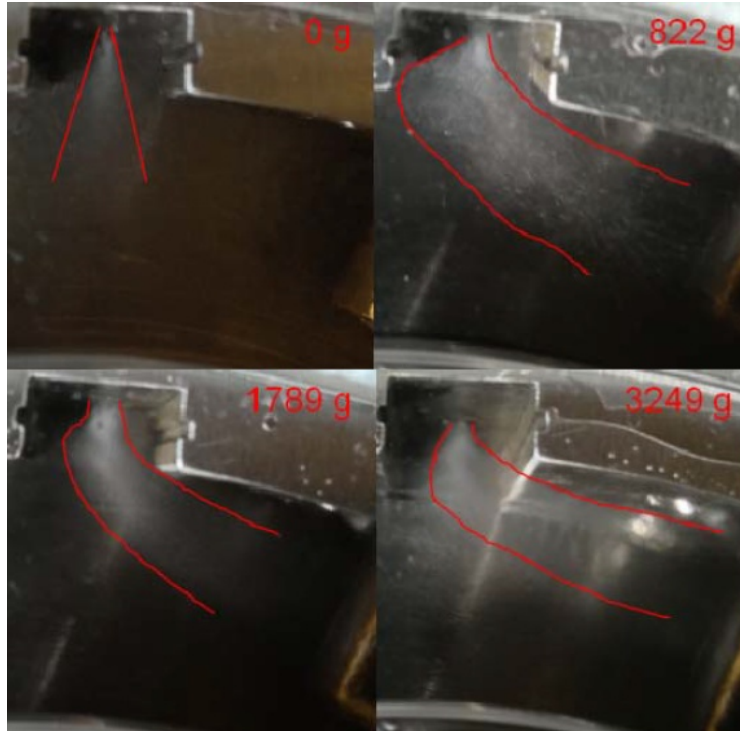


**Figure 19: Fuel spray testing at varying g-loading [14]**

## **2.5 Phase Doppler Particle Anemometry (PDPA)**

Due to the development of continuous wave gas lasers, the Doppler Effect can now be utilized as part of a non-intrusive, optical technique for measuring the velocity of gases, solids, or liquids [15]. This technique for measuring velocities is known as Laser Doppler Anemometry (LDA). In addition to LDA, PDPA utilizes a particle analyzer to process data about individual particles rather than just the particle velocity. PDPA is a unique and beneficial fluid flow measurement technique because it is a non-contact means of optical measurement. Focused laser beams are used to measure the flow velocity without disturbing the flow during measurement. The only requirements to make measurements are a transparent medium with a suitable concentration of tracer particles and optical access to the flow [15]. PDPA devices are capable of measuring

velocity in three dimensions along with particle sizes and distributions. The knowledge gained from particle velocity and size greatly aids in the characterization of a flow field.

### 2.5.1 Laser Doppler Anemometry Theory

The properties of spatial and temporal coherence of a gas laser make it a well suited instrument for measuring mechanical properties [15]. Gas lasers create beams with an intensity defined by a Gaussian distribution, and the edges of the laser beam are defined as the point where the edge-intensity is equal to  $\frac{1}{e^2}$  or 13% of the core intensity [15]. The most precise measurements are taken in the beam waist of a given laser beam. The beam waist is the point at which the cross section reaches its smallest value [15]. Measurement precision is greatest in the beam waist because the wavefronts are straight in this area, after passing through the beam waist, the wavefronts are curved. Figure 20 depicts a laser beam with a Gaussian intensity distribution along with showing the beam waist ( $d_0$ ) and transition of straight wavefronts in the beam waist to curved wavefronts.

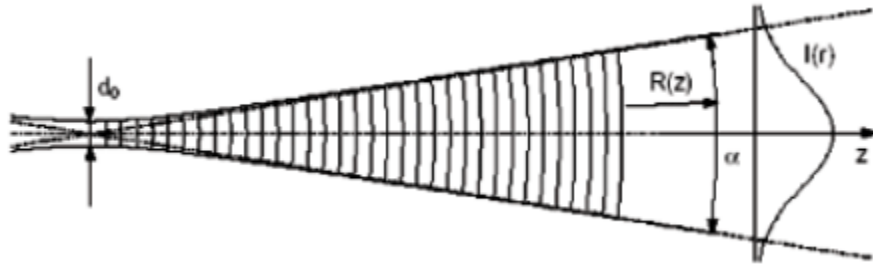


**Figure 20: Laser beam with Gaussian intensity distribution [15]**

### 2.5.2 Doppler Effect

The technique of LDA is based in measuring the Doppler shift of the light reflected and/or refracted from the particle being measured. LDA operates on the principle of Lorenz-Mie scattering, which applies when the size of the particle is comparable to the wavelength of the light. Lorenz-Mie scattering theory asserts that light is scattered in all directions at once; however, only the light reflected in the direction of the receiver is considered for measurements [15]. The incoming light from the laser has a velocity of  $c$  and a frequency of  $f_i$ . The movement of the particle being measured causes the frequency of the light with respect to the particle to be  $f_p$ , due to a Doppler-shift, and is scattered toward the receiver [15]. The frequency of the light reaching the receiver can be calculated using Doppler-theory given in Equation (2.7).

$$f_s = f_i \cdot \frac{1 - q_i \cdot \left(\frac{U}{c}\right)}{1 - q_s \cdot \left(\frac{U}{c}\right)} \quad (2.7)$$

Where:

$q_i$  = unit vector describing the direction of incoming light

$q_s$  = unit vector describing the direction of scattered light

The frequency of the incoming laser,  $f_i$ , is known and the receiver measures the Doppler-shifted frequency which then allows for the velocity of the particle,  $U$ , to be calculated. It is important to note that frequency change due to the movement of the particle can only be measured directly for high particle velocities [15].

Most LDA systems use at least two laser beams for measurements. Light is scattered toward the receiver at different frequencies from both of the incoming laser beams due to the different angles of the laser beams [15]. When the two beams of



slightly different frequency are crossed, they interfere with each other constructively and destructively creating a beat frequency also known as the Doppler frequency ( $f_D$ ). The Doppler frequency is mathematically explained in Equation (2.8).

$$f_D = u_x \cdot \frac{2 \sin\left(\frac{\theta}{2}\right)}{\lambda} \quad (2.8)$$

Where:

$\theta$  = the angle between the incoming laser beams

$\lambda$  = the wavelength of the laser beams

$u_x$  = particle velocity.

The Doppler frequency can be measured by the receiver according to the changes in the intensity of the light reflected from the particle [15]. Equation (2.8) shows that the Doppler frequency is proportional to the component of velocity being measured, and by rearranging the equation it is possible to solve for the given component of the particle velocity.

The fringe model is an easier way to visually represent the Doppler frequency. Figure 21 visualizes the intersection of two coherent laser beams at their beam waists. When the beams intersect, an interference pattern is created of parallel planes of constructive (light) and destructive (darkness) interference. The planes created by the interference are called fringes, and the distance between fringes ( $\delta_f$ ) is calculated based on the wavelength of the laser and the angle between the crossing beams and is calculated using Equation (2.9). As a particle moves through the probe volume the intensity of reflected light varies with a frequency proportional to the component of the particle velocity being measured [15]. The more fringes that a particle travels through the greater the accuracy of the measurement.

$$\delta_f = \frac{\lambda}{2 \sin\left(\frac{\theta}{2}\right)} \quad (2.9)$$

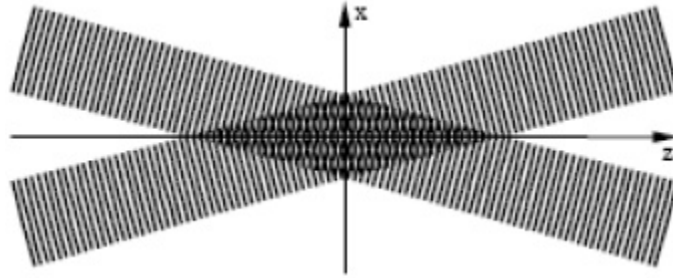


**Figure 21: Fringe pattern created by two coherent, vertically polarized laser beams [15]**

There are three different set ups for a LDA system to collect light: backscatter, forward scatter, and off-axis scattering. Due to the typical size of the particles being investigated most of the light is scattered away from the direction from which the laser beams emanate. When LDA was in its infancy, forward scattering was used which meant a receiver had to be placed in a location opposite the laser beam transmitter. The amount of backscattered light is significantly smaller than forward scatter; however, with advances in technology, it is possible to collect accurate information using the fainter backscatter signals. Using backscatter allows for the receiving and transmitting optics to be located in the same housing and eliminates the hardship of aligning the receiver. Off axis scattering is beneficial because the LDA system uses a separate receiver to look at the probe volume at an angle, effectively focusing on a smaller area in which measurements are made. Due to the Gaussian nature of laser beams, the probe volume created by the intersecting laser beams is elliptical. The elongated elliptical probe volume could be subject to velocity gradients where particles moving through the edges

of the volume are moving at different speeds than particles moving through the center.

Figure 22 shows how using off-axis scattering reduces the effective size of the measuring volume.

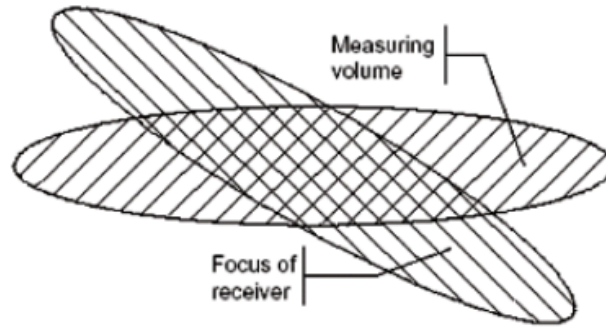


**Figure 22: Off-axis scattering [15]**

### **2.5.3 Phase Doppler Particle Anemometry**

Phase Doppler Particle Anemometry (PDPA) goes one step further than LDA. In addition to measuring velocity components of particles, the particle diameter is able to be measured by incorporating an additional photo-detector in the receiver.

The difference in optical path length for the reflections from the two incident beams changes with the position of the photo-detector. This means that, when the particle passes through the measuring volume, both photo-detectors receive a Doppler burst of the same frequency, but the phases of the two bursts vary with the angular position of the detectors [15].

The phase difference between the two Doppler bursts are dependent on the size of the particle. Figure 23 depicts how the phase difference changes with respect to the particle size.

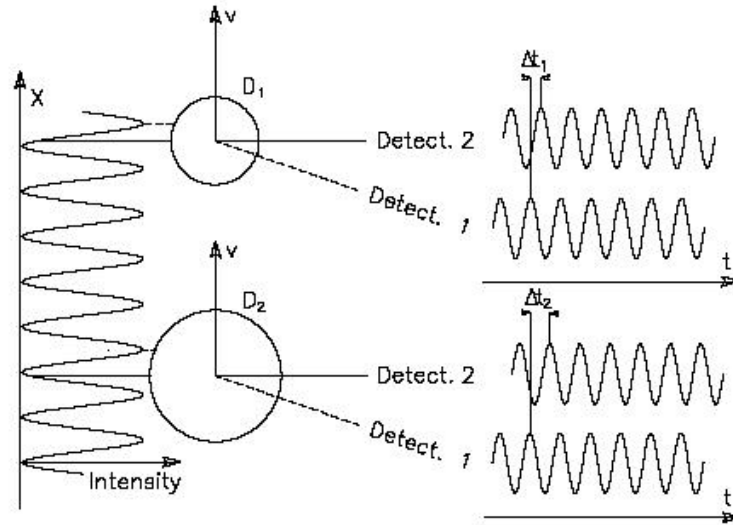


**Figure 23: Change in phase difference due to particle size [15]**

## 2.6 Summary

Characterizing the combustion process within the UCC is an ongoing effort. Before the UCC can be used as a main combustor on jet engines, it must be thoroughly evaluated and understood. The work previously discussed has significantly improved understanding of the combustion process taking place within the UCC. One area of research that still lacks information is the characterization of fuel sprays in the high g-loaded environment present inside the circumferential cavity of the UCC. Conrad [14] conducted rudimentary qualitative tests by taking high speed video of the fuel sprays under different g-loadings; however, they were only able to develop hypotheses from the images that were captured. No quantitative data was able to be obtained from the photographs taken with the high speed camera.

Using a nonintrusive measurement technique such as PDPA allows for a much needed quantitative characterization of the UCC. Characterizing the fuel spray patterns

under g-loads will lead to more efficient combustion. As detailed by Anderson et al. [9] and Wilson [3], there are significant stability differences when the UCC is operated with the circumferential cavity air rotating CW versus CCW. Analyzing fuel sprays under these conditions are critical to understanding the differences in stability. Once fuel spray patterns are characterized, research can go much further by studying areas such as where reactions are occurring in the cavity to optimize fuel injection. Research can also be conducted in the efforts to characterize the flow of combustion products through the UCC. This thesis details the first attempts to experimentally characterize spray patterns within the circumferential cavity of the UCC.

### **3. Methodology**

Testing was conducted on the AFIT full annular UCC designed by Wilson [3] to accomplish the research objective of analyzing spray patterns in the circumferential cavity of the UCC under high g-loads. All testing used water as the liquid injected into the UCC for the first attempt to characterize the spray patterns. Spray characterization was completed using Phase Doppler Particle Anemometry (PDPA) to measure two components of a droplet's velocity and the droplet diameter. The AFIT full annular UCC is designed with multiple optical access points, making the rig ideally suited for optical measurement techniques including PDPA. All experimental testing was conducted in the Combustion Optimization and Analysis Laser (COAL) Laboratory at AFIT.

#### **3.1 Full Annular UCC Design**

Wilson designed the AFIT full annular UCC to handle realistic conditions at the exit of a typical jet turbine engine compressor. Figure 24 depicts the AFIT full annulus UCC. Due to previous research, the rig was designed around a 70/30 core-to-cavity flow split. The design of the rig required a core flow of 18.9 kg/min to accurately simulate a full scale UCC. The circumferential cavity was sized with a cross sectional area of 2.54 cm by 2.54 cm based on a cavity flow of 8.1 kg/min of air which allowed the g-loading of 2000 in the cavity [3]. Both the core flow and cavity flow were able to be independently controlled to vary mass flow splits, aiding in the optimization efforts of the UCC. The circumferential cavity was also designed around equivalence ratios ranging from 1.5 to 2.0 because previous research performed by Zelina et al. [7] [8] indicated that these equivalence ratios were in the stable operating regime and also allowed for off design

studies [3]. The UCC was designed for compressor exit conditions of Mach 0.35 and  $35^\circ$  swirl [3]. To achieve this, the rig incorporated a centerbody with a pre-swirler, pictured in Figure 25, which initially imparts a swirl of  $35^\circ$  to the core flow to mimic compressor exit conditions. After the flow is turned prior to the circumferential cavity, it then flows through guide vanes based off the hybrid vane design of Bohan and Polanka [10] which turn and accelerate the flow to  $70^\circ$  and Mach 0.7-0.8 at the exit of the combustor in order to mimic the typical inlet conditions of a jet turbine engine.

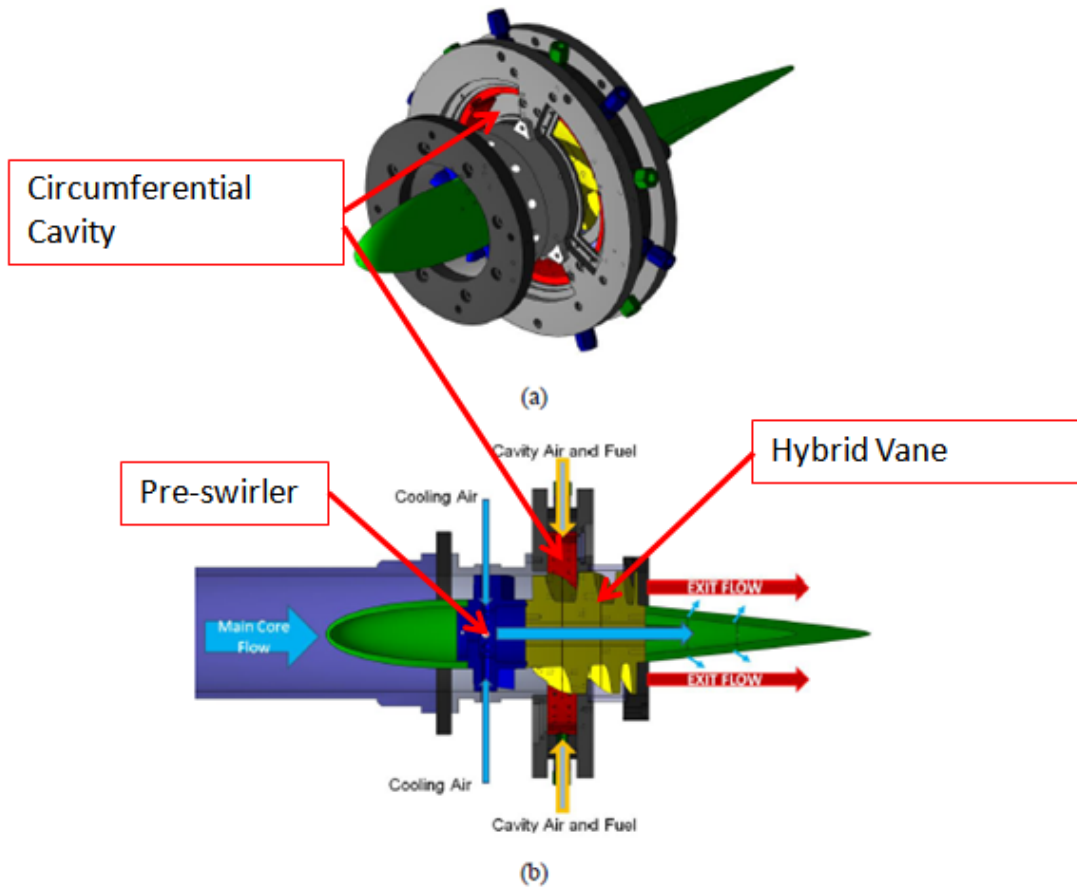


**Figure 24: Full annulus UCC (a) design and (b) main flow paths**

Wilson [3] designed two separate centerbodies to study the ability of controlling Rayleigh loss within the core. The first centerbody was designed with a straight taper of the ID from the front to rear while the second centerbody had an ID with a radius distribution designed to slow the flow and lessen Rayleigh losses [3]. The centerbodies were referred to as the Tapered Centerbody (TCB) and the Low Loss Centerbody (LLCB) respectively. More information about the centerbodies can be found in Wilson's Thesis [3]. The UCC was outfitted with LLCB throughout the testing process.

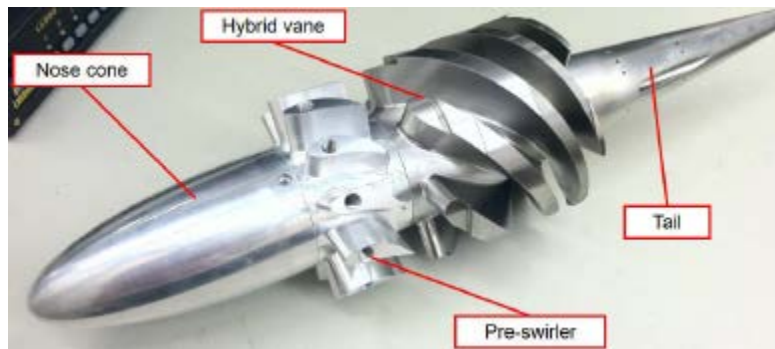


**Figure 25: UCC centerbody [3]**

All experimental data was taken inside the circumferential cavity of the UCC through the optical access windows. A depiction of the circumferential cavity is given in Figure 26. Six air lines and six fuel bolts are equally spaced around the OD of the cavity. Air is injected into a plenum located between the outer shell of the circumferential cavity and the air injection ring and then travels through the air injection ring. The air injection ring, pictured in Figure 27, is comprised of 48 paired injection holes, machined at  $35^\circ$  to the tangential direction which impart the swirl within the circumferential cavity. In addition to the air injection holes, six small fuel injection cavities measuring  $1.02 \times 0.51$  cm were machined into the air injection ring allowing for the injection of fuel into the



circumferential cavity. The radius of the air injection rings and thus the circumferential cavity is approximately 7.95 cm. When using gaseous fuel, the air injection ring allows for baffles to be inserted at the edge of the fuel injection cavity to reduce the momentum of the gaseous fuel and break up a single stream of fuel using the eight holes in the baffle. The air injection ring was designed to be easily removed allowing experiments to be conducted with rings of varying hole diameters. Previous research conducted by Wilson [3] found that an air injection ring with 0.45 cm diameter holes provided the most stable operating conditions under the greatest range of g-loads. Because of Wilson's findings the air injection ring with 0.45 cm diameter holes was used through the entirety of the experiment.

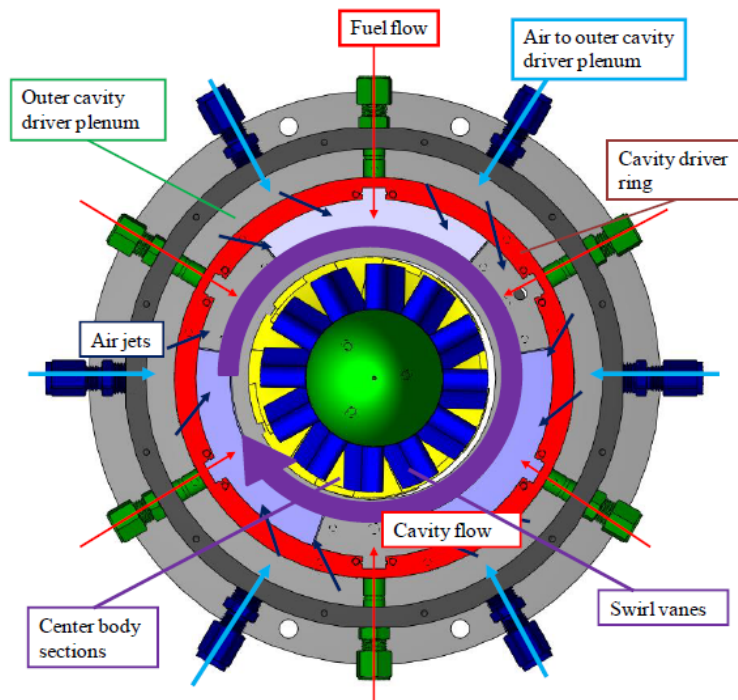


**Figure 26: Diagram of circumferential cavity [3]**

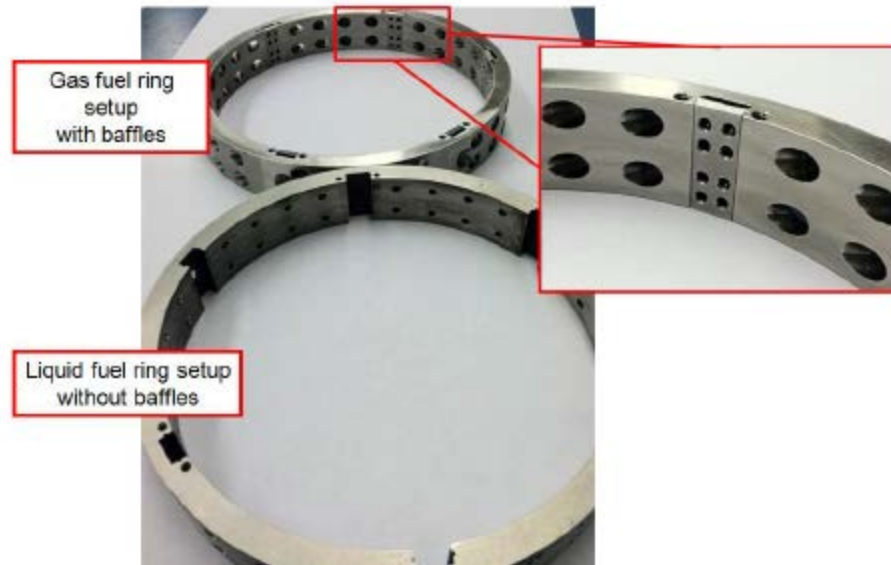


**Figure 27: Air injection rings [3]**

The six fuel bolts, equally spaced and located around the outside of the cavity, allowed for both liquid and gaseous fuel to be burned and studied within the cavity. The fuel bolt with an atomizing nozzle is shown in Figure 28. When left unaltered, the fuel bolts themselves were hollow, allowing gaseous fuel to flow through them and into the circumferential cavity. The inside diameter of the fuel bolts was threaded which allowed for atomizing fuel nozzles to be installed in order to study liquid fuels within the rig. Goodrich fuel nozzles with a 0.3 flow number were used to atomize water for all tests.

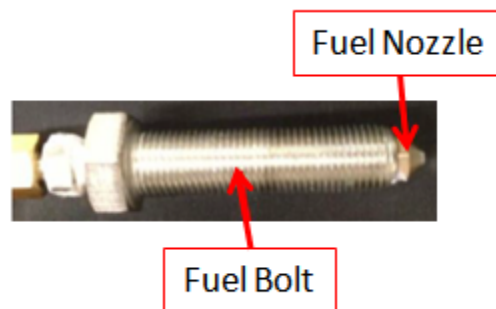


**Figure 28: Fuel plug with atomizing nozzle**

Water was pressurized and injected through the fuel nozzles using two ISCO Model 1000D syringe pumps seen in Figure 29. Two pumps were used in order to achieve a continuous flow of water. While one pump was injecting water through the fuel nozzle, the other pump was refilling. The two pumps were connected via a series of air actuated valves that allowed the pumps to switch between refilling and delivery without affecting the flow rate or pressure of the water being injected. The pumps were capable of providing constant flow rates up to 408 mL/min or constant pressurization up to 13.8 MPa [16]. The pressurized liquid was routed through steel tubing and a 0.5 micron Swagelok® fuel filter before being injected through the fuel bolts attached around the OD of the UCC.

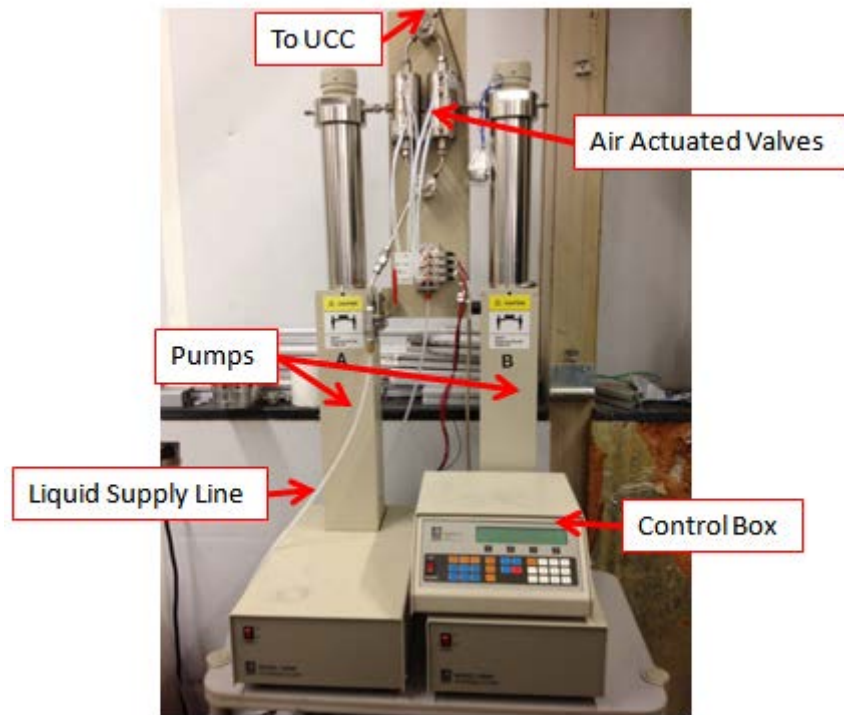


**Figure 29: ISCO Model 1000D syringe pumps**

The AFIT UCC was designed to allow maximum optical access to the circumferential cavity. The front plate of the UCC incorporates three equally spaced  $90^\circ$  windows for optical access while the back plate incorporates three equally spaced  $80^\circ$  windows. The front and back optical access points can be arranged in one of two configurations illustrated in Figure 30. In the first configuration, the optical windows on the front and back plates were aligned such that it is possible to see completely through the rig without any obstructions. The unobstructed alignment was ideal for laser diagnostics. The second configuration is such that the front and back plate windows are overlapped, creating a back drop. The second configuration is ideal for high speed video or photos. All experiments conducted for the research presented in this paper were accomplished with the unobstructed configuration. Multiple windows made of quartz and Plexiglas were manufactured for optical access. Quartz windows are used for experiments involving reacting flows due to the materials ability to withstand high temperatures. For experiments involving nonreacting flows, Plexiglas windows were used. Fiberfrax® ceramic felt was used to ensure a tight seal between the windows and the metal of the UCC as well as provide a thermal barrier between the metal and quartz during experiments involving reacting flows.



(a)



(b)

**Figure 30: UCC Optical access unobstructed (a) and with a background (b)**

Instrumentation panels were also fabricated which allowed access to measure temperature and pressure inside the circumferential cavity. The panels, shown in Figure 31, were designed to be interchangeable with the windows used for optical access. The instrumentation panel for the rear plate of the UCC had seven tapped holes while the front instrumentation panel had nine tapped holes. The tapped holes were all located at the mid radius of the circumferential cavity [3]. In addition to the windows and instrumentation panels, blank panels were also fabricated for use during experiments when optical access was not necessary.

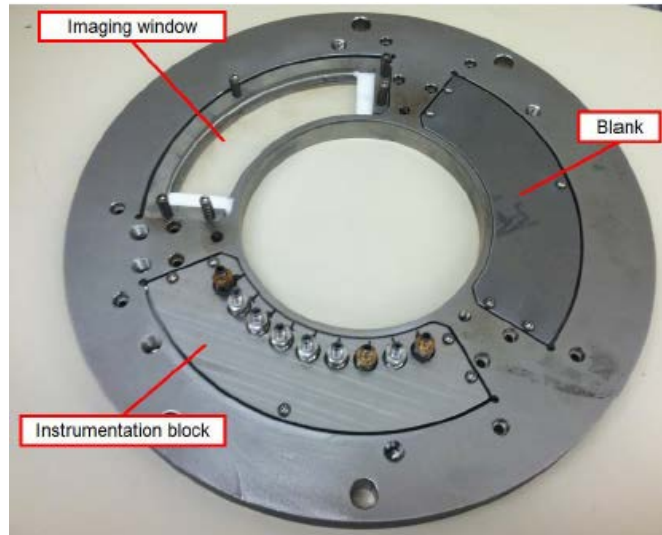


**Figure 31: Front face of the UCC with a window, instrumentation panel, and blank panel [3]**

The rear plate of the UCC was designed to receive an ethylene-air torch which was used to initiate combustion for reacting experiments. Figure 32 shows the ethylene-air torch. The torch consisted of a stainless steel manifold where air and ethylene were mixed and ignited by a spark plug. The resulting flame then traveled through a stainless steel tube and into the circumferential cavity, igniting the fuel.



**Figure 32: Ethylene-air ignition torch.**

The front plate, rear plate, and center body of the UCC along with the air injection rings and the outer ring containing the plenum were fabricated from Hastelloy-X, a nickel-based alloy. Wilson chose Hastelloy-X as the material for the UCC because of its low thermal expansion coefficients between 15.6 and 16.7  $\mu\text{m/m}^\circ\text{C}$  at 1000°C (1273K) [3].

### **3.2 Laboratory Air Supply**

Three compressors were used to generate the air flow required for the UCC. An Ingersoll Rand H50A-SD, 50 hp, oil-free compressor was located outside the East wall of the COAL lab. This compressor was capable of providing air flow rates of 1 kg/s at atmospheric pressure. Condensation was removed from the compressed air through built in dryers. The other two compressors were the AFIT 50 hp Ingersoll Rand compressors capable of providing a total flow rate of 0.15 kg/s.

Flow from the COAL lab compressor and the two AFIT compressors entered the COAL lab and were split into three independently operated air lines through a series of valves in order to provide air to the UCC. The plumbing of the air supply lines is shown in Figure 33. A 7.62 cm line provided the air necessary for the core flow while a 3.81 cm line provided the air necessary for the circumferential cavity flow. A third 1.91 cm line provided cooling air necessary for cooling the rig during combustion experiments. A detailed depiction of the three air lines is presented in Figure 34. Both the 7.62 cm and 3.81 cm lines were equipped with Flowserve MaxFlo 3 valves capable of providing 0.6 kg/s and 0.3 kg/s of air respectively. The 7.62 cm and 3.81 cm line incorporated Fisher 99 and Fisher 299H pressure reducers, respectively, to maintain a constant



pressure in the line and reduce fluctuations in mass flow. The 1.91 cm was able to flow a maximum of 0.03 kg/s of air using an ITP and Badger control valve and Cashoo pressure reducer. All three lines utilized FT2 Fox Thermal instruments flow meters, calibrated by the manufacturer, to ensure proper mass flow rates were being maintained within  $\pm 1\%$ . The air supply lines were controlled by a laboratory computer running LabVIEW [17]. More details on the air supply lines and control systems can be found in Wilson's thesis [3].

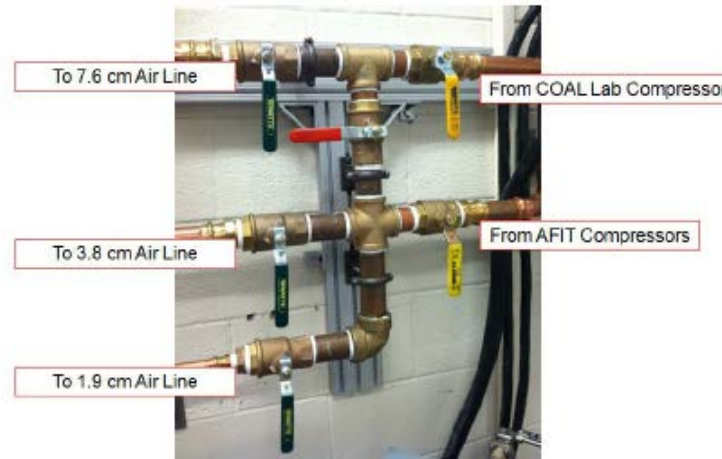


**Figure 33: Plumbing and splitting of incoming air [3].**

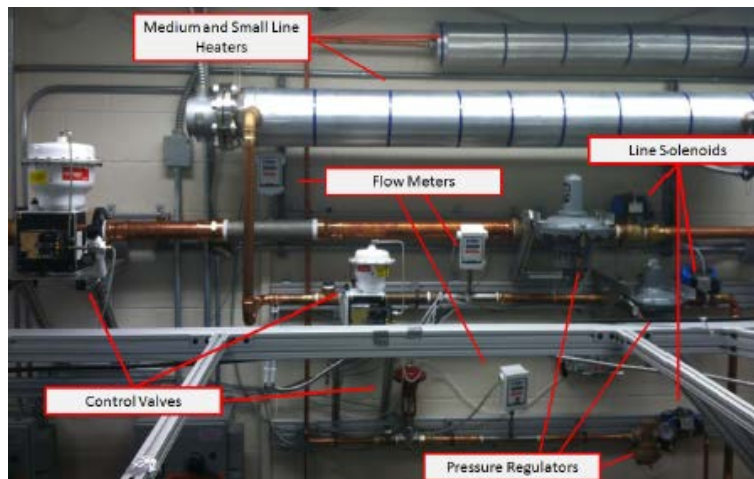


**Figure 34: Set up of the three air supply lines [3]**



The 7.62 cm line provided the air flow for the core of the UCC. Figure 35 shows how the core air was routed to the UCC. After passing through the Flowserve valve, the air was then routed through a flexible, corrugated plastic tube and turned through a 90° PVC elbow connected to a 10.16 cm diameter PVC pipe which connected to the inlet of the UCC. In order to make the inlet conditions of the UCC as uniform as possible, the length of the PVC pipe was approximately 12 diameters.

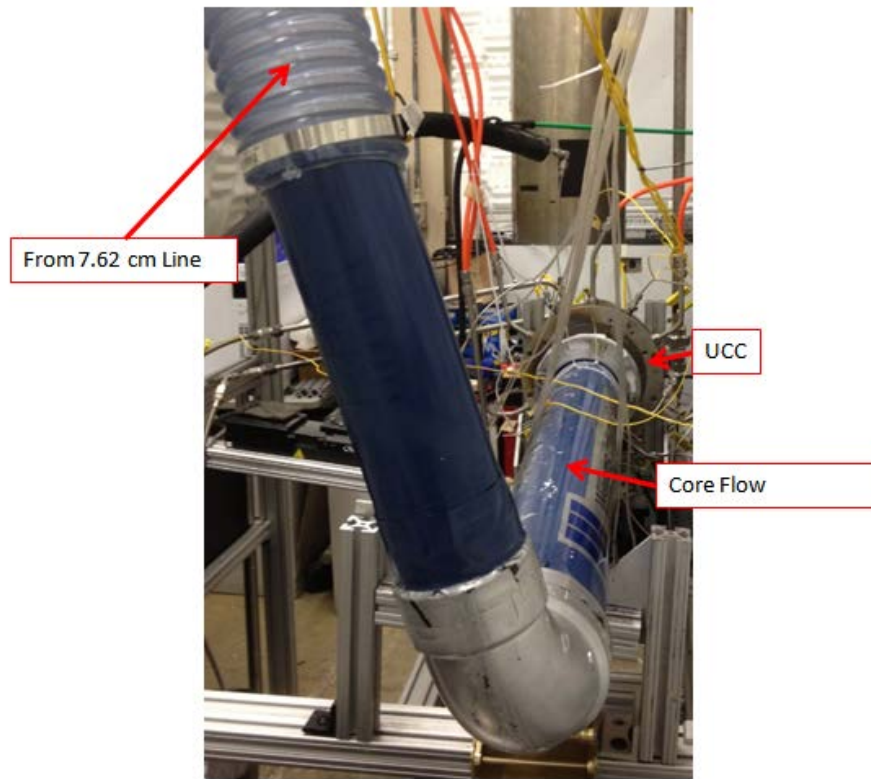


**Figure 35: Inlet of the core flow to the UCC**

The air in the circumferential cavity was provided by the 3.81 cm line. Figure 36 shows the cavity air routing. After passing through the Flowserve valve, the air was routed through heaters and then to a location above the circumferential cavity. The air supply line was then split six ways and traveled through flexible tubing to six equally spaced locations around the OD of the cavity.

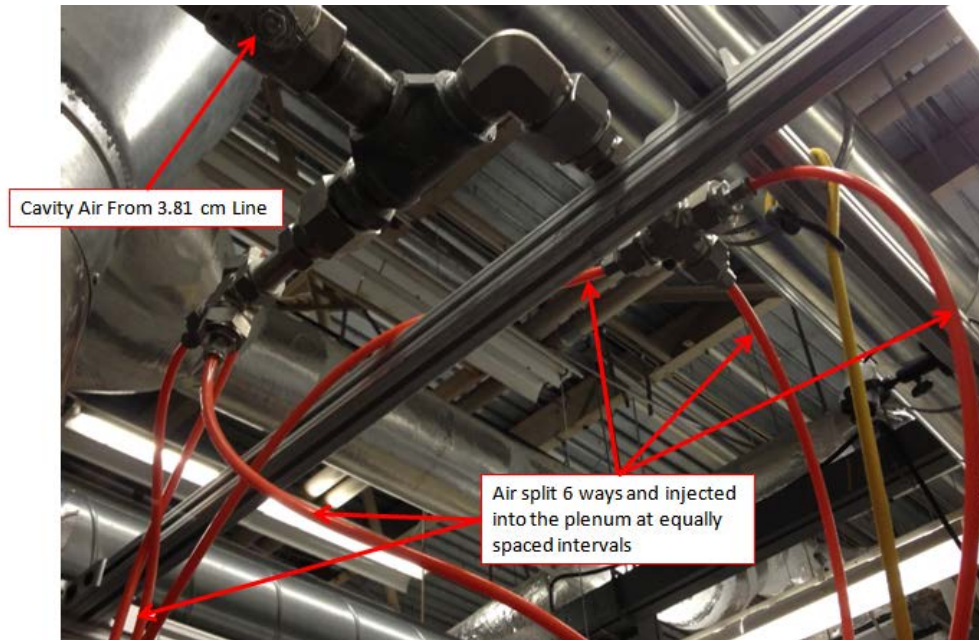


**Figure 36: Routing of the cavity air.**

### **3.3 Pressure and Temperature Measurements**

Pitot tubes were used record static and total pressures at various locations throughout the experiment. Pressure measurements were recorded inside the circumferential cavity by inserting pitot tubes through the tapped holes on the UCC instrumentation panels as seen in Figure 37. The pressures were measured using an Esterline DTC Initium pressure acquisition system and a 32 port ESP-HD PSID pressure scanner seen in Figure 38. The Initium pressure acquisition system was able to be automatically calibrated using shop air at 80 PSI and was connected to the laboratory computer using ethernet. Prior to recording any pressure measurements while operating the UCC, the pressure transducer was calibrated to ensure the values were accurate. The calibration process and results can be found in Appendix A.

In addition to pitot tubes, K-type thermocouples were also inserted into the instrumentation panel of the UCC to record the temperature inside the cavity. A

thermocouple connection panel seen in Figure 39 was made up of four boards with twelve plugs and allowed for up to 48 thermocouples to be used simultaneously if needed. The four boards were connected to the laboratory computer via four 12-line cables that ran to data acquisition modules (DAQ) manufactured by National Instruments (NI).

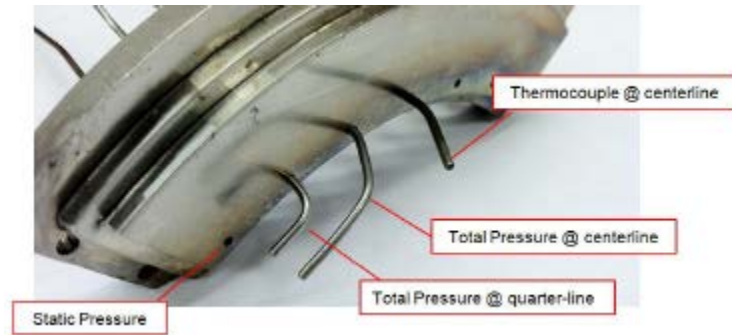
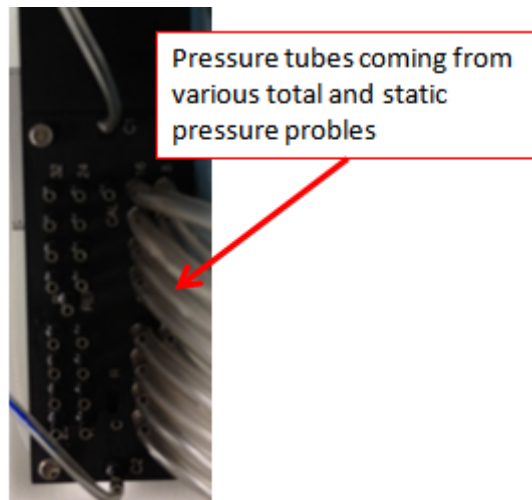


**Figure 37: Temperature and pressure instrumentation.**



**(a)**



**(b)**

**Figure 38: Initium Pressure acquisition system (a) 32 port pressure scanner (b)**



**Figure 39: Thermocouple plug board.**

It is essential to obtain temperature and pressure measurements inside the circumferential cavity in order to calculate the g-loading. Assuming compressible flow within the circumferential cavity, the Mach number for a subsonic compressible flow, assuming air is an ideal gas, was calculated using Equation (3.1),

$$M = \sqrt{\left( \left( \frac{P_T}{P} \right)^{\frac{\gamma-1}{\gamma}} - 1 \right) \frac{2}{\gamma-1}} \quad (3.1)$$

Where:

$P_T$  = the total pressure

$P$  = the static pressure

$\gamma$  = the ratio of specific heats.

With the Mach number known, the tangential velocity and g-loading were calculated using Equations (3.2) and (3.3).

$$V_{tan} = \sqrt{\gamma RT} \quad (3.2)$$

$$G - load = \frac{V_{tan}^2}{rg_c} \quad (3.3)$$

Where:

$V_{tan}$  = the tangential velocity

$R$  = the universal gas constant

$T$  = the temperature measured by the thermocouple

$r$  = the radius of the circumferential cavity  
 $g_c$  = the acceleration due to gravity

For all calculations conducted in this research, a value of  $\gamma = 1.4$  was used because measurements were recorded in a non-reacting flow and the value of  $R=287 \text{ J/(kg K)}$  for dry air was used. Multiple g-load was calculated multiple times at each individual operation conditions indicating the test rig was able to maintain a g-load within  $\pm 25 \text{ g}$ .

### **3.4 PDPA Setup**

PDPA is an excellent non-intrusive way used to measure the velocity and size of particles in a flow field. The specific characteristics of fuel injection into the circumferential cavity of the UCC have yet to be quantitatively studied and analyzed. Analysis needs to be conducted on fuel spray data to ensure that the proper amount and distribution of fuel is provided for the combustion process. The non-contact means by which PDPA measures the velocity and droplet size of particles made it an excellent system to characterize the fuel spray patterns within the circumferential cavity.

#### **3.4.1 General**

The PDPA experiment was conducted using an Argon-ion laser with an output power of 100 mW along with PDPA hardware and BSA Flow software manufactured by DANTEC. The beam emitted from the Argon-ion laser was directed into the FiberFlow where the beams traveled through a Bragg cell which operated at 40 MHz, creating shifted beams to eliminate the directional ambiguity in the measured velocity. Color separator hardware in the FiberFlow was used to separate the 488 and 514 nm beams. The four beams (the 488 nm and 514 nm beams and their respective shifted beams)

traveled through fiber optics and the transmitting optics which focused the four beams into one point. The data was collected using the DANTEC FiberPDA receiving optics seen in Figure 40. The presence of three photo-detectors allowed for two components of velocity to be measured as well as the diameter of the droplets.

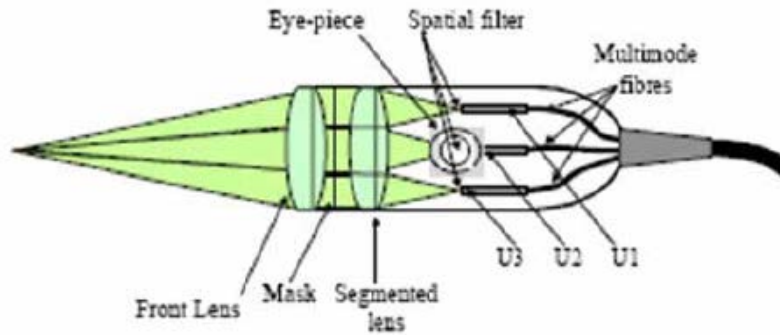


**Figure 40: DANTEC FiberPDA Probe [15]**

Tests were conducted at three g-loadings and two different pressure drops across the nozzle. Table 2 lists the various test cases. The test cases were designed to characterize the spray inside the circumferential cavity for the conditions at which the UCC was designed to operate.

**Table 2: Matrix of test scenarios.**

Case	Pressure Drop across Nozzle $\Delta P$ (MPa)	G-Load
1	0.7	300
2	1.4	300
3	0.7	1400
4	1.4	1400
5	0.7	5000
6	1.4	5000

### 3.4.2 Initial beam calibration and data collection

Prior to data being collected in the circumferential cavity of the UCC, it was

necessary to ensure the PDPA system was properly aligned and all four beams intersected at a single point. The lens affixed to the front of the transmitting optics had a focal length of 310 mm. To verify the four beams crossed at a single point, a magnification lens was set up slightly more than 310 mm from the transmitting optics which then projected the location of the beams on a sheet of white paper. The four beams were adjusted using the adjustment screws on the transmitter until the beams converged at one point. In addition to adjusting the location of the beams, the intensity of the beams was also adjusted using the fine and coarse adjustments on the color separator until a nominal value of approximately 10 mW was achieved for all four beams. The intensity of the beams was measured using an Ophir Nova laser power meter. The fine and coarse adjustment knobs on the color separator can be seen in Figure 41a while the adjustment screws on the transmitter and the can be seen in Figure 41b.

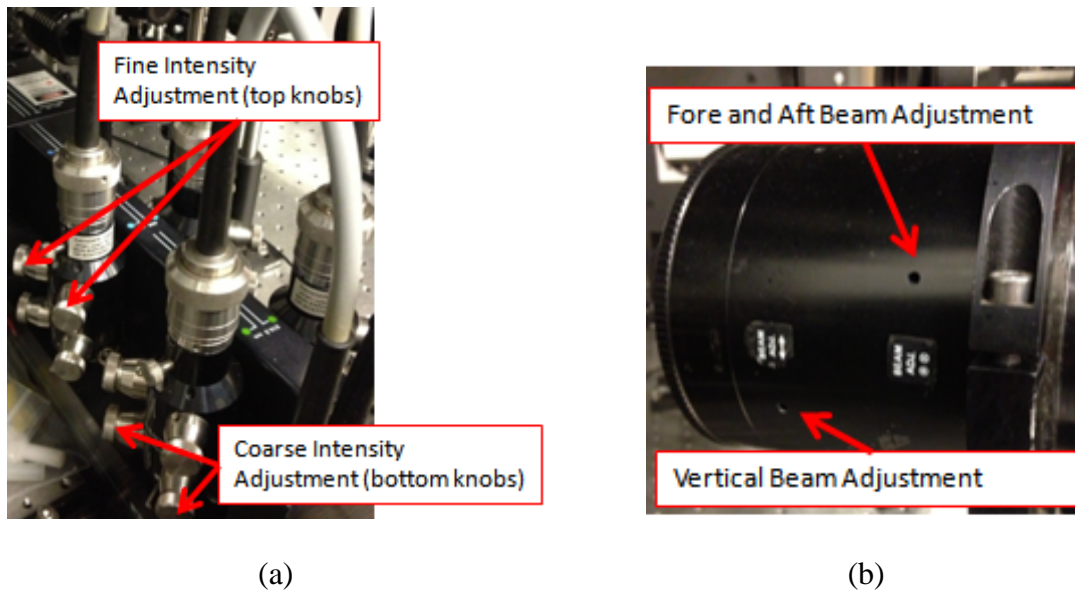


**Figure 41: PDPA transmitting optics and calibration screws.**

After the beams were calibrated, initial tests were conducted by spraying water



through a 0.3 flow number fuel nozzle in the open air of the laboratory. The water was delivered to the nozzle from a pressure vessel pressurized to 80 PSI using shop air.

Figure 42 shows the initial testing of the PDPA setup with a fuel nozzle atomizing water in open air. The initial test results are located in Appendix B.

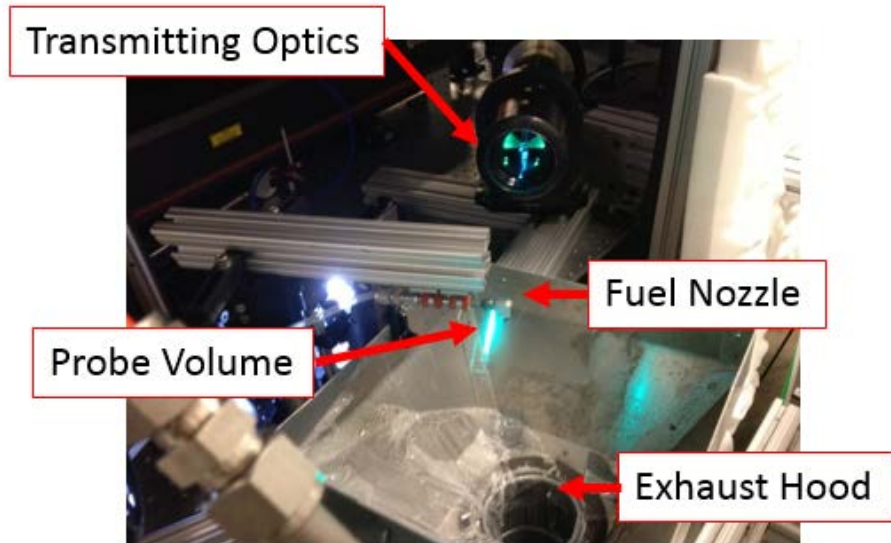
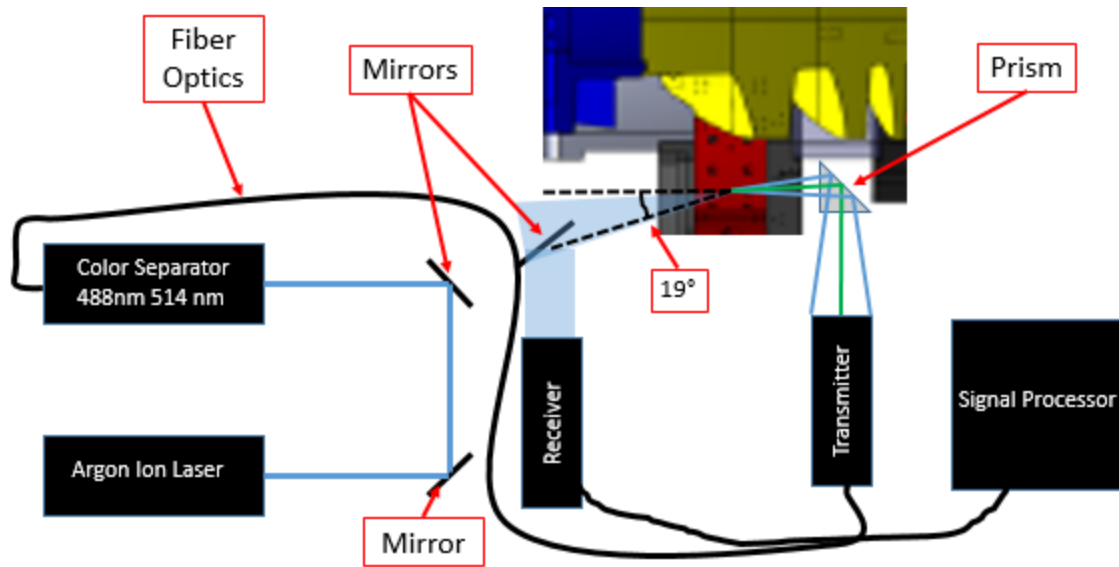


**Figure 42: Initial PDPA calibration using water in open air**

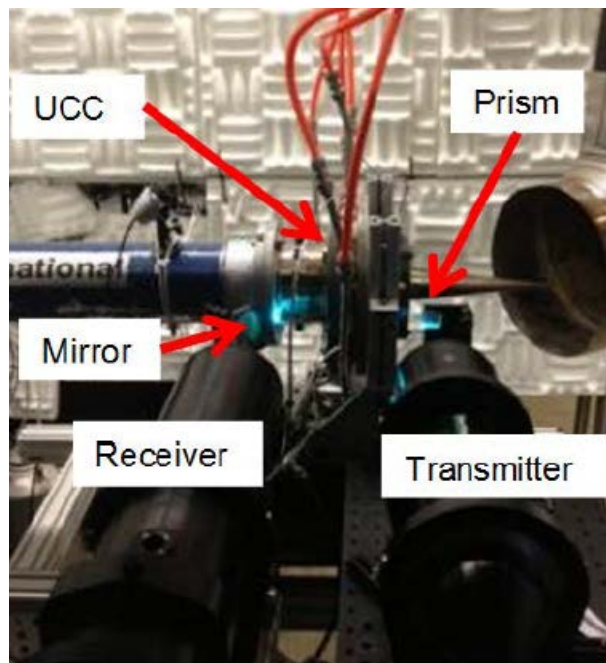
### **3.4.3 PDPA alignment with the UCC**

After successfully recording droplet data in the open air environment of the laboratory, the PDPA hardware was aligned with the UCC. Figure 43 depicts the setup and alignment of the hardware with respect to the UCC. The four beams left the transmitter through the 310 mm focal length lens and passed through a single prism that redirected the beams  $90^\circ$  through the Plexiglas window where they converged to one point in the center of the circumferential cavity. The reflected and refracted light was directed to the receiver via a mirror that was located  $19^\circ$  off axis from the beams. The information collected by the photo-detectors in the receiver was then processed by the software.





(a)



(b)

**Figure 43: Experimental setup configuration.**

### 3.4.4 Traversing system and data collection grid

A traversing system was devised to maximize the number of locations where data

was collected while minimizing the need to constantly align the optics of the PDPA system. Both the transmitter and prism were mounted on one traverse while the receiver and the off-axis mirror were mounted on another traverse. The traverses used were Newport traverses and they were controlled by a Newport ESP301 motion controller. The traverse and motion controller are shown in Figure 44. By mounting the receiver and transmitter on traverses and moving them simultaneously, it was possible to horizontally adjust the location of the measurement probe volume while maintaining system alignment. In addition to the horizontal movement provided by the traverses, the UCC test rig was mounted on a vertical translation stage which allowed the probe volume to be translated in the vertical direction relative to the rig.

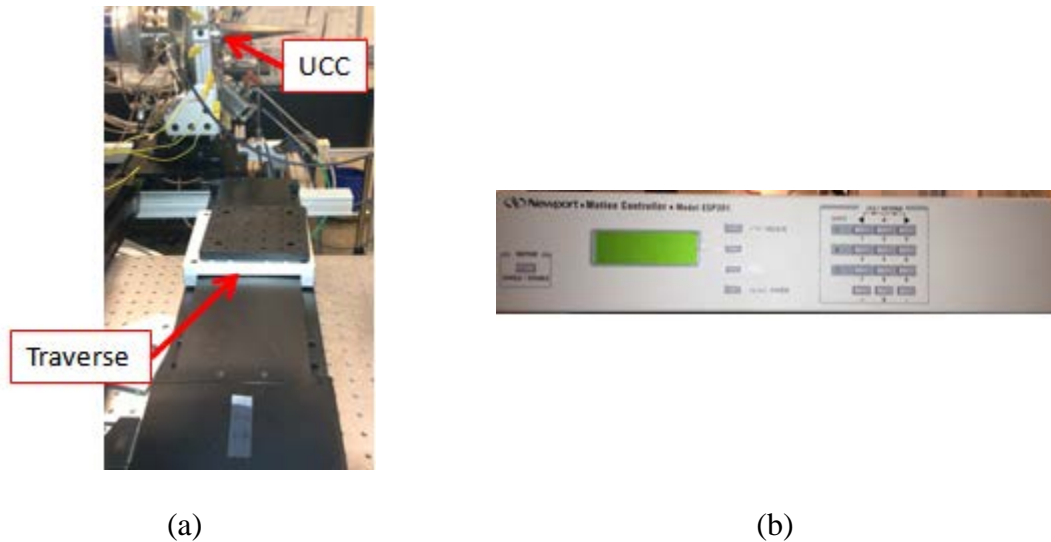


**Figure 44: Newport electronic traverse (a) and Newport traverse controller (b)**

The traversing system was setup using a Cartesian coordinate system. The initial starting position of (0,0) was located when the measuring probe was located in the same horizontal plane as the fuel nozzle at the point where the fuel injection cavity met the circumferential cavity. The positive x-direction was defined as moving toward the

centerline of the rig while the positive y-direction was defined as moving downward. Once the measuring probe was located at the starting point of (0,0), the traverse controller was zeroed and horizontal adjustments were made using the *Move Relative* mode. The *Move Relative* mode allowed the user to input various horizontal locations of the measuring probe, in millimeters, relative to the initial starting position of  $x=0$ . The horizontal height of the measuring probe was measured using a ruler fixed to the stationary portion of the test stand. As the vertical translation stage was adjusted to increase or decrease the height of the rig, measurements were recorded using the ruler and the top of the support pole to which the UCC was attached. Figure 45 illustrates how the height was measured.

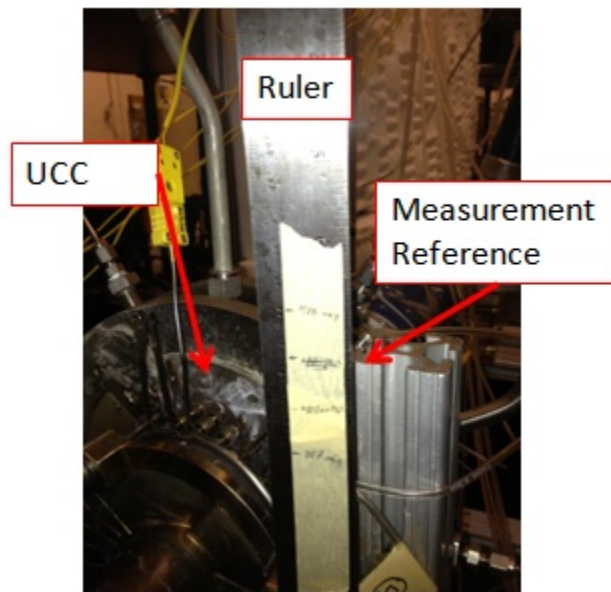


**Figure 45: Recording the vertical height of the measurement probe**

The location of points inside the circumferential cavity at which data was collected can be seen in Figure 46. Data for a cavity g-loading of 300 was initially recorded in 2 mm horizontal increments in planes located 10 mm above the fuel nozzle,

in line with the fuel nozzle, and 10, 20, 30 mm below the fuel nozzle for as long as the rig hardware allowed. For all subsequent test conditions an additional plane of data was collected 5 mm below the fuel nozzle at 1 mm horizontal increments in order to better characterize the initial conditions of the spray entering the circumferential cavity. In addition to the data collection plane 5 mm below the nozzle, data was also collected at 1 mm increments in the plane 30 mm below the fuel nozzle in an effort to characterize the spray at the further downstream location. The points shown in Figure 46 include extremes at which data was able to be recorded due to the maximum amount of travel in the vertical translation stage and the limited amount of horizontal movement allowed by the rig itself.

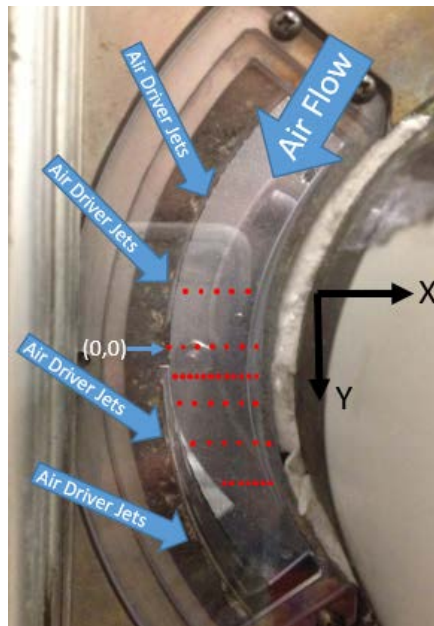


**Figure 46: Data collection grid**

### 3.4.5 BSA Flow Software Settings

The BSA Flow software processed and analyzed the light collected by the receiver. In order to accurately analyze the velocity and size of the particles inside the circumferential cavity, basic information about the PDPA setup was input into the software. Table 3 lists the values for all of the specifications needed for the software to accurately process the data collected by the receiver.

**Table 3: BSA Flow software specifications.**

Beam System U1		Beam System U2	
Wavelength	514 nm	Wavelength	488 nm
Focal length	310 mm	Focal length	310 mm
Beam diameter	1.35 mm	Beam diameter	1.35 mm
Expander ratio	1	Expander ratio	1
Beam spacing	38 mm	Beam spacing	38 mm
Fringe spacing	2.005 $\mu\text{m}$	Fringe spacing	2.114 $\mu\text{m}$
Frequency shift	40 MHz	Frequency shift	40 MHz
Center Frequency	7.88 m/s	Center Frequency	14.9 m/s
Bandwidth	31.54 m/s	Bandwidth	29.91 m/s
Signal gain	26 dB	Signal gain	26 dB
High Voltage Level	1000	High Voltage Level	1000
PDA Receiver		Flow Properties	
Receiver type	Fiber PDA	Particle name	Water
Scattering angle (deg)	19	Particle refractive index	1.334
Receiver focal length	310 mm	Medium name	Air
Receiver expander ratio	1	Medium refractive index	1
Fringe direction	Positive		
Scattering mode	Refraction		
Aperture mask	Mask A		
Spherical validation band (%)	25%		

As mentioned previously, both the transmitter and receiver were outfitted with 310 mm focal length lenses meaning that the four beams will intersect and create a probe volume 310 mm from the transmitter. The beam diameter, beam spacing, and expander ratio were determined by the hardware used. The diameter of the beam is the value

obtained at the beam waist determined by the Gaussian intensity distribution and the beam spacing is the distance between the beams leaving the transmitter.

The shifted and unshifted green (514 nm) beams were in the vertical plane and measured the vertical component of velocity, while the shifted and unshifted blue (488 nm) beams were in the horizontal plane and measured the horizontal component of velocity.

Velocity is measured as two beams overlap at the probe volume and create a volumetric fringe pattern with planes of high and low intensity. As the droplets move through the fringe pattern the scattered light intensity can be used to calculate the velocity if the fringe spacing is known. The fringe spacing is function of the wavelength of the beams and the angle at which the beams intersect. Using Equation (2.9) the fringe spacing for the 488 nm and 514 nm beams were found to be 2.005  $\mu\text{m}$  and 2.114  $\mu\text{m}$  respectively. The measurement probe volume can be calculated using the diameter of the beam waist and the angle at which the beams intersect given by Equations (3.4), (3.5), and (3.6).

$$dx = \frac{d_f}{\sin \frac{\theta}{2}} \quad (3.4)$$

$$dy = d_f \quad (3.5)$$

$$dz = \frac{d_f}{\cos \frac{\theta}{2}} \quad (3.6)$$

Where:

$dx, dy, dz$  = the dimensions of the volumetric measuring probe  
 $d_f$  = the waste diameter of the focused beam

$\theta$  = the angle at which the beams cross.

For the 488 nm laser beam, the dimensions of the probe volume were  $dx = 2.32$  mm,  $dy = 0.143$  mm,  $dz = 0.143$  mm. For the 514 nm laser beam, the dimensions of the probe volume were  $dx = 2.453$  mm,  $dy = 0.15$  mm,  $dz = 0.151$  mm.

The direction the fringes travel, due to the use of one shifted beam, have an effect on the accuracy of the particle size measurement. According to DANTEC, “The fringe direction setting affects the sign of the phase factors but not the Doppler frequency. Therefore, the direction of fringe motion affects the measurement of diameter but not the velocity measurement.” The fringe direction was set to positive for the purposes of this experiment.

Figure 47 shows a typical phase plot for the PDPA system. The phase plot illustrates the phase difference between photo-detectors U1 and U2 as a function of the phase difference between photo-detectors U1 and U3 [15]. DANTEC states, “The diagonal continuous line represents the theoretical relationship between the two phase differences for perfectly spherical particles.” The dashed lines on the phase plot represent the spherical validation tolerance band, which was set to 25% for the duration of data collection. The phase plot is used to ensure proper alignment and that the fringe direction is set correctly. When aligned correctly a cloud of dots will build up around the solid diagonal line predominately inside the tolerance band [15].

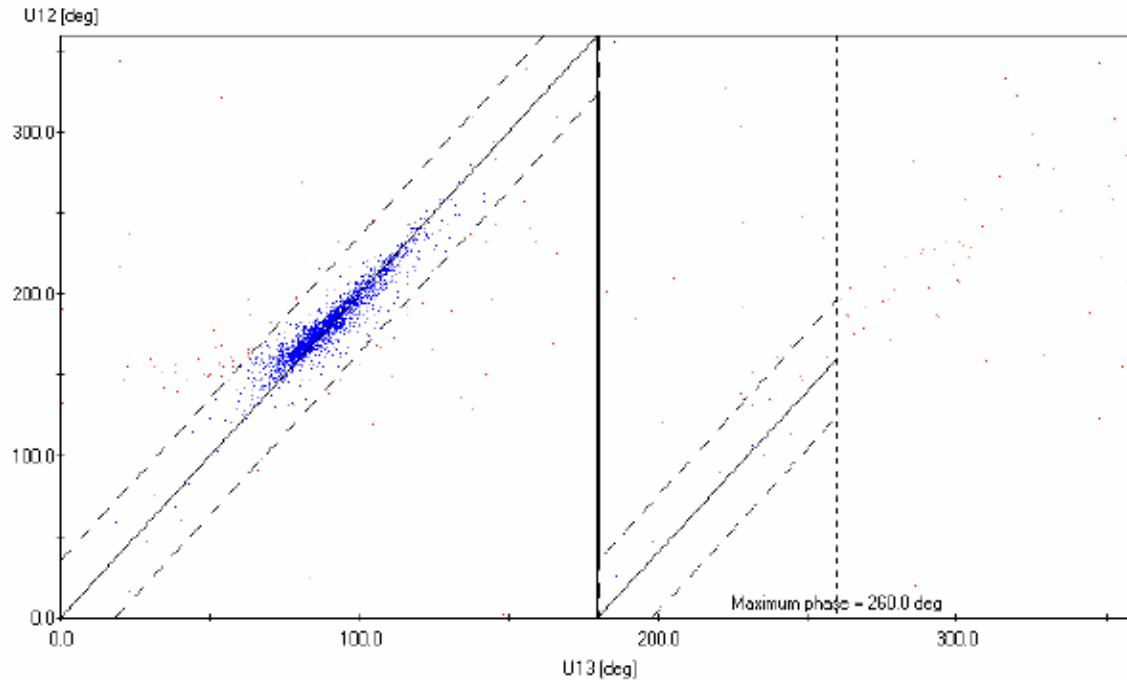


**Figure 47: Representative phase plot used to ensure alignment and fringe directions are set correctly [15]**

The scattering angle is the angle at which the receiver views the probe volume and is measured with respect to the direct forward scattering direction. A scattering angle of  $0^\circ$  would represent a setup where the receiver was positioned directly opposite the transmitter. The scatter angle was maintained at  $19^\circ$  throughout data collection for the entirety of the experiment and the mode of scattering was refraction.

The DANTEC PDPA system offers the choice of three aperture masks for the receiver. The three available aperture masks are labeled A, B, and C. A mask is the largest aperture and is used for small particles, B mask is a medium sized aperture for use with medium apertures, and C mask has the smallest apertures and is used for large particle measurement [15]. It is important to note that DANTEC does not give values segregating small, medium, and large particles. Aperture mask A was used for this



experiment based on previous work conducted on fuel sprays using the same DANTEC PDPA system, found in the thesis work of Ryan Batchelor [18]. The prior work confirmed that aperture mask A measured the size of particles produced by the fuel nozzle.

The spherical validation band is used to validate and measure particles that are not perfectly spherical. DANTEC states that the spherical validation band defines the width of the tolerance band of the phase difference between detectors. A spherical validation band value of 25% was used for all test cases. The value of 25% was decided upon due to the high g-loads in the cavity which distorted the droplet shape. The data collection rate was directly related to the spherical validation band. For higher spherical validation values, more droplets were recognized and measured by the detection system. The value of 25% allowed for data to be collected at a sufficient rate.

The center frequency and bandwidth were adjusted according to the velocity range in the flow. The center frequency was the nominal velocity value the PDPA system was looking to record while the bandwidth provided the range of velocities in which the system was looking to analyze data. The values were adjusted according to the air velocity in the cavity in order to collect the maximum amount of data possible.

The signal gain and high voltage level were optimized together to obtain consistency for all measurements. The signal gain sets the gain of the photo-multiplier signal amplifier while the high voltage level sets the high voltage to the photo-multiplier. The signal gain and high voltage level were adjusted until the rate of data collection was maximized. The values resulting in the greatest data collection rate were a signal gain of 26 dB and a high voltage level of 1000.

The BSA Flow software incorporates two separate conditions which indicate the completion of data collection at a given point. The software allows the user to input both a maximum sample size and a maximum amount of time for which the PDPA system collects data at a given point. Sprays are made up of primarily small droplets; however, it is the relatively few large droplets that affect the overall average diameter [11]. A large number of drops needed to be recorded in order for the sample size to be representative of the nozzle spray. According to Lewis et al. [19], in a sample of 1000 drops, the presence or absence of one large drop could affect the average diameter by as much as 100%. Bowen and Davis [20] conducted research on the influence of sample size on the accuracy of drop size measurements and found that in order to obtain a degree of confidence of 95%, 5500 drops should be measured. Table 4 shows the results of the number of drops recorded and the corresponding accuracy of the measurements found by Bowen and Davis.

**Table 4: Influence of sample size on accuracy of drop size measurements [20]**

Number of Drops in Sample	Accuracy (%)
500	$\pm 17$
1500	$\pm 10$
5500	$\pm 5$
35000	$\pm 2$

Initial measurements were conducted to determine how many samples were to be collected such that the mean particle diameter was measured with in  $\pm 1 \mu\text{m}$ . Figure 48 shows a representative plot of the initial measurements. The sampling criterion was found to be met with a maximum sample size of 2000 samples giving an accuracy measurement of 8.5% according to the research by Bowen and Davis [20]. In addition to the maximum amount of samples to be collected, the maximum data collection time was

set to 60 seconds. The value of 60 seconds was selected because if the computer had not collected 2000 drops in 60 seconds it likely would not collect data at a sufficient rate to measure 2000 drops in a timely manner. The software stopped recording data once the maximum sample size or maximum data collection time was reached, whichever occurred first.

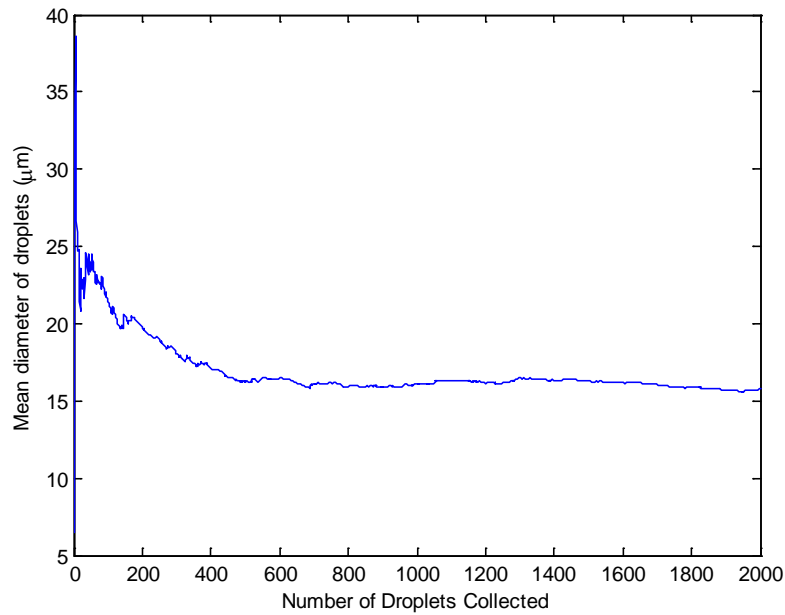


**Figure 48: Mean diameter of droplets as a function of droplets collected**

## **4. Analysis and Results**

The goal of this work is to quantitatively measure how a spray is affected when it is injected into a high g-load environment. The DANTEC [15] PDPA measuring system described in Chapter 3 was used to characterize the droplet size distribution and velocity pattern. For the purposes of this research, a water spray was used to simulate a fuel spray to gain an initial understanding of the spray behavior within the circumferential cavity of a UCC. The primary objective of the research was to characterize the fuel injector spray pattern as a function of g-loading. Understanding fuel spray patterns within the circumferential cavity is needed to determine the appropriate number of fuel nozzles needed to create a continual burning pattern and produce ideal emissions and temperature profiles.

### **4.1 Test Conditions**

Initial measurements were taken with the air flow in the circumferential cavity traveling in the clockwise direction, when viewing the rig from the front. Data was collected for six separate cases previously detailed in Chapter 3.4.1, listed in Table 2. The swirl in the circumferential cavity was varied to induce g-loadings of 300, 1400, and 5000 g. Figure 49 illustrates where various temperature and pressure measurements were recorded in the circumferential cavity with respect to the probe volume. All tests were performed with water spraying from a single nozzle into the cavity of the rig. Water was injected at two different water pressures measured upstream of the nozzle: 0.7 or 1.4 MPa. The approximate mass flow rates of the water were 17 and 24 mL/min. The velocity of the air in the cavity was measured using pressure transducers in the opposite

side of the cavity from the water spray. Average pressure and velocity measurements were recorded periodically throughout the time required to perform PDPA measurements for a single rig operating condition with little variation was seen during that time. The air and water temperatures throughout the rig were approximately 293 K.

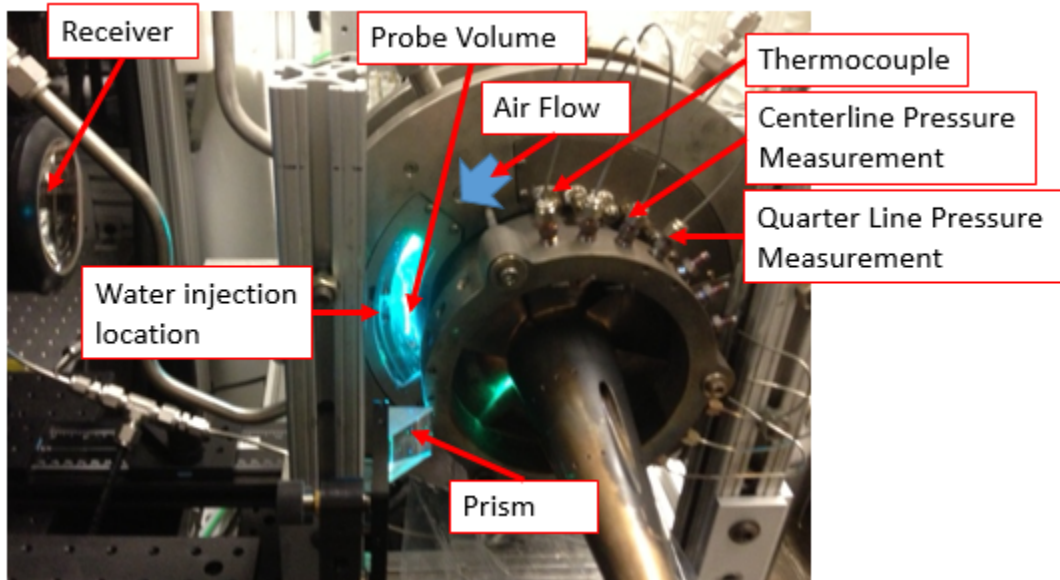


**Figure 49: Temperature and Pressure measurement locations within the cavity**

Data was not able to be collected at the locations 10 mm above the fuel nozzle as the spray was quickly turned downstream and few if any droplets reached the laser probe volume. A representative plot of average velocity and particle droplet size measurements for the operating conditions of 1400 g and 0.7 MPa is shown in Figure 50. The circles in the plot represent the average droplet size. The vector size and color correspond to the average speed of the droplets. Only locations where more than 1200 droplets were measured are shown. Measurements were not performed closer to the nozzle exit due to geometry considerations with the rig hardware and the off-axis nature of the scattered light needed for PDPA.

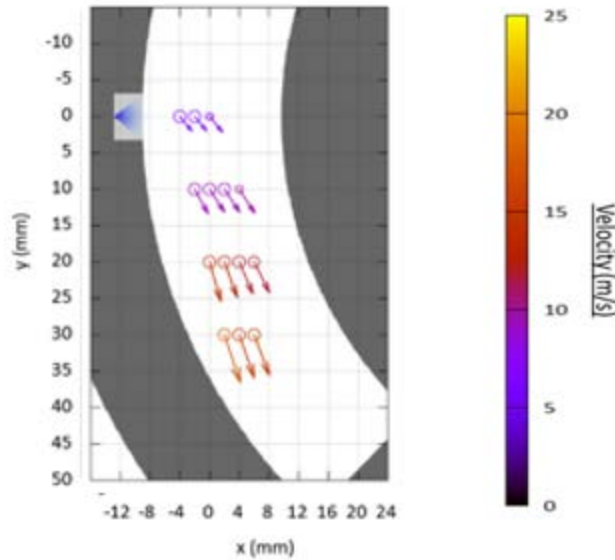


**Figure 50: Initial measurements recorded at 1400 g 0.7 MPa**

The values for droplet size and velocity were calculated by the PDPA processor based upon the light received by the receiver, explained in Chapter 2.5. Figure 50 shows that the average speed of the droplets increases with distance from the nozzle. This is due to the relatively large velocity of the air flow in the cavity. The y component of velocity is pointing downward indicating that the air flowing clockwise (when viewed from front of rig) in the cavity has redirected any initial spray exiting upwards. For some rig operating conditions, the droplet velocity at a spatial height of 10 mm shows a slightly stronger velocity in the positive x direction. This is attributed to the fact that the spray is issuing directly from the nozzle into this region and the initial positive x momentum has not been completely dominated by the air flow in the cavity. The direction of the average droplet velocity is relatively constant across the region where data was recorded.

Initial data from all six of the test cases is given in Figure 51. Once again, only locations where at least 1200 droplets were recorded are presented in the plots. For all

six cases, the same general trend is realized. As the droplets are exposed to the cross flow for a longer period of time, the initial momentum in the x direction diminishes, and the particles are accelerated as they travel further downstream.

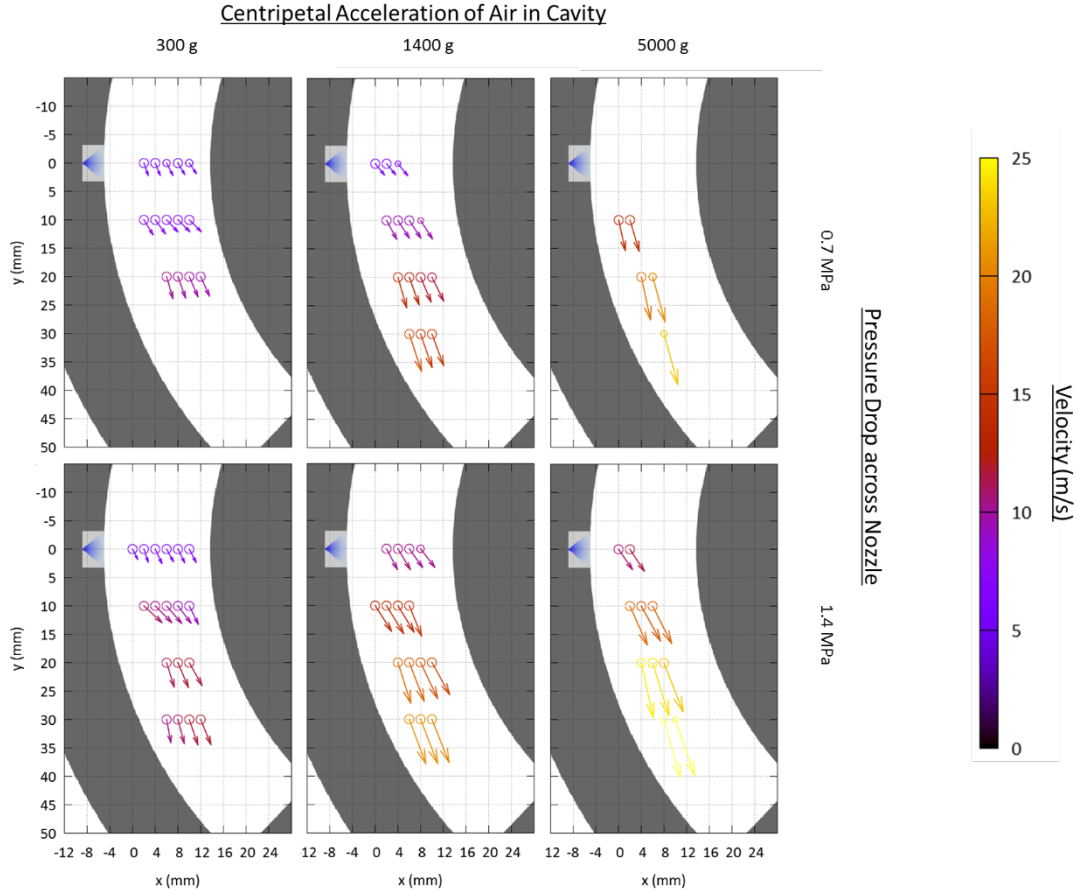


**Figure 51: Measured velocity for water droplets in the UCC cavity with gravitational loadings of 300, 1400 and 5000 g. The pressure drop across the nozzle is 0.7 or 1.4 MPa. The circles in the plots represent the average droplet size.**

## 4.2 Droplet Break-up

For each location in the data location grid provided in Figure 46, the average liquid Reynolds number, Ohnesorge number, and relative air Weber number were calculated using Equation (2.5), Equation (2.6), and Equation (2.2), respectively. The

maximum and minimum Reynolds numbers, Ohnesorge numbers, and relative air Weber numbers are given in Table 5.

**Table 5: Maximum and Minimum liquid Reynolds number, Ohnesorge Number, and Weber number**

Test Case	Liquid Reynolds Number		Ohnesorge Number		$We_{rel-air}$	
	Max	Min	Max	Min	Max	Min
1	2487	351	0.0522	0.0176	0.0390	0.0008
2	1968	306	0.0544	0.0249	0.0191	0.0004
3	5147	946	0.0356	0.0176	0.2459	0.0099
4	7709	1131	0.0382	0.0183	0.0968	0.0110
5	5575	1328	0.0331	0.0180	1.1051	0.1465
6	6253	1222	0.0362	0.0168	0.1604	0.0020

Comparing the values for liquid Reynolds number and Ohnesorge number against Figure 18 given in Chapter 2.4.1, for all cases, the Ohnesorge number is on the order of  $10^{-2}$  while the liquid Reynolds numbers range from an order of  $10^2$  to  $10^3$ . The Ohnesorge number and range of Reynolds numbers indicate that all six test cases experience a mixture of all three modes of atomization: Rayleigh breakup, sinuous wave break-up, and secondary atomization. During Rayleigh break-up, which occurs at Reynolds numbers less than 800 for Ohnesorge numbers on the order of  $10^{-2}$ , large drops of fairly uniform size are created allowing for secondary atomization to occur and further disintegrate the particle [11]. The relative air Weber numbers, also given in Table 5, are used to determine the mode of secondary atomization. Park, Kim, and Lee [21] state that there are three modes of secondary atomization: bag break-up, stretching and thinning break-up, and catastrophic break-up. Bag break-up occurs at Weber numbers less than 100, stretching and thinning break-up occurs at Weber numbers between 100 and 300,



and catastrophic break-up occurs when Weber numbers are greater than 300 [21]. Park et al. found when secondary atomization occurred in the regime of bag break-up, drops of varying size were created. Drops of larger size tended to continue in their initial direction while the smaller diameter droplets were quickly affected by the cross flow [21]. Stretching and thinning break-up along with catastrophic break-up resulted in rapid break-up of drops into small and stable sizes [21]. The greatest relative air Weber number calculated for the six rig operating conditions was 1.1051. Because the relative air Weber number of the spray inside the cavity was less than 100, all test conditions experienced the bag break-up regime of secondary atomization.

### **4.3 Stokes Number Determination**

The primary objective of this research is to characterize the behavior of sprays within the circumferential cavity. As detailed in the previous section, the droplets within the circumferential cavity experienced bag break-up as a mode of secondary atomization where, depending on size, the droplet will either tend to follow or not follow the flow field. The Stokes number can be used to determine how particles are following the air flow inside the cavity. Ideally the droplets need to follow the air flow inside the cavity and remain in the cavity until they are ignited. Keeping the droplets in the cavity until they ignite is critical. If the droplets do not follow the flow in the cavity, they could be injected through the cavity and into the core flow prior to ignition and therefore waste significant amounts of fuel.

The Stokes number is a dimensionless number that details the behavior of particles in a fluid flow and is defined as the ratio of the characteristic time of a particle

to the characteristic time of the flow or obstacle [22]. For Stokes numbers greater than one, particles tend not to follow the flow in which they are suspended. Conversely, for Stokes numbers less than one, particles tend to closely follow the flow in which they are entrained. The Stokes number for a particle in a flow field can be calculated using Equation (4.1).

$$Stk = \frac{\tau U_0}{d_c} \quad (4.1)$$

Where:

$U_0$  = the velocity of the fluid

$d_c$  = the characteristic dimension of the obstacle

$\tau$  = the relaxation time for the particle.

Particle Reynolds numbers for droplets within the circumferential cavity were calculated using Equation (4.2)

$$Re_{particle} = \frac{\rho_{air} U_{rel} D}{\mu_{air}} \quad (4.2)$$

Where:

$\rho_{air}$  = density of air

$U_{rel}$  = relative velocity of the particle ( $V_{air} - V_{liquid}$ )

$\mu_{air}$  = viscosity of air

For analysis purposes, the largest particle Reynolds number was calculated using the values of  $\rho_{air} = 1.2041 \text{ kg/m}^3$  and  $\mu_{air} = 1.8208 \text{ kg/(m s)}$  at 293 K. Assuming a maximum  $U_{rel}$  equal to the velocity of the air in the circumferential cavity when  $V_{liquid} = 0$ , the largest particle Reynolds number was found to be 377 for a droplet measuring 100  $\mu\text{m}$  in diameter. For Reynolds numbers in the range of 0 to 1000 the particle drag coefficient is inversely proportional to the Reynolds number [22]. When the

particle drag coefficient is inversely proportional to the Reynolds number, the value of  $\tau$  in Equation (4.1) can be calculated using Equation (4.3) [22].

$$\tau = \frac{\rho_d d_d^2}{18\mu_g} \quad (4.3)$$

Where:

$\rho_d$  = the particle density  
 $d_d$  = the particle diameter  
 $\mu_g$  = the gas dynamic viscosity

The droplets were separated based on their Stokes number. Three different Stokes number regimes were created, droplets with Stokes numbers less than one, droplets with Stokes numbers greater than two, and droplets with Stokes numbers between 0.5 and 2. Combining Equations (4.1) and (4.3) and selecting a Stokes number, the diameter of a particle which gives the desired Stokes number can be calculated as given by Equation (4.4).

$$d_d = \sqrt{\frac{18\mu_g d_c Stk}{\rho_d U_0}} \quad (4.4)$$

Using the values for the various properties of water and air given in Table 6, Equation (4.4) shows that a droplet diameter of 41, 28, and 20  $\mu\text{m}$  correspond to a Stokes number of one for the g-loads of 300, 1400, and 5000 g's, respectively.

**Table 6: Flow Properties**

Flow Properties	
$U_0$ (300 g's)	14.07 m/s
$U_0$ (1400 g's)	30.4 m/s
$U_0$ (5000 g's)	57.45 m/s
$d_c$ (radius of UCC circumferential cavity)	0.067 m
$\rho_d$ (density of water)	1000 kg/m <sup>3</sup>
$\mu_g$ (dynamic viscosity of air)	$1.8028 \times 10^{-5}$ kg/(m s)
$\mu_g$ (dynamic viscosity of water)	$8.9 \times 10^{-4}$ kg/(m s)

Plots for small droplets with Stokes numbers less than 1 for the conditions of 0.7 MPa and g-loadings of 300, 1400, and 5000 corresponding to droplet diameters less than 41, 28, and 20  $\mu\text{m}$ , respectively, are presented in Figure 52. Only locations where at least 100 points were recorded are shown in the plots. The size of the box represents the number of drops that were measured at the given position while the velocity vectors are color coded according to overall magnitude. It can immediately be seen that as the g-load increases the velocity of the particles increase. Droplets with Stokes numbers less than 1 are considered to follow the flow. The plots indicate that the small droplets do follow the flow as expected. Shortly after exiting the nozzle the small droplets lose their initial momentum in the x direction and are swept into the flow while increasing velocity in the direction of the flow. Additionally it was observed that there was a smaller overall amount of droplets the further inboard the droplets traveled, confirming that the droplets rapidly lost their x direction momentum and began following the flow field.

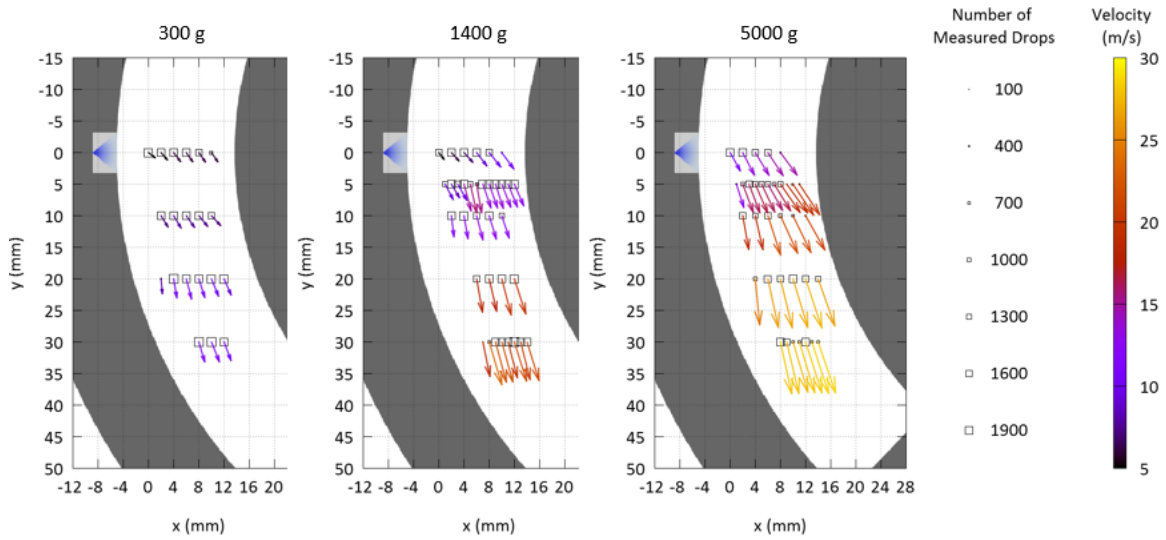


**Figure 52: Vector plots for droplets with Stokes numbers less than 1 for rig operating conditions of 0.7 MPa and g-loadings of 300, 1400, and 5000 g**

Figure 53 shows the vector plots for the same Stokes numbers of less than one with the same corresponding diameters, however the nozzle injection pressure was increased to 1.4 MPa. The overall trend is the same as the 0.7 MPa injection pressure. The droplets are turned into the flow field and increase in velocity the further downstream they travel. Once again it was noticed that there were a smaller overall amount of droplets the further inboard the spray traveled due to the droplets being turned into the flow. Due to the higher injection pressure it was observed that the droplets had a higher initial velocity in the x direction and required more distance before being turned into the flow.

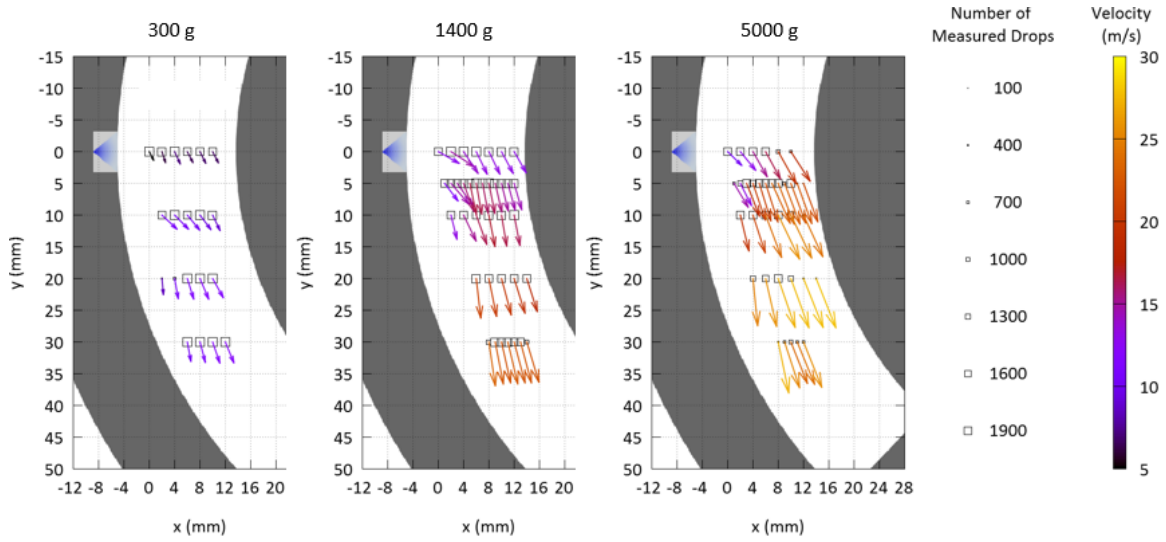


**Figure 53: Vector plots for droplets with Stokes numbers less than 1 for rig operating conditions of 1.4 MPa and g-loadings of 300, 1400, and 5000 g**

The bag break-up regime of secondary atomization produces both large and small droplets where the small droplets tend to follow the flow and the larger droplets tend to continue in their initial direction. Figure 54 plots the larger droplets created by the bag break-up atomization with Stokes numbers greater than 2 for the conditions of 0.7 MPa and g-loadings of 300, 1400, and 5000 corresponding to droplet diameters greater than 58, 39, and 29  $\mu\text{m}$ , respectively. The results showed that at g-loadings of 300 and 1400 g there were very few particles greater than 58 and 39  $\mu\text{m}$  respectively, which indicated that a pressure drop across the nozzle of 0.7 MPa atomized the water droplets to sufficiently low enough diameters to closely follow the flow field within the circumferential cavity. During the 5000 g test case it was noticed that many more droplets with a Stokes number greater than 2 were observed when compared to the 300 and 1400 g test cases. This was due to the fact the diameters of droplets in the 5000 g cross flow (57.45 m/s) only had to be greater than 29  $\mu\text{m}$  in order to achieve Stokes numbers greater than 2. Even though all droplets in Figure 54 have Stokes numbers

greater than 2, they all tended to follow the flow field over the spatial window of the data collection rather than be injected through the cavity and into the core flow. It is important to note that the small size of the window limited the ability to acquire data further than 30 mm downstream from the nozzle. Because of the limited distance, any deviation of the particles from the flow field will take a longer circumferential length than the length data was able to be collected.

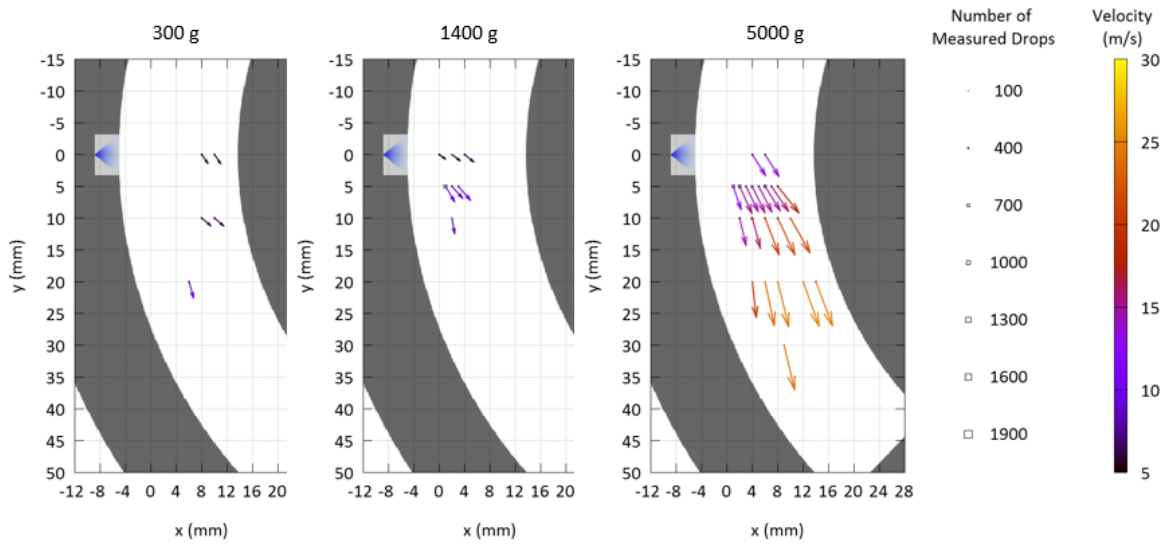


**Figure 54: Vector plots for droplets with Stokes numbers greater than 2 for rig operating conditions of 0.7 MPa and g-loadings of 300, 1400, and 5000 g**

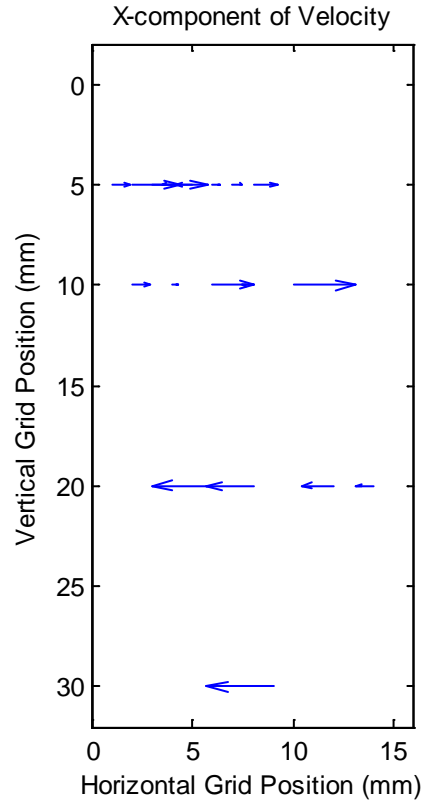
The results showed that the larger diameter droplets had a lower velocity when compared to the smaller diameter droplets at the same conditions. This was due to the fact that the larger droplets weighed more and required more force to accelerate at the same rate as the smaller droplets. Table 7 shows the difference of the x and y components of velocity between particles with Stokes numbers greater than 2 and Stokes numbers less than 1 at rig operating conditions of 5000 g and an injection pressure of 0.7 MPa. The velocities of the smaller particles ( $Stk < 1$ ) were subtracted from the velocities of the larger particles ( $Stk > 2$ ). The results of the velocity difference between

the two particle sizes showed the larger particles were accelerated at a slower rate than the smaller particles in the vertical direction. Additionally, for a given rig operating condition, the difference in the horizontal component of the droplet velocity for particles with Stokes numbers greater than 2 and Stokes numbers less than 1 were plotted on a vector plot. Figure 55 shows the difference in the horizontal component of velocity for the droplets  $[(Stk > 2) - (Stk < 1)]$  when the rig was operated at 5000 g with a nozzle pressure of 0.7 MPa. The direction of the vectors indicate that the larger particles initially have a greater horizontal component of velocity when compared to the smaller particles as evidenced by the vectors pointing toward the right in the measuring planes 5 mm and 10 mm below the fuel nozzle. However, as the particles travel further downstream, the trend reverses and the smaller particles were seen to have a greater horizontal component of velocity than the larger particles as evidenced by the vectors pointing to the left in the measuring planes 20 mm and 30 mm below the fuel nozzle. The relative horizontal component of the larger particles is indicative of the larger particles being pushed outboard by the high g-load as they travel further downstream.



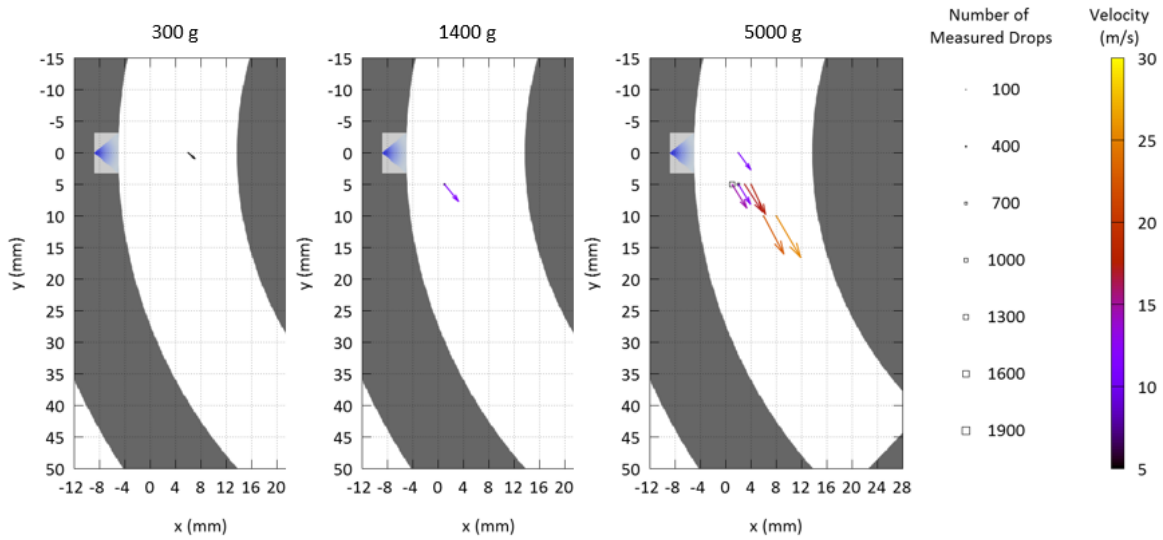
**Table 7: Difference in velocity of particles ( $Stk > 2$ ) – ( $Stk < 1$ ) at 5000 g and 0.7 MPa**

<b>x (mm)</b>	<b>y (mm)</b>	<b><math>\Delta u</math> (m/s)</b>	<b><math>\Delta v</math> (m/s)</b>	<b><math>\Delta</math> Magnitude (m/s)</b>	<b>Magnitude Percent Change</b>
4	0	-0.59	-0.77	-0.96	7.43%
6	0	-0.78	-0.73	-1.04	7.68%
1	5	0.24	-0.37	-0.27	2.19%
2	5	0.63	-0.81	-0.51	3.32%
3	5	0.72	-1.92	-1.48	10.06%
4	5	-0.14	-1.32	-1.26	8.28%
5	5	-0.22	-1.14	-1.12	7.42%
6	5	0.1	-1.16	-0.95	6.34%
7	5	0.13	-0.86	-0.65	4.13%
8	5	0.33	-0.8	-0.45	2.55%
2	10	0.24	-3.5	-3.38	23.11%
4	10	0.08	-1.79	-1.72	10.44%
6	10	0.54	-1.29	-1.04	5.03%
8	10	-0.15	-0.42	-0.44	2.09%
10	10	0.82	-1.19	-0.67	3.21%
6	20	-0.78	-2.46	-2.57	10.88%
8	20	-0.62	-2.2	-2.28	9.42%
12	20	-0.41	-2.54	-2.54	10.27%
14	20	-0.22	-1.63	-1.61	6.53%
9	30	-0.87	-3.66	-3.76	15.68%



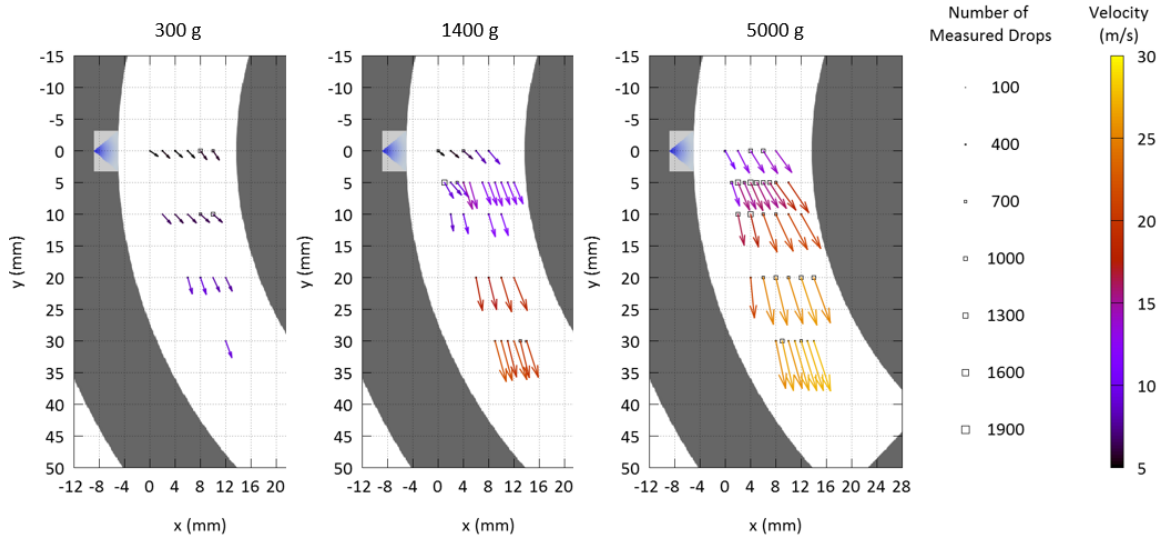
**Figure 55: Vector plot of the difference of the horizontal components of velocity for particles  $[(Stk > 2) - (Stk < 1)]$  at the operation condition of 5000g and injection pressure of 0.7 MPa**

Figure 56 shows the vector plots for the droplets with Stokes numbers greater than 2 with the same corresponding diameters, however the nozzle injection pressure was increased to 1.4 MPa. Due to the increase in nozzle pressure, the droplets were more finely atomized as is evidenced by fewer drops with diameters larger than 58, 39, and 29  $\mu\text{m}$  for 300, 1400 and 5000 g, respectively, when compared to the results presented in Figure 54.



**Figure 56: Vector plots for droplets with Stokes numbers greater than 2 for rig operating conditions of 1.4 MPa and g-loadings of 300, 1400, and 5000 g**

Droplets with Stokes numbers ranging from 0.5 to 2 were plotted for the three different g-loads at 0.7 and 1.4 MPa and are shown in Figure 57 and Figure 58, respectively. These plots represent the middle range of Stokes numbers around the critical Stokes number of 1 which is the value at which a drop or particle will tend to follow or not follow the flow. The results show that droplets with Stokes numbers ranging from 0.5 to 2 follow the same pattern exhibited by the droplets with Stokes numbers less than one and droplets with Stokes numbers greater than two. Once again it was observed that the spray lost its initial momentum in the x direction and was turned to travel with the flow. As shown by the size of the squares and number of positions at which data was recorded for all three Stokes number divisions, the majority of the drops possessed a Stokes number of less than one. Fewer droplets were measured with Stokes numbers between 0.5 and 2 and still fewer droplets were measured with Stokes numbers greater than two. The results of the Stokes number analysis indicated that the nozzle primarily atomized the water into droplets with diameters less than 30  $\mu\text{m}$ .



**Figure 57: Vector plots for droplets with Stokes numbers between 0.5 and 2 for rig operating conditions of 0.7 MPa and g-loadings of 300, 1400, and 5000 g**

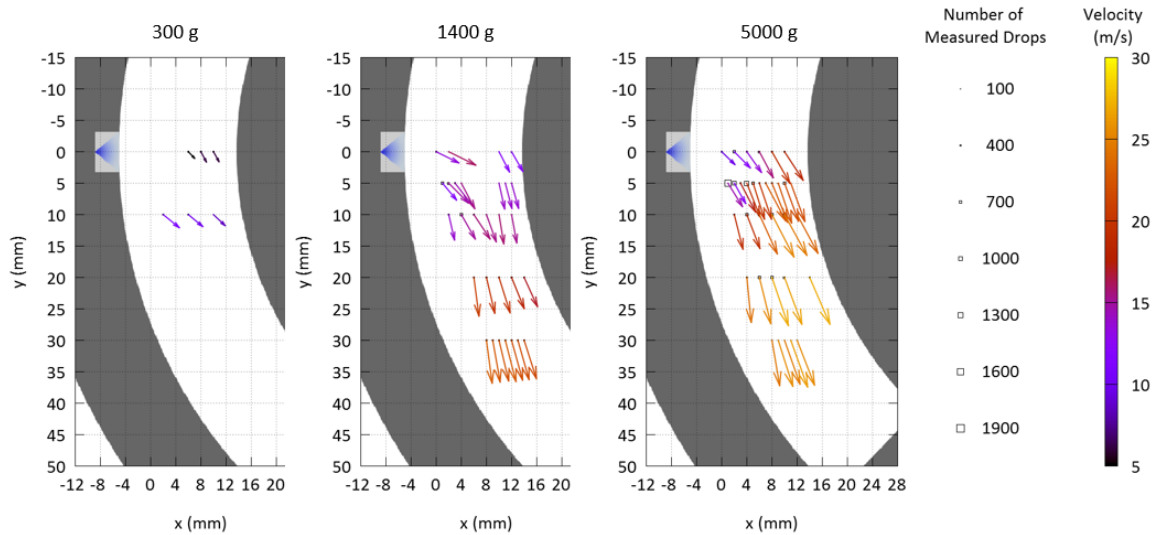


**Figure 58: Vector plots for droplets with Stokes numbers between 0.5 and 2 for rig operating conditions of 1.4 MPa and g-loadings of 300, 1400, and 5000 g**

Figure 59 shows the data for the different range of Stokes numbers evaluated at a single rig operating condition (1400 g, 0.7 MPa). The results clearly indicated that there was a large amount of smaller diameter droplets present within the cavity. It was hypothesized that the higher Stokes number, higher diameter drops present near the nozzle exit decayed as they moved further downstream thus increasing the amount of

smaller Stokes number, smaller diameter droplets present in the measurements 20 and 30 mm downstream from the nozzle. It was noted, however, that the Stokes number did not affect the propensity of the droplet to follow the flow field within the circumferential cavity as all test conditions showed that particles of all sizes tended to turn into and follow the flow.

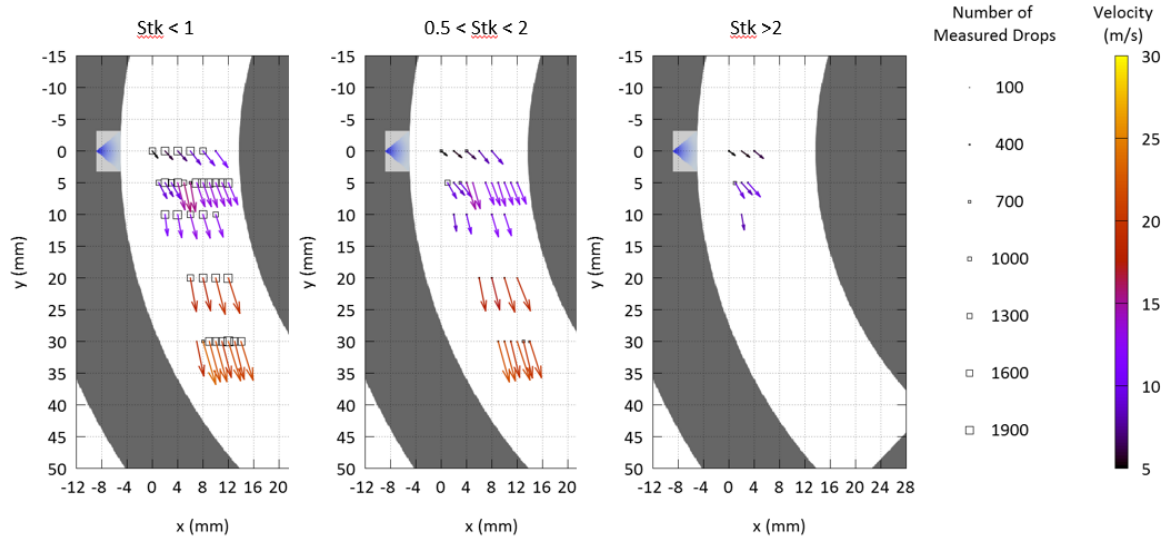


**Figure 59: Vector plots 1400 g 0.7 MPa rig condition for droplet Stokes:  $St < 1$ ,  $0.5 < St < 2$ , and  $St > 2$**

#### 4.4 Concentration Measurements

The next step in characterizing the spray within the circumferential cavity was to determine what the concentration of droplets was at the various grid measurement locations. Finding the concentration of the droplets at the various locations provided insight as to whether the spray was pushed to the OD of the cavity, stayed in the middle of the cavity, or was sprayed through the cavity into the core flow. A droplet concentration measurement was calculated by taking the total number of drops collected at a given grid location and dividing by the time it took to collect the drops, resulting in a

number representing the concentration with the units of drops per second (drops/sec).

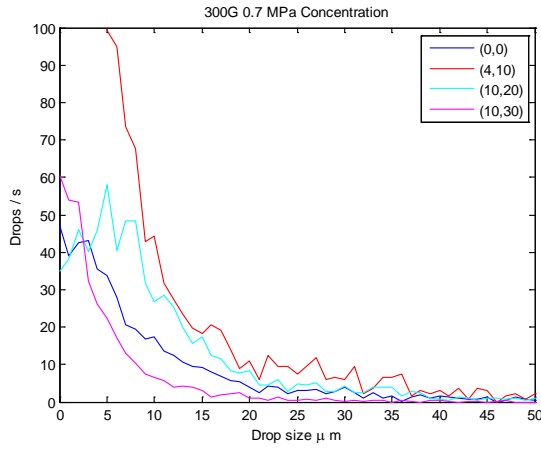
Table 8 indicates the distance, in millimeters from the OD of the cavity, in each horizontal plane where the measurement rate was the greatest for all six test cases. The measurement rate results from all six test cases indicate that the flow behaves in a similar fashion for all centripetal accelerations and nozzle pressures. The highest concentration of drops was observed where the fluid exits the nozzle. After exiting the nozzle, the highest concentration of drops tended to undulate as the spray moves downstream from the nozzle. Overall, the general trend is for the concentration of drops to slowly move from the OD of the cavity towards the center of the cavity; however, the unsteady and recirculating air caused by the air driver jets and interactions with the centerbody cause the undulations seen in the values in Table 8.

**Table 8: Location of highest droplet concentrations for each measurement plane**

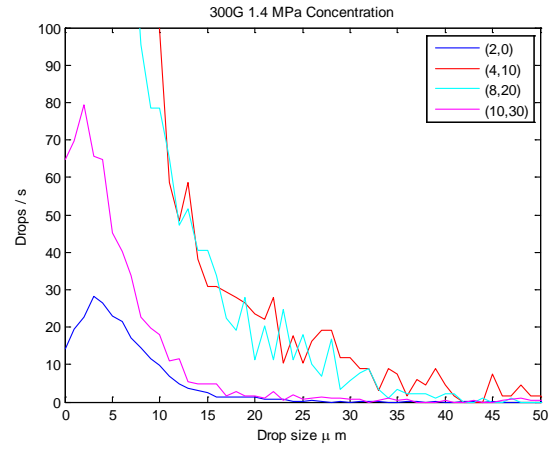
Y position	X position of highest drop concentration from OD (mm)					
	Case 1	Case 2	Case 3	Case 4	Case 5	Case 6
0 mm	0	2	2	0	0	4
5 mm	N/A	N/A	1.84	0.84	4.84	3.84
10 mm	3.37	3.37	3.37	3.37	1.37	3.37
20 mm	7.44	5.44	7.44	5.44	9.44	5.44
30 mm	4.12	4.12	5.12	3.12	3.12	4.12

Analysis was further conducted by taking the locations of highest concentration (drop / sec) values in each horizontal measuring plane and plotting them for a given rig operating condition. Figure 60 shows the plots of the highest droplet concentrations in each plane for the six test conditions. As the particles move further downstream, the data collection rate decreases which indicated that the concentration of particles decreased the further downstream the particles traveled. Additionally, the amount of large sized

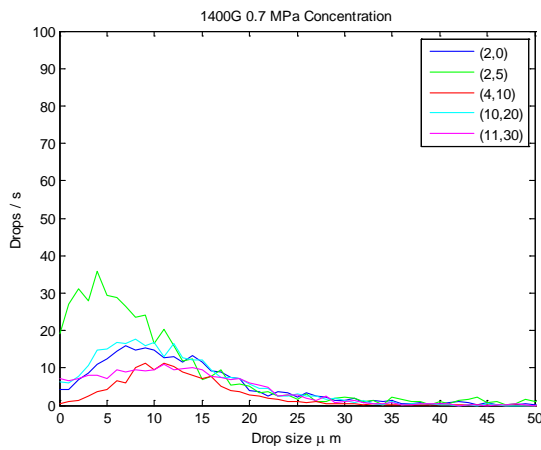
particles,  $d > 20 \mu\text{m}$ , was less at locations further downstream, which indicated droplet decay. A high number of small diameter drops were recorded near the nozzle exit while the amount of smaller drops dissipated further downstream, supporting the theory of droplet decay.



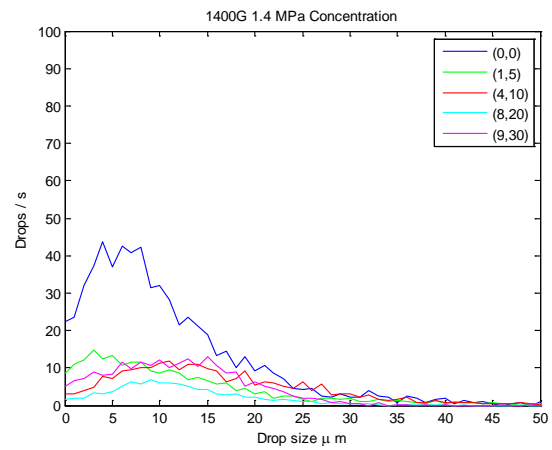
(a) 0.7 MPa 300G



(b) 1.4 MPa 300G



(c) 0.7 MPa 1400G



(d) 1.4 MPa 1400G

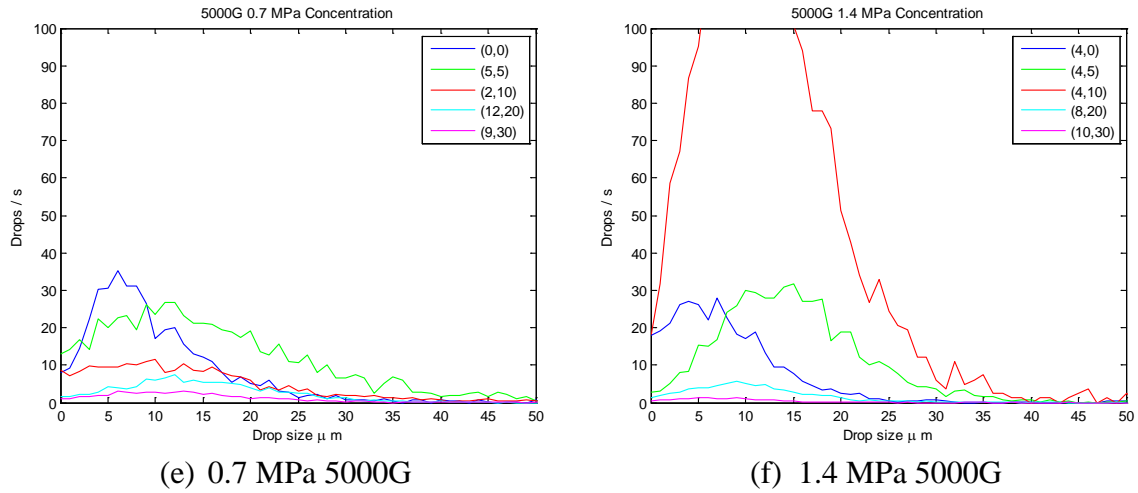


**Figure 60: Plots of the location of the highest concentrations of drops for all six cases. The legend indicates the x and y position in the data collection grid at which the concentration of drops was measured**

#### 4.5 Droplet Velocity and Diameter Analysis

Evaporation affects are an important aspect when conducting measurements of fine sprays. Depending on the initial drop size distribution, evaporation could lead to an increase or decrease in mean particle size [11]. In Chapter 4.3, it was hypothesized that the higher Stokes number, higher diameter drops present near the nozzle exit decayed as they moved further downstream thus increasing the amount of smaller Stokes number, smaller diameter droplets present in the measurements 20 and 30 mm downstream from the nozzle. Analysis was conducted to characterize and quantify the mean diameter of the droplets throughout the test section of the circumferential cavity.

For every droplet recorded, the PDPA system recorded the horizontal and vertical components of velocity along with an associated root mean square (RMS) value to provide information about the turbulence at the given measuring location. Table 9 lists the average vertical and horizontal components of the droplet velocity at the center of the circumferential cavity for each horizontal measuring plane for a g-load of 1400 and



nozzle injection pressure of 0.7 MPa. Tables for the remaining five test conditions can be found in Appendix C. The values show that the vertical velocity of the droplets increased the further downstream they traveled while the horizontal velocity remained constant. The horizontal and vertical velocity RMS values remained similar at each horizontal measuring plane and showed that the turbulence within the cavity remained consistent as the droplets moved further downstream. The average RMS in the horizontal component of the velocity was recorded to be 2.5 m/s while the average RMS in the vertical component of the velocity was recorded to be 3.37 m/s.

**Table 9: Average vertical and horizontal components of droplet velocity at rig operating conditions of 1400g and nozzle injection pressure of 0.7 MPa.**

<b>1400 G 0.7 Mpa</b>					
<b>x (mm)</b>	<b>y (mm)</b>	<b>u (m/s)</b>	<b>v (m/s)</b>	<b>u<sub>rms</sub> (m/s)</b>	<b>v<sub>rms</sub> (m/s)</b>
0	0	2.83	3.25	1.45	2.08
5	5	3.47	15.14	3.74	3.42
6	10	3.32	12.55	1.57	3.41
8	20	3.95	17.03	1.81	3.67
11	30	4.9	18.84	2.41	3.13

Drop diameter analysis was first conducted by comparing the diameters of the drops created when the pressure drop across the nozzle was varied from 0.7 MPa to 1.4 MPa. The results of varying the pressure drop across the nozzle are shown in Figure 61. Representative data was taken from locations 5 mm, 10 mm, and 30 mm downstream from the fuel nozzle and the average droplet diameter was plotted for all three g-loadings and the injection pressures of 0.7 MPa and 1.4 MPa. When the water was injected at the higher pressure of 1.4 MPa, it resulted in a smaller overall droplet diameter, confirming that the higher injection pressures resulted in more finely atomized sprays.

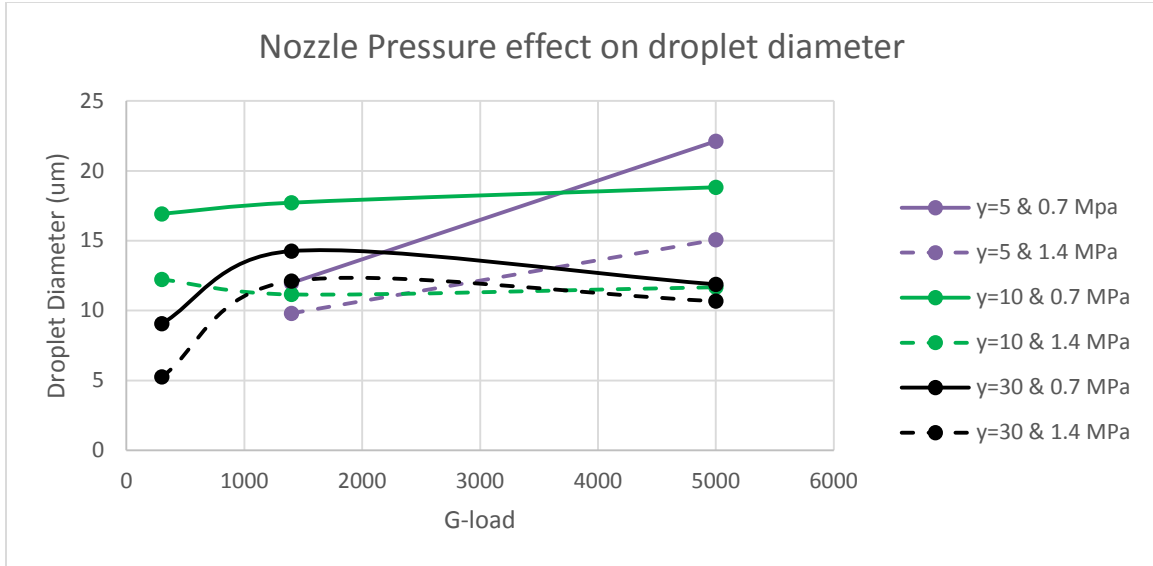


**Figure 61: Nozzle pressure effect on droplet diameter**

The PDPA system collected and stored the diameter of every recorded droplet. In an effort to understand how the droplet diameters differed at the varying measurement locations within the circumferential cavity, the raw droplet diameter data for each measurement location was plotted in the form of a histogram where the diameter of the droplets was on the x-axis and the number of droplets recorded at the various diameters was represented on the y-axis. Figure 62 shows the various histograms generated for the operating conditions of 1400 g and 0.7 MPa. The histogram data provided information proving that the spray within the cavity was relatively uniform throughout the data collection gird, with the majority of the droplets ranging in size from 0 to 25  $\mu\text{m}$ .

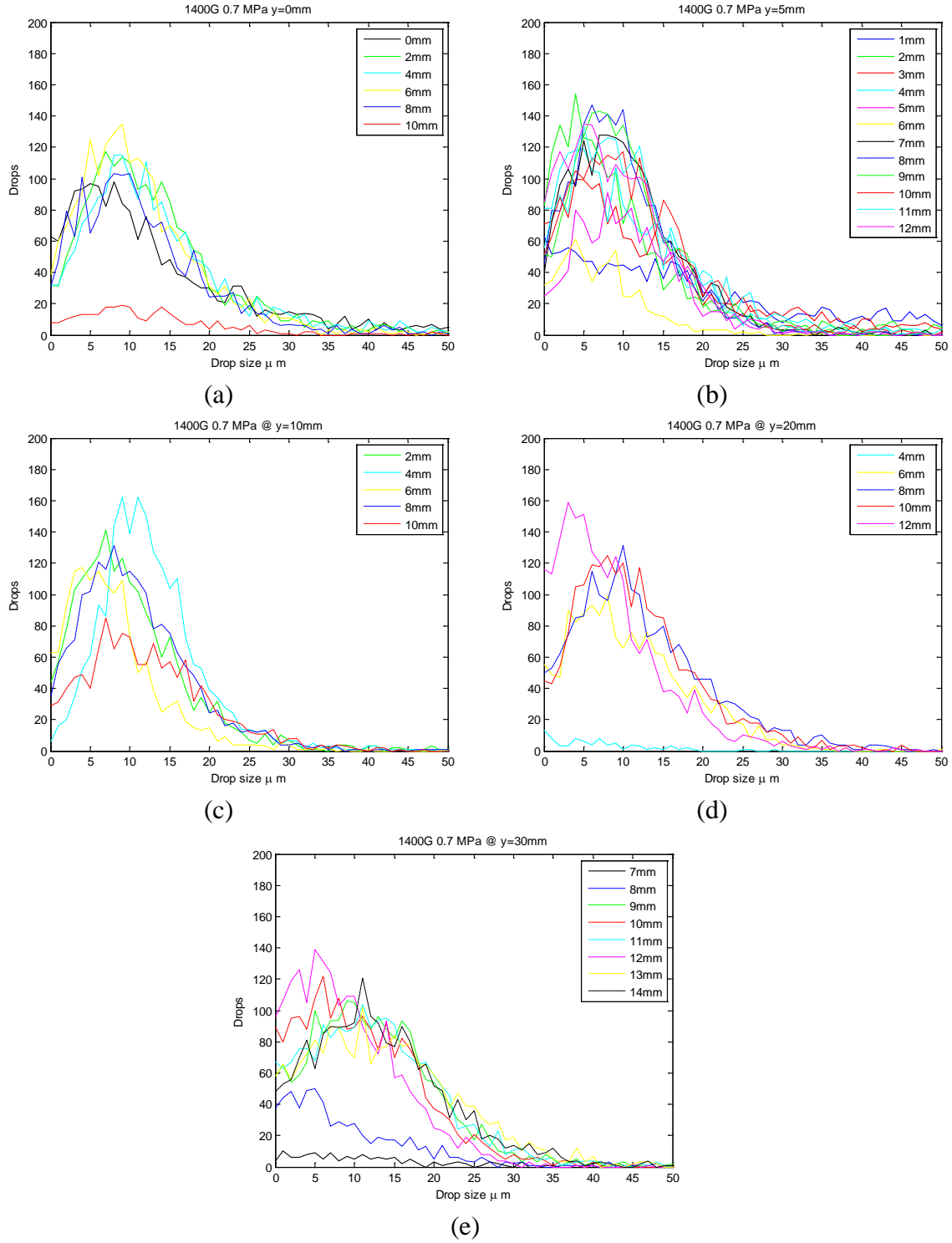


**Figure 62: Histogram of droplet diameters for 1400 g & 0.7 MPa at horizontal locations of (a)  $y=0$ , (b)  $y=5$ , (c)  $y=10$ , (d)  $y=20$ , and (e)  $y=30$**

In an effort to further characterize the spray within the circumferential cavity, the lifetime of the droplets were experimentally calculated for the six rig conditions. To calculate the lifetime of the droplets, the  $D^2$  law for droplet lifetimes was utilized. Turns [23] asserts that for mass transfer controlled evaporation, “the history of the droplet diameter can be obtained by writing a mass balance stating that the rate at which the mass of the droplet decreases is equal to the rate at which the liquid is vaporized [23].” The  $D^2$  law is given by Equation (4.5) and shows that the time derivative of the square of the droplet diameter is constant, meaning that  $D^2$  varies linearly with the slope of  $-K$  which is defined as the evaporation constant [23].

$$\frac{dD^2}{dt} = -\frac{8k_g}{\rho_l c_{pg}} \ln(B_q + 1) \quad (4.5)$$

$$K = \frac{8k_g}{\rho_l c_{pg}} \ln(B_q + 1)$$

Where:

$k_g$  = thermal conductivity of the gas phase of the droplet (W / m-K)

$\rho_l$  = density of the liquid (kg/m<sup>3</sup>)

$c_{pg}$  = Specific heat of gas phase of the droplet (J / kg-K)

$B_q$  = Transfer or Spalding number

Using the values given in Table 10 and found in the text by Turns [23], the theoretical value for  $K$  was determined to be  $5.05 \times 10^{-9}$ . This represents the evaporation into a quiescent flow. For all six test conditions an experimental value for  $K$  in a high g-loaded flow was determined by plotting the weighted average square diameter of droplet size at each horizontal plane versus time it took the particle to reach the given measurement plane. The time it took for the particles to reach each measurement plane was calculated by dividing the distance the particle traveled from the nozzle by the

particles average weighted velocity. For the rig operating condition of 1400 g and 0.7 MPa, the  $D^2$  law plot can be seen in Figure 63. The plots used to determine the  $K$  value for the remaining five operating conditions are listed in Appendix D. Table 11 lists the experimentally calculated  $K$  values with the respective errors for the six rig operating conditions. It is important to note that the theoretical value obtained for  $K$  assumes that droplets are evaporating from a liquid spray into quiescent air, while the experimentally obtained values of  $K$  were obtained in the high g-loaded environment of the UCC. The experimental values for  $K$  calculated inside the circumferential cavity are on the order of 10 to 200 times greater than the theoretical value of  $K$  for water sprayed into still air. The increase in evaporation rate was attributed to the high velocity air flow in the cavity.

**Table 10: Values used to calculate evaporation constant**

Variable	Value
$k_g$ (W / m-K)	0.02
$\rho_l$ (kg / m <sup>3</sup> )	1000
$c_{pg}$ (kJ / kmol-K)	33.448
$B_q$ (dimensionless)	-0.057

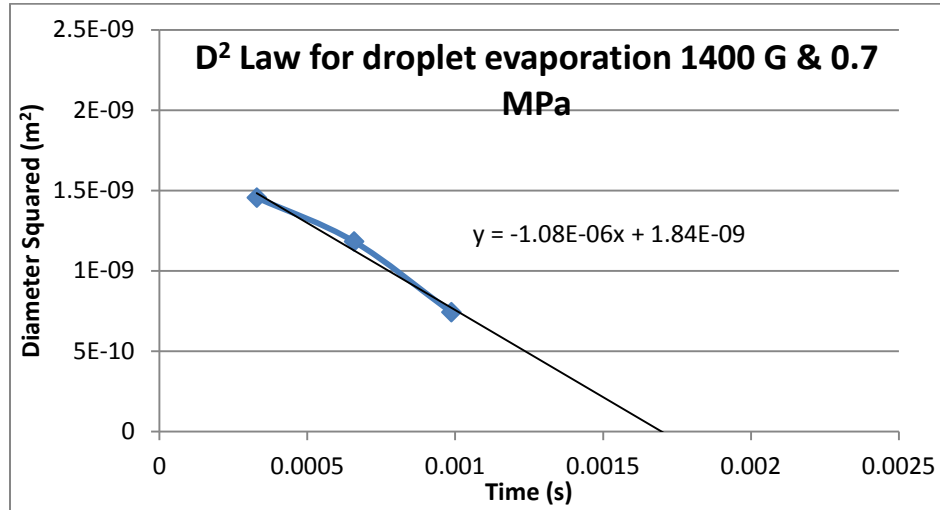


**Figure 63: Plot of  $D^2$  law for a rig operating condition of 1400 g and 0.7 MPa**

**Table 11: Experimentally calculated  $K$  values and associated error**

G-load	$K$ ( $\text{m}^2/\text{s}$ )			
	P = 0.7 MPa	Uncertainty	P = 1.4 MPa	Uncertainty
<b>300</b>	1.43E-07	$\pm 4.65\text{E-}08$	8.57E-08	$\pm 4.58\text{E-}08$
<b>1400</b>	1.08E-06	$\pm 1.46\text{E-}07$	3.56E-07	$\pm 7.17\text{E-}08$
<b>5000</b>	7.68E-07	$\pm 1.37\text{E-}07$	2.08E-07	$\pm 1.12\text{E-}07$

Figure 64 graphically shows how  $K$  varied with g-load. As the g-load increased, the evaporation constant for the water injected into the circumferential cavity increased and leveled off. Figure 64 indicates that there was a substantial increase in the evaporation rate with the addition of shear due to a high cross stream flow. For this data, a further increase in the g-load resulted in a consistent rate within the bounds of the experimental uncertainty. Due in part to determining the evaporation rate from as few as four axial locations coupled with the fact that individual droplets were not tracked, large errors in  $K$  were measured. The error associated with the  $K$  values listed in Table 11 ranges from 27% to 107%. These high uncertainties were compounded by the complications that the smallest particles measured at a given plane were evaporated at the next plane and as such the particle sizes were skewed to larger values than was appropriate.

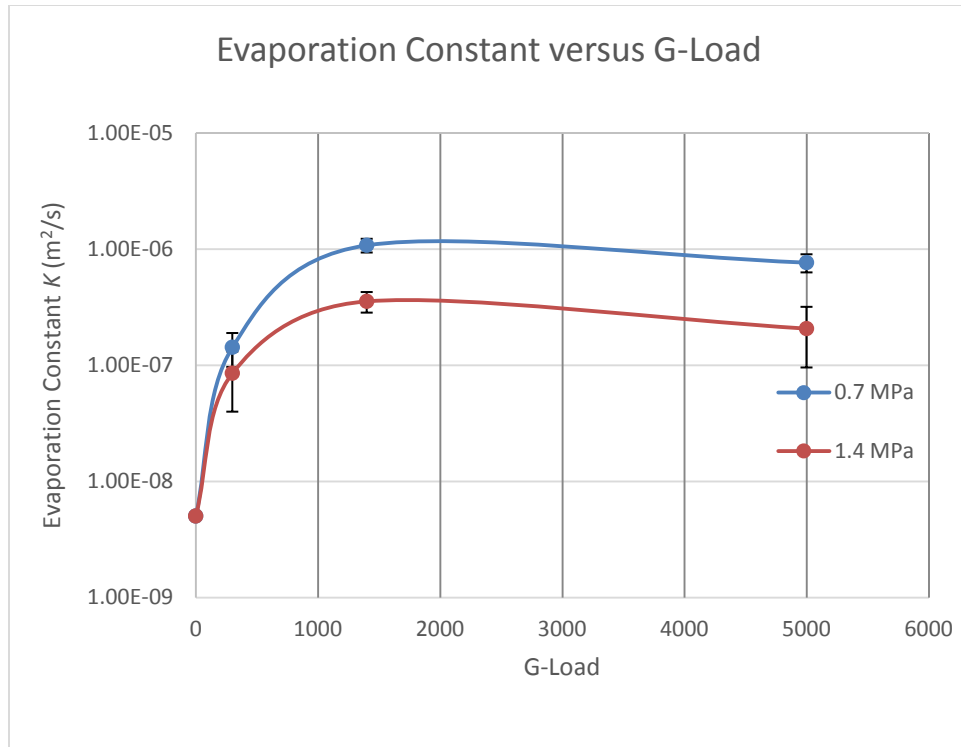


**Figure 64: Evaporation constant versus g-load**

Utilizing the values in Table 11 and the equations of the linear curve fit lines for the  $D^2$  law plots, the estimated particle life time was calculated. The analysis showed the droplets produced by the nozzle would remain in the cavity for a time period ranging from 0.0007 to 0.0026 seconds. The experimentally calculated time for complete evaporation of the droplets for all six test conditions is given in Table 12. In addition to the time it took the droplet to evaporate, the distance traveled by the droplet before complete evaporation was calculated and ranged from 31 to 58 mm. The experimentally calculated distance traveled by the droplets before complete evaporation for all six test cases is also given in Table 12. The length traveled by the droplets prior to complete evaporation is integral to determining the proper fuel injector design pattern. Having a correct fuel injector design pattern results in efficient combustion within the UCC.

**Table 12: Time in seconds and Distance in mm for complete evaporation of the droplets**

	TIME (s)		DISTANCE (mm)	
G-load	Pressure		Pressure	
	0.7 MPa	1.4 MPa	0.7 MPa	1.4 MPa
<b>300</b>	0.0026	0.0022	36.2	31.4
<b>1400</b>	0.0017	0.0013	51.6	39.6
<b>5000</b>	0.0007	0.0010	38.8	58.5



## **V. Conclusions and Recommendations**

### **5.1 Overview**

Tests were conducted using the full annular test rig designed by Wilson [3]. The objective of the tests was to characterize the liquid spray into the circumferential cavity of the UCC. Up to this point, little research has been conducted on the effects of g-loading on liquid sprays. The efforts of this thesis expanded upon the previous qualitative research on sprays inside the UCC conducted by Conrad [14] using high speed imaging. In order to obtain quantitative measurements for the liquid spray, a Phase Doppler Particle Anemometer was utilized, allowing for droplet diameters and velocities to be measured.

### **5.2 Test Conclusions**

The main objective of the testing was to model how a liquid spray was distributed in the circumferential cavity under a g-load. Modeling how the liquid is distributed will provide valuable information regarding the UCC combustion process. The information gathered focused on tracking the droplets of a spray through the circumferential cavity of the UCC and determining the droplet size, velocity, concentration, and lifetime to optimize the overall design of the UCC

#### **5.2.1 Droplet Break-up**

Based on the Reynolds numbers and Ohnesorge numbers of the liquid spray caused by varying the g-load from 300 to 5000 g and the nozzle injection pressure from 0.7 to 1.4 MPa, it was determined that for all six test cases the fluid experienced a mixture of all three modes of atomization: Rayleigh breakup, sinuous wave break-up, and

secondary atomization. The relative air Weber number was then calculated to determine the mode of secondary atomization present within the circumferential cavity. The greatest relative air Weber number calculated for the six rig operating conditions was 1.1051. Because the relative air Weber number of the spray inside the cavity was less than 100, all test conditions experienced the bag break-up regime of secondary atomization. In the bag break-up regime of secondary atomization both large and small particles are created where the large particle tend to continue their motion in their original direction while the smaller particles quickly turn with and follow the flow.

### **5.2.2 Stokes Number Determination**

The Stokes number for the droplets collected by the PDPA system were calculated to give a better understanding of how the different sized particles reacted in the flow. In general, particles with Stokes numbers greater than one tend to not follow the flow while particles with Stokes numbers less than one tend to follow the flow. The particles were divided into three categories: Stokes numbers less than one, Stokes numbers from 0.5 to 2, and Stokes numbers greater than 2. The velocities of the particles for each case were plotted and analyzed. The results indicated that a majority of the particles were small with a Stokes number of less than 2. Droplets in all three cases tended to exhibit similar behavior by quickly turning into and following the flow after being injected into the cavity within the circumferential length of these measurements.

### **5.2.3 Concentration Measurements**

The concentration of droplets at the various measurement conditions was determined to indicate whether the droplets in the spray were forced to the OD of the cavity, remained in the center of the cavity, or traveled completely through the cavity.

The concentration results indicated the unsteadiness that was present within the cavity. The location of highest concentration tended to undulate back and forth with a general trend of migrating toward the center of the cavity with respect to the OD. The undulations of concentration were attributed to the complex air flow within the cavity due to the interaction of the air driver jets, the core flow, and the centerbody vanes. As the g-load increased the drops stayed more toward the OD of the cavity. Plots of the highest concentration locations within each horizontal measuring plane were plotted. The results of the plots indicated that the amount of droplets was significantly decaying the further the droplets traveled.

#### **5.2.4 Droplet Diameter Analysis**

Based on the results found when researching the droplet concentration, analysis was conducted to characterize the diameter of droplets within the spray and how the droplet diameter changed over time. Initial analysis confirmed that when the liquid was injected at a higher pressure, the droplets were more finely atomized with smaller diameters for all of the g-loads tested. Further analysis utilized the  $D^2$  law to determine the evaporation constant ( $K$ ) and the decay rate of the droplets. The g-load inside the circumferential cavity was the primary factor affecting droplet decay rates. It was found that the evaporation constant for the water spray subjected to g-loadings was on the order of 100 times greater than the theoretical evaporation constant corresponding to still air. As the g-load increased, the evaporation constant increased as well. The increased evaporation constant caused the droplets to quickly evaporate within 30 to 60 mm from the nozzle exit.

### 5.3 Recommendations for Future Work

The work conducted for this thesis was the initial spray characterization for fluids inside the circumferential cavity of the UCC. The initial characterization was conducted using water rather than fuel. Laboratory upgrades need to be implemented in order to run fuel through the rig and either collect or burn the fuel downstream from the measurement location. The UCC also needs to be fitted with seals to prevent excessive leaking around all the surfaces especially the optical windows and instrumentation panels. Future work needs to be conducted with fuel to ensure similar behavior to that of water.

Additional research needs to be conducted on reacting flows using diagnostics to investigate where the reaction fronts are occurring and how centripetal acceleration in the circumferential cavity affects the propagating flame structures. Diagnostic tools such as an Image Fourier Transform Spectrometer can analyze where CO and NO<sub>x</sub> are produced and how these emission species move through the combustor. The concentration of OH needs to be analyzed to provide information as to where the flame front is occurring. Identifying the production mechanisms and locations of the various combustion products will be an integral step for developing subsequent emissions reduction techniques.

Additionally, analyzing the flow migration of the combustion products out of the circumferential cavity and the interaction of the combustion products with the core flow will greatly aid in optimizing the UCC. It is recommended that testing be conducted to quantify the effects that the hybrid vanes have on the g-loads within the circumferential cavity and the migration paths of the combustion products out of the cavity. The design of the hybrid vane at the intersection of the circumferential cavity plays a major role in establishing the movement of flow from the cavity into the core flow.

## Appendix A

The 32-port ESP-HD PSID pressure scanner and Esterline DTC Initium pressure acquisition system used to record static and total pressure measurements throughout the rig was calibrated using by using a hand held pressure calibrator. The ESP-HD PSID pressure scanner measured pressures in differential pounds per square inch (PSID) when referenced to the atmospheric pressure. The pressure scanner was capable of recording values up to 5 PSID. The pressure calibrator was attached to the pressure scanner and pressure measurements were input into the scanner in 0.5 PSI increments from 0 up to 4.5. The results, seen in Figure 65, indicated that the values LabView was recording were accurate and no adjustments were necessary.

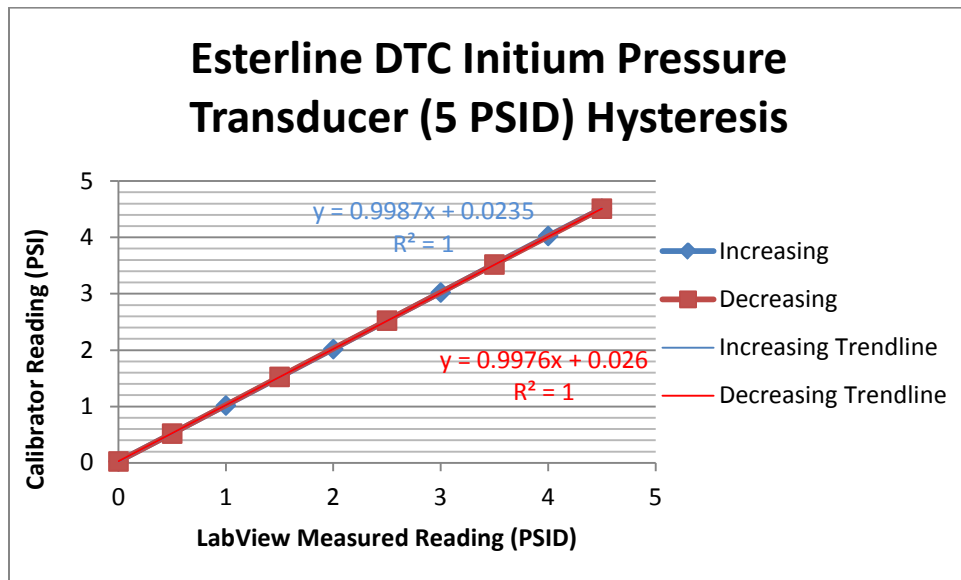


**Figure 65: Pressure Calibration**

## Appendix B

Preliminary measurements were performed using the fuel nozzles that were used in the experimental arrangement. For the fuel nozzle characterization measurements, water was sprayed from the fuel nozzle into quiescent laboratory air. Figure 66 shows an image of the nozzle and four laser beams used for the PDPA measurements. In this figure, the lasers are propagating in the positive x direction and the flow is spraying in the positive z direction. Measurements were performed along a line in the y direction located 25 mm beneath the center of the nozzle. For these preliminary measurements, the pressure drop across the nozzle was 0.55 MPa.

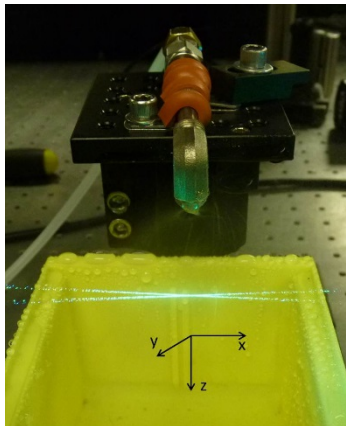


**Figure 66: PDA measurements performed on the same nozzle to be used in the UCC**

Figure 67 shows the average measured z and y velocities as a function of y position as well as the average measured particle diameter. The y components of velocity are always positive due to the exhaust system used while the measurements were performed. The z component of velocity shows the negative axial velocities in the recirculation zone along the centerline of the atomizer. The average droplet size is relatively uniform.

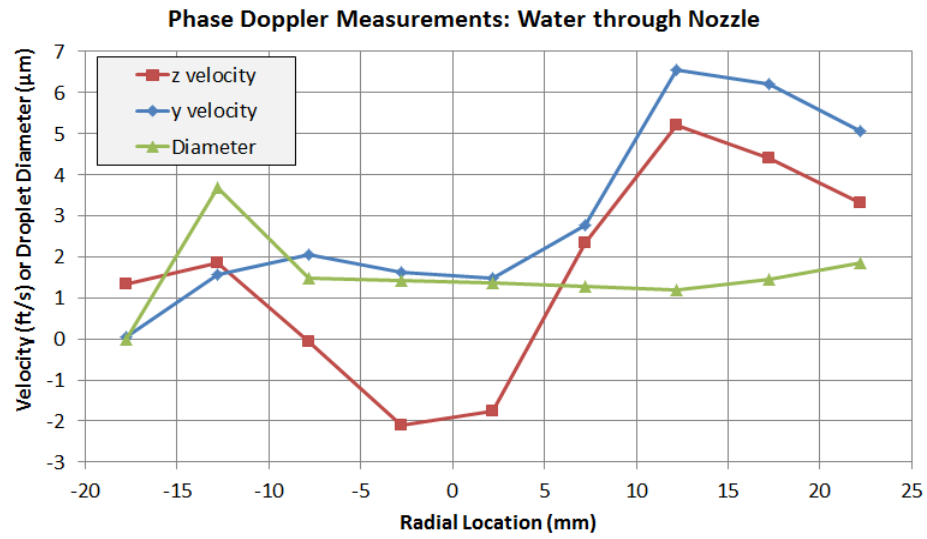


**Figure 67: Preliminary PDPA fuel nozzle characterization measurements for water flowing through the fuel nozzle**

## Appendix C

Appendix C contains tables of the average horizontal and vertical component of velocity measured in the center of the circumferential cavity for each horizontal measuring plane.

**Table 13: Average vertical and horizontal components of droplet velocity at rig operating conditions of 300g and nozzle injection pressure of 0.7 MPa.**

300 G 0.7 Mpa					
x (mm)	y (mm)	u (m/s)	v (m/s)	u <sub>rms</sub> (m/s)	v <sub>rms</sub> (m/s)
0	0	3.49	2.73	1.83	2.90
6	10	4.34	5.98	2.00	2.48
8	20	3.08	9.68	1.01	1.81
11	30	3.61	9.60	0.86	1.56

**Table 14: Average vertical and horizontal components of droplet velocity at rig operating conditions of 300g and nozzle injection pressure of 1.4 MPa.**

300 G 1.4 Mpa					
x (mm)	y (mm)	u (m/s)	v (m/s)	u <sub>rms</sub> (m/s)	v <sub>rms</sub> (m/s)
0	0	2.23	4.43	1.75	2.69
6	10	6.58	7.62	3.68	2.23
8	20	4.55	10.77	1.60	1.50
11	30	3.75	10.99	1.03	1.39

**Table 15: Average vertical and horizontal components of droplet velocity at rig operating conditions of 1400g and nozzle injection pressure of 1.4 MPa.**

1400 G 1.4 Mpa					
x (mm)	y (mm)	u (m/s)	v (m/s)	u <sub>rms</sub> (m/s)	v <sub>rms</sub> (m/s)
0	0	11.02	6.11	4.94	3.45
5	5	3.39	16.11	3.98	3.51
6	10	5.71	15.16	4.67	4.2
8	20	4.03	19.73	2.43	3.21
11	30	5.25	21.89	2.16	2.96



**Table 16: Average vertical and horizontal components of droplet velocity at rig operating conditions of 5000g and nozzle injection pressure of 0.7 MPa.**

5000 G 0.7 Mpa					
x (mm)	y (mm)	u (m/s)	v (m/s)	u <sub>rms</sub> (m/s)	v <sub>rms</sub> (m/s)
0	0	5.29	9.57	3.24	4.55
5	5	6.94	14.27	2.56	2.97
6	10	9.63	18.94	2.14	3.81
8	20	6.21	25.45	2.03	4.02
11	30	7.99	26.4	1.64	4.47

**Table 17: Average vertical and horizontal components of droplet velocity at rig operating conditions of 5000g and nozzle injection pressure of 1.4 MPa.**

5000 G 1.4 Mpa					
x (mm)	y (mm)	u (m/s)	v (m/s)	u <sub>rms</sub> (m/s)	v <sub>rms</sub> (m/s)
0	0	7.29	7.12	3.94	3.87
5	5	6.14	19.42	4.1	4.15
6	10	8.6	21.88	3.7	4.11
8	20	8.89	25.54	1.94	4.42
11	30	9.12	22.31	1.7	8.25

## Appendix D

The following graphs represent the  $D^2$  law data analysis using the experimental results to calculate the evaporation constant ( $K$ ) of the water droplet spray inside the circumferential cavity of the UCC.

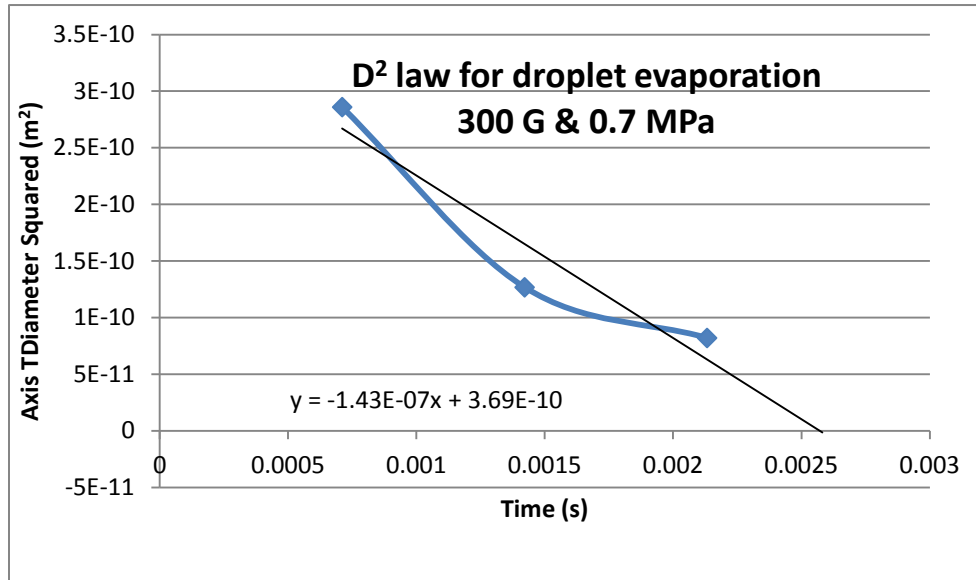


Figure 68: Plot of  $D^2$  law for a rig operating condition of 300 g and 0.7 MPa

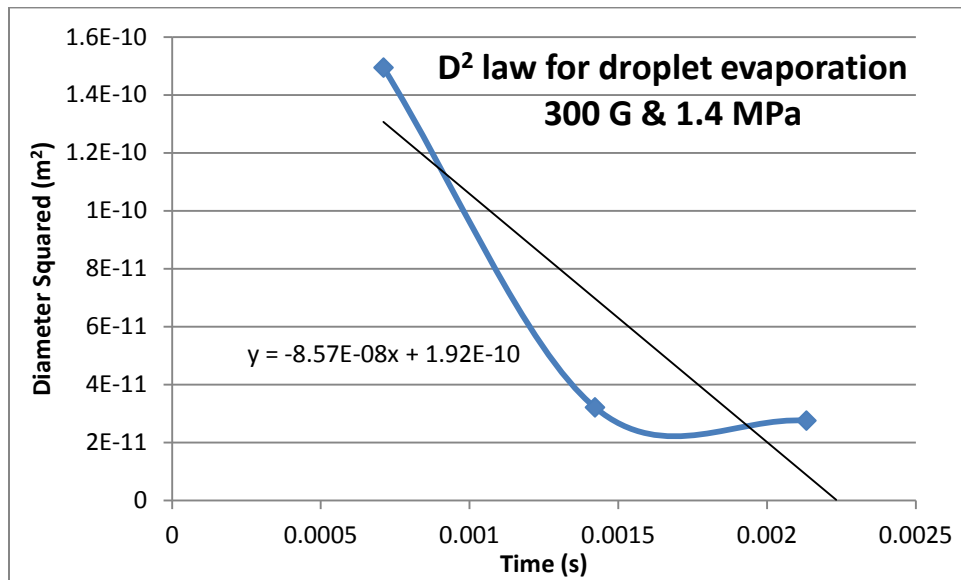
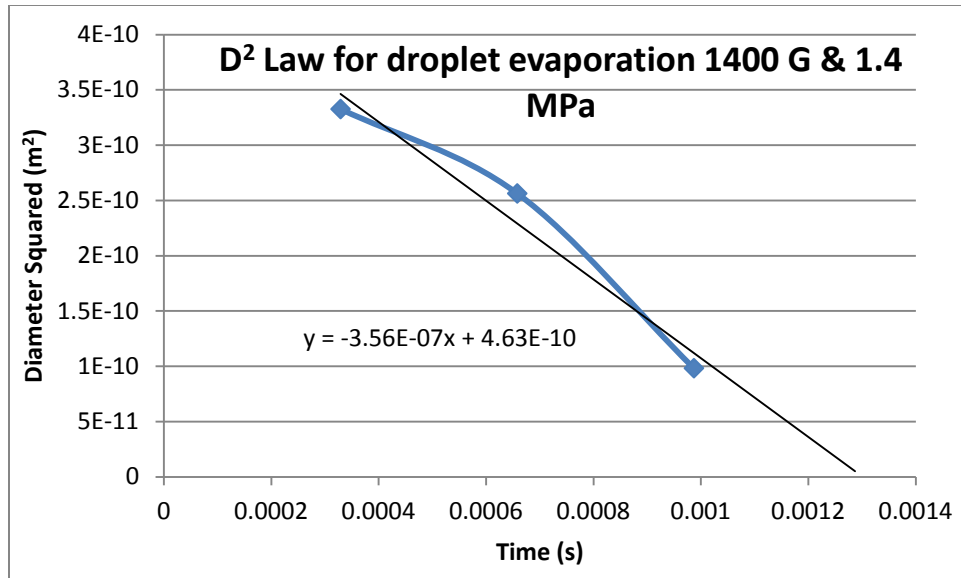
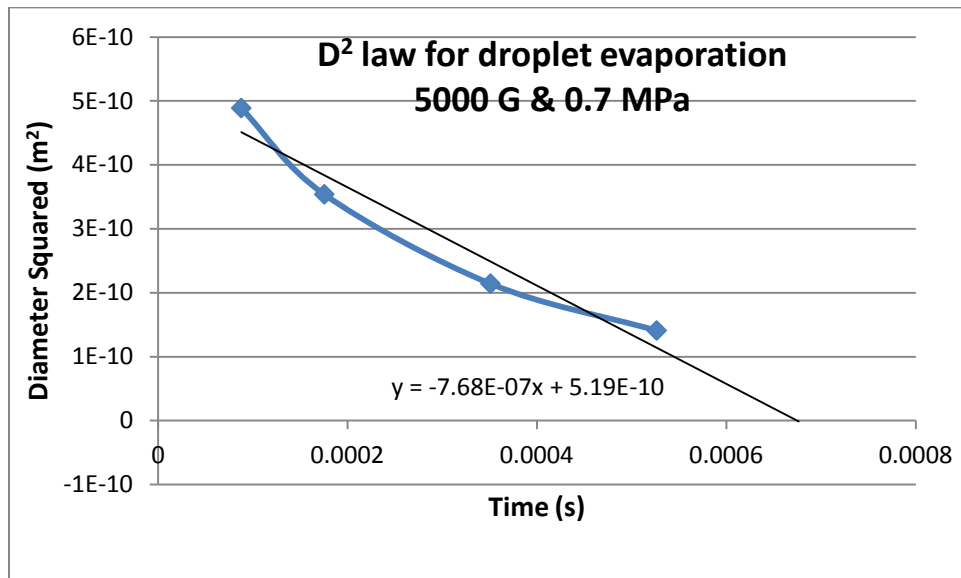


Figure 69: Plot of  $D^2$  law for a rig operating condition of 300 g and 1.4 MPa



**Figure 70: Plot of D<sup>2</sup> law for a rig operating condition of 1400 g and 1.4 MPa**



**Figure 71: Plot of D<sup>2</sup> law for a rig operating condition of 5000 g and 0.7 MPa**

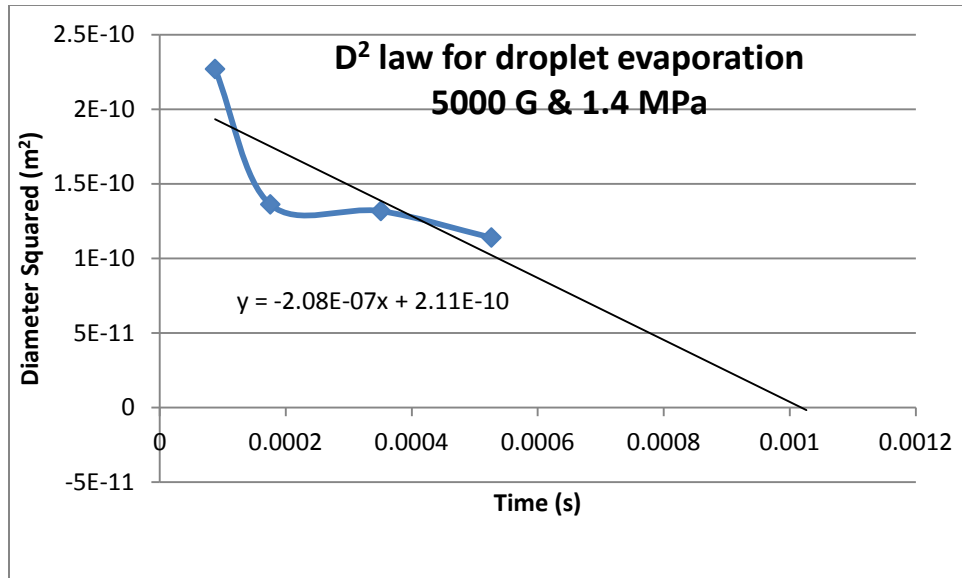


**Figure 72: Plot of D<sup>2</sup> law for a rig operating condition of 5000 g and 1.4 MPa**

## Bibliography

1. Mattingly, J. D., Heiser, W. H., Pratt, D. T., *Aircraft Engine Design*, 2<sup>nd</sup> edition, AIAA, Reston, Virginia, 2002.
2. Lewis, G. D., "Swirling Flow Combustors – Fundamentals and Applications," Presented at AIAA/SAE 9th Propulsion Conference, Las Vegas, Nevada, AIAA-1973-1250, 1973.
3. Zelina, J., Sturgess, G. J., and Shouse, D. T., "The Behavior of an Ultra-Compact Combustor (UCC) Based on Centrifugally Enhanced Turbulent Burning Rates," 40th AIAA/ASME/SAE/ASEE Joint Propulsion Conference, AIAA-2004-3541, 2004.
4. Bohan, B.T. and Polanka, M. D., "Analysis of Flow Migration in an Ultra-Compact Combustor," *Journal of Engineering for Gas Turbines and Power*, vol. 135, 051502 1-11, 2013.
5. Wilson, J. D., "Characterizing G-loading, Swirl Direction, and Rayleigh Losses in an Ultra Compact Combustor," Graduate School of Engineering and Management, Air Force Institute of Technology (AU), WPAFB, Ohio, Master's thesis, 2013.
6. Sirignano, W. A., Delplanque, J. P., Liu, F., "Selected Challenges in Jet and Rocket Engine Combustion Research," 33rd AIAA/ASME/SAE/ASEE Joint Propulsion Conference, Seattle, Washington, AIAA-1997-2701, 1997.
7. Yonezawa, Y., Toh, H., Goto, S., Obata, M., "Development of the Jet-Swirl, High Loading Combustor," 26th AIAA/ASME/SAE/ASEE Joint Propulsion Conference, Orlando, FL, AIAA-1990-2451, 1990.
8. Anthenien, R. A., Mantz, R. A., Roquemore, W. M., and Sturgess, G. J., "Experimental Results for a Novel, High Swirl, Ultra Compact Combustor for Gas Turbine Engines," 2nd Joint Meeting of the U.S. Sections of the Combustion Institute, Oakland, CA. 2001.
9. Zelina, J., Sturgess, G., Hancock, R., "Ultra-Compact Combustors for Advanced Gas Turbine Engines," 49<sup>th</sup> ASME International Gas Turbine and Aeroengine Congress and Exposition, Vienna, Austria, GT2004-53155, 2004.
10. Anderson, W., Radtke, J., King, P., Thornburg, H., Zelina, J., Sekar, B., "Effects of Main Swirl Direction on High-g Combustion," 44th AIAA/ASME/SAE/ASEE Joint Propulsion Conference and Exhibit, Hartford, Connecticut, AIAA-2008-4954, 2008.

11. Lefebvre, A. H., *Atomization and Sprays*. New York: Hemisphere Publishing, 1989.
12. Ohnesorge, W. V., "Formation of drops by nozzles and the breakup of liquid jets." *Z. Angew. Math. Mech.* Vol. 16 No. 4, pp. 355-358, 1936.
13. Fraser, R. P. and Eisenklam, P., "Research into the performance of atomizers for liquids." *Imp. Coll. Chem. Eng. Soc. J.*, Vol. 7. pp. 52-68, 1953.
14. Conrad, M. M., "Integration of an Inter-Turbine Burner to a Jet Turbine Engine," Graduate School of Engineering and Management, Air Force Institute of Technology (AU), WPAFB, Ohio, Master's thesis, 2013.
15. *BSA Flow Software Version 4.10 Installation & User's Guide*. Skovlunde, Denmark: Dantec Dynamics, 2006.
16. TELEDYNE ISCO, *D-Series Pumps Installation and Operation Guide*, Lincoln, NE, 2012
17. National Instruments LabVIEW graphical programming code. National Instruments 2012.
18. Lynch, A., Batchelor, R. G., Kiel, B., Miller, J., Gord, J., and Reeder, M., "Spray Characteristics of a Pressure-Swirl Fuel Injector Subjected to a Crossflow and a Coflow." *Atomization and Sprays*, Vol. 21, No. 8, 2011.
19. Lewis, H., Edwards, D. G., Goglia, M. J., Rice, R. I., & Smith, L. W., "Atomization of liquids in high velocity gas streams." *Industrial & Engineering Chemistry*, Vol. 40, No. 1, pp. 67-74. 1948.
20. Bowen, I. G., and Davies, G. P., Report ITC 28, Shell Research Ltd., London, 1951
21. Park, S. W., Kim, S., Lee, C. S., "Breakup and atomization characteristics of mono-dispersed diesel droplets in a cross-flow air stream," *International Journal of Multiphase Flow*, Vol. 32. pp 807-822. 2006
22. Brennen, C. E., *Fundamentals of multiphase flow*. Cambridge University Press, 2005.
23. Turns, S. R., *An Introduction to Combustion*, 3rd edition, McGraw-Hill, Inc., New York, 2012.

REPORT DOCUMENTATION PAGE				Form Approved OMB No. 074-0188	
<p>The public reporting burden for this collection of information is estimated to average 1 hour per response, including the time for reviewing instructions, searching existing data sources, gathering and maintaining the data needed, and completing and reviewing the collection of information. Send comments regarding this burden estimate or any other aspect of the collection of information, including suggestions for reducing this burden to Department of Defense, Washington Headquarters Services, Directorate for Information Operations and Reports (0704-0188), 1215 Jefferson Davis Highway, Suite 1204, Arlington, VA 22202-4302. Respondents should be aware that notwithstanding any other provision of law, no person shall be subject to a penalty for failing to comply with a collection of information if it does not display a currently valid OMB control number.</p> <p><b>PLEASE DO NOT RETURN YOUR FORM TO THE ABOVE ADDRESS.</b></p>					
1. REPORT DATE (DD-MM-YYYY) 27-03-2014		2. REPORT TYPE Master's Thesis		3. DATES COVERED (From – To) October 2012 – March 2014	
TITLE AND SUBTITLE  LIQUID SPRAY CHARACTERIZATION IN FLOW FIELDS WITH CENTRIPETAL ACCELERATION				5a. CONTRACT NUMBER	
				5b. GRANT NUMBER	
				5c. PROGRAM ELEMENT NUMBER	
6. AUTHOR(S)  Brinker, Andrew J., Captain, USAF				5d. PROJECT NUMBER	
				5e. TASK NUMBER	
				5f. WORK UNIT NUMBER	
7. PERFORMING ORGANIZATION NAMES(S) AND ADDRESS(S) Air Force Institute of Technology Graduate School of Engineering and Management (AFIT/ENY) 2950 Hobson Way, Building 640 Wright-Patterson AFB OH 45433-8865				8. PERFORMING ORGANIZATION REPORT NUMBER  AFIT-ENY-14-M-09	
9. SPONSORING/MONITORING AGENCY NAME(S) AND ADDRESS(ES) Air Force Office of Scientific Research Dr. Chiping Li 875 N Randolph St Ste 325 Rm 3112 Arlington AFB, VA 22203 chiping.li@us.af.mil				10. SPONSOR/MONITOR'S ACRONYM(S) AFOSR	
				11. SPONSOR/MONITOR'S REPORT NUMBER(S)	
12. DISTRIBUTION/AVAILABILITY STATEMENT Distribution Statement A. Approved for Public Release; Distribution Unlimited					
13. SUPPLEMENTARY NOTES This material is declared a work of the U.S. Government and is not subject to copyright protection in the United States.					
14. ABSTRACT Performing combustion in the circumferential direction has a significant potential payoff in terms of saving engine length and subsequently weight. What is not understood is the flame dynamics for a liquid fuel when sprayed into a combustor with centripetal acceleration. This investigation used phase Doppler anemometry (PDA) to characterize a nonreacting liquid spray exiting from a nozzle into a circular cavity with centripetal acceleration. The two-component velocity and size of the droplets in the cavity are measured as a function of centripetal acceleration of the air in the cavity. It was found that the droplets are accelerated by the swirling air flow and that droplet velocity increases with distance from the nozzle. Additionally it was found that water droplets evaporated within 60mm of the nozzle under the high g-load conditions. These measurements will aide in the development of compact combustors for gas turbine engines that use a circumferential cavity with swirling flow to reduce the length of the combustor. Knowing the spray distribution and residence time for the particles will allow optimization of the temperature distribution in the cavity and should enable a minimization of the number of fuel injection sites.					
15. SUBJECT TERMS Combustion, Ultra-Compact Combustion, Inter-Turbine Burner, Phase Doppler Particle Anemometry					
16. SECURITY CLASSIFICATION OF:			17. LIMITATION OF ABSTRACT  UU	18. NUMBER OF PAGES  127	19a. NAME OF RESPONSIBLE PERSON Dr. Marc D. Polanka, AFIT/ENY
a. REPORT U	b. ABSTRACT U	c. THIS PAGE U			19b. TELEPHONE NUMBER (Include area code) (937) 255-6565, ext 4714 (marc.polanka@afit.edu)

Standard Form 298 (Rev. 8-98)  
Prescribed by ANSI Std. Z39-18